Spring 2021

Visible Light Generation and Mechanistic Investigation of High-Valent Metal-Oxo Species Supported by Different Ligands

Seth Ellis Klaine
Western Kentucky University, seth.klaine128@topper.wku.edu

VISIBLE LIGHT GENERATION AND MECHANISTIC INVESTIGATION OF HIGH-VALENT METAL-OXO SPECIES SUPPORTED BY DIFFERENT LIGANDS

A Thesis
Presented to
The Faculty of the Department of Chemistry
Western Kentucky University
Bowling Green, Kentucky

In Partial Fulfillment
Of the Requirements for the Degree
Master of Science

By
Seth Klaine

May 2021

VISIBLE LIGHT GENERATION AND MECHANISTIC INVESTIGATION OF HIGH-VALENT METAL-OXO SPECIES SUPPORTED BY DIFFERENT LIGANDS

Date Recommended 04-15-2021

_____

Dr. Rui Zhang, Director of Thesis

_____
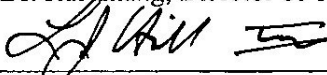
Dr. Lawrence Hill

_____
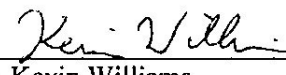
Dr. Kevin Williams

_____

Associate Provost for Research and Graduate Education

I dedicate my thesis work to Prof. Rui Zhang on the occasion of his 50th birthday for his inspirational research and mentorship. I also dedicate the present work in memory of the late Prof. Donald Slocum who started me on this journey.

PREFACE

"The unique challenge which chemical synthesis provides for the creative imagination and the skilled hand ensures that it will endure as long as men write books, paint pictures, and fashion things which are beautiful, or practical, or both."

-R. B. Woodward

TABLE OF CONTENTS

LIST OF FIGURES

LIST OF SCHEMES

LIST OF TABLES

VISIBLE LIGHT GENERATION AND MECHANISTIC INVESTIGATION OF HIGH-VALENT METAL-OXO SPECIES SUPPORTED BY DIFFERENT LIGANDS

Seth Klaine   May 2021   Pages 113

Directed by: Dr. Rui Zhang, Dr. Kevin Williams, and Lawrence Hill

Department of Chemistry   Western Kentucky University

Numerous transition metal catalysts have been designed as biomimetic model compounds for the active site of metalloenzymes found throughout Nature, most notably cytochrome P450 monooxygenases that carry out the oxidative transformations of organic substrates with near-perfect chemo-, regio-, and stereo-selectivity. The primary active oxidants in catalytic and enzymatic cycles are fleeting high-valent metal-oxo intermediates where the oxo ligand can transfer to an organic substrate in a process known as oxygen atom transfer (OAT).

In the present work, porphyrin-manganese(III), salen-chromium(III), and salen-manganese(III) derivatives were successfully synthesized and spectroscopically characterized using ^{1}H NMR and UV-Vis spectroscopies. A facile photochemical approach was applied for the successful production of porphyrin-manganese(IV)-oxo, salen-chromium(V)-oxo, and salen-manganese(V)-oxo intermediates. The photochemistry in all circumstances was rationalized through the cleavage of the oxygen-halogen bond in bromate and chlorate photo-liable precursors under visible light irradiation. The results serve as a 'proof-of-concept' that photolysis reactions are not exclusive to porphyrin or corrole systems. Meanwhile, conventional chemical oxidation methods were applied to the

generation of identical high-valent metal-oxo species using terminal oxidants, such as iodobenzene diacetate and *m*-chloroperoxybenzoic acid. The kinetics of OAT reactions of these generated metal-oxo intermediates with various organic substrates were studied, providing a direct comparison for their reactivities.

In addition, the present catalytic studies demonstrated that porphyrin-manganese(III), and salen-chromium(III), and salen-manganese(III) complexes showed excellent activity and selectivity for the oxidation of sulfides, alkenes, and activated alkanes. Furthermore, kinetic and competition studies along with Hammett analyses were conducted on the chemically- and photo-generated metal-oxo species, providing detailed mechanistic insights into the potential reaction pathways and active intermediates. With porphyrin-manganese complexes, a direct oxygen atom transfer event occurs in the presence of reactive nucleophiles such as sulfides and porphyrin-manganese(IV)-oxo species; while a disproportionation mechanism in the case of weak nucleophiles such as hydrocarbons where the premier oxidant is manganese(V)-oxo species, although the manganese(V)-oxo species was spectroscopically detectable. In the instance of salen-derivatives, there was no observed rate acceleration effect towards sulfides in the presence of electrophilic chromium(V)-oxo and manganese(V)-oxo cationic species. Presumably, the electrophilicity of these metal-oxo species was hampered due to the strong outer-sphere coordination of sulfoxide to the metal ion. The mechanistic studies imply that the observed chromium(V)-oxo and manganese(V)-oxo species are unlikely to serve as the primary oxidants under catalytic turnover conditions.

CHAPTER 1

INTRODUCTION

1.1 Cytochrome P450 Monooxygenases

By way of introduction, Cytochrome P-450 monooxygenases (customarily abbreviated P450s) play a significant role in the oxidative transformation of endogenous and exogenous organic compounds in various biological processes.[1] The active site of cysteinato heme-containing enzymes contains an iron(III) protoporphyrin IX with a proximal cysteine ligand (Figure 1-1). Initially, Axelrod in 1955 demonstrated the metabolic biotransformation of amphetamine into phenylacetone and ammonia in the presence of rabbit or rat liver microsomes, NADPH, and molecular oxygen.[2] Not known at the time, the liver microsomes contained P450s. Omura and Sato were the first to assign P450s in mammal liver microsomes to hemoproteins, and they noted that the binding of the P450 pigment with carbon monoxide (CO) displayed a characteristic Soret absorption band at $\lambda_{max} = 450$ nm.[3] P450s are responsible for the metabolism of xenobiotic compounds (substances that are exogenous with respect to the organism) and the biosynthesis of crucial signaling molecules necessary for the regulation of growth, development, and homeostasis.[1] The P450 superfamily is present in *Bacteria*, *Archaea*, and *Eukarya* domains of life, and surprisingly a report from 2009 even showed the genome sequence of a mimivirus that contained two possible cytochrome P450 genes. [4,5] In 2004, the completed human genome showed a total of 57 P450 gene sequences and 58 pseudogenes.[6] In humans, P450s assist in the metabolism of pharmaceuticals, synthesis of steroid-based hormones such as Vitamin D, as well as the transformation of certain fatty acids into biologically

active compounds.[1] In drug metabolism, only 5 gene sequences are responsible for the deactivation and clearance of pharmaceuticals from the human body.[6]
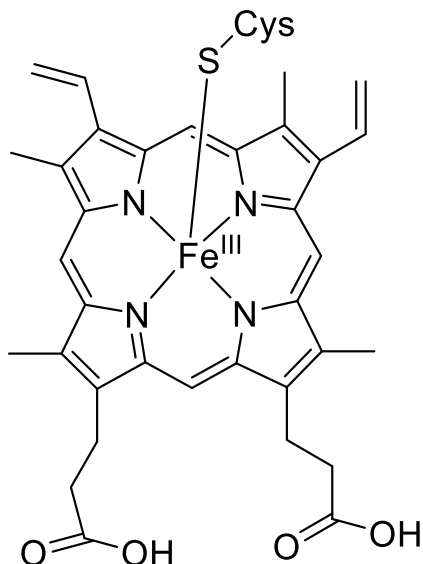
Figure 1-1. Structure of the active site of P450 consisting of a heme protoporphyrin IX with a proximal cysteine ligand.

The oxidative transformations found throughout Nature typically involve either *N-*, *S-*, and *O*-dealkylation, deformylation, dehalogenation, dehydrogenation, epoxidation, hydroxylation, sulfide oxidation reactions.[7] As shown in Scheme 1-1, the mechanism of P450 typically involves a monooxygenase reaction where activation of molecular oxygen is followed by insertion of a single oxygen atom into an organic substrate i.e. an alkane, and then reduction of the other oxygen atom into H_2O. This process also utilized two electrons provided by the electron donor, NADPH *via* cytochrome P450 reductase. Of note, an extensive set of different cofactors including flavin, copper, and non-heme iron are used throughout Nature to metabolize molecular oxygen in an oxygenase catalytic cycle, causing the integration of one or more oxygen atoms into an organic reductant.[1]

$$RH + O_2 + NADPH + H^+ \longrightarrow ROH + H_2O + NADP^+$$
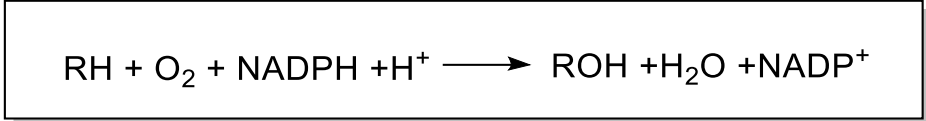
Scheme 1-1. A monooxygenase reaction, specifically hydroxylation of an aliphatic hydrocarbon, catalyzed by cytochrome P450 monooxygenase.

In 1987, Poulos and Raag presented the X-ray crystal structure of the ternary complex generated between camphor, CO, and ferrous cytochrome P-450$_{CAM}$ of the *pseudomonas putida* species which served as a model for proton-transfer mechanisms and the existence of active intermediates (Figure 1-2).[8] The structure supported the regio- and stereoselective hydroxylation of camphor at the 5-*exo*-position as shown in Scheme 2-1.

A	37–46	
B	67–77	
B	89–96	
C	106–126	
D	127–145	
E	149–169	
F	173–185	
G	192–214	
H	218–225	
I	234–267	
J	267–276	
K	280–292	
L	359–378	

β1	52–66
β2	226–233
β3	295–301
	315–323
β4	305–312
β5	382–405
	146–150
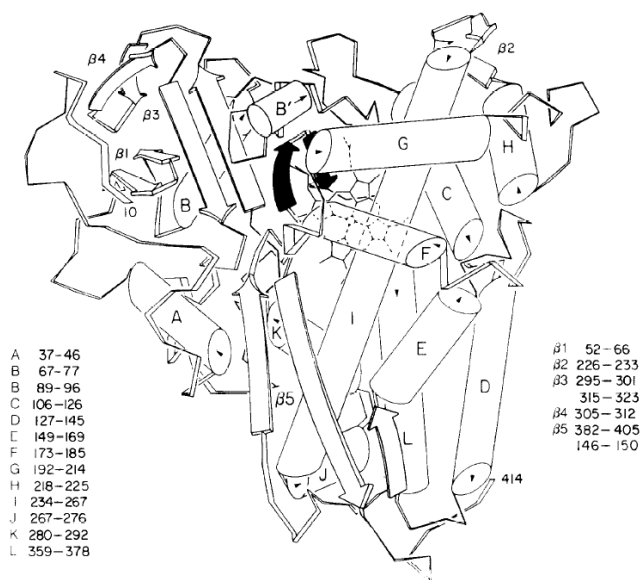
Figure 1-2. Visual representation of P450$_{CAM}$. Helices are represented by bars, and β-structure via arrows. The shading represents the antiparallel β-region and β-bulge which contains axial ligand Cys357. The residue numbers for each segment are shown in the figure. Reproduced from Ref. 8.

3
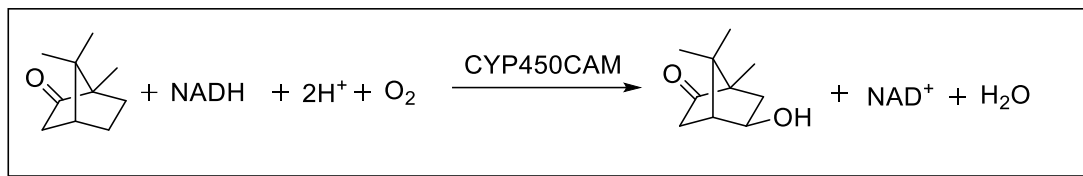
Scheme 1-2. A hydroxylation of camphor catalyzed by cytochrome P450$_{CAM}$ with dioxygen.

1.2   Catalytic Cycle of Cytochrome P450 Monooxygenases

In the 1970s, the catalytic cycle of P450$_{CAM}$ was proposed and is generally accepted by the scientific community as detailed in Figure 1-3.[1,9–11] In the resting state of the enzyme, the heme iron is hexacoordinated and is in the ferric oxidation state (**1**). In the presence of an organic substrate binding in the heme pocket, the low-spin ferric enzyme (**1**) will displace the coordinated H$_2$O axial ligand with the substrate then generate a high-spin substrate coordinated adduct (**2**). The ferric cytochrome P450 enzyme then undergoes reduction upon transport of a single electron from NADPH *via* CYP450 reductase (CPR). The high-spin state has a positive reduction potential and therefore is reduced to the ferrous state (**3**). An electron from the ferrous heme enzyme then is donated to molecular oxygen which generates a ferrous cytochrome P450-superoxo complex (**4**), a relatively stable intermediate. Through a similar process in the formation of intermediate **3**, another one-electron reduction of the complex provides a ferric cytochrome P450-peroxo intermediate (**5**). A hydroperoxo-ferric intermediate is then formed upon protonation by H$_2$O (also referred to as compound 0) (**6**). Subsequent protonation at the distal oxygen atom followed by heterolytic cleavage of the O-O bond forms an electrophilic oxoiron(V) species and water (**7**). This perferryl intermediate is short-lived and previous kinetic data suggests the iron-oxo will not accumulate before the oxygen transfer event.[12] An outer-sphere electron

4

transfer process will then produce an iron(IV)-oxo cationic radical species, known as compound I (**8**). Hydrogen atom abstraction (HAT) from the substrate generates a hydroxy-iron(IV) species (**9**) (compound II) and a substrate radical intermediate. The reaction proceeds through a hydroxyl rebound mechanism which generates a product-coordinated complex. Another mechanistic facet is that the oxo ligand can directly transfer to the substrate through an oxygen atom (OAT) process to form the oxygenated product complex. The oxidized product then dissociates from the complex and ligation of H_2O regenerates the enzyme's resting state.
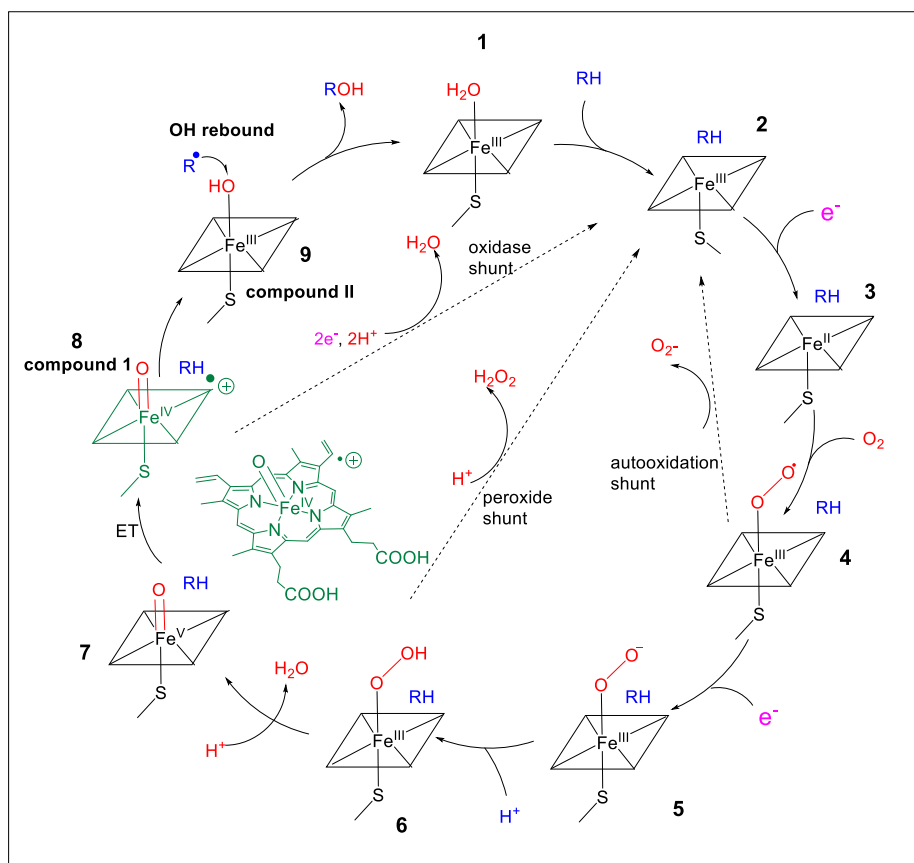
Figure 1-3. A hydroxylation reaction of camphor catalyzed by cytochrome P450$_{CAM}$ with molecular oxygen.

1.3   Metalloporphyrin-Catalyzed Oxidations

As detailed in the earlier section, the catalytic ability of the P450 active site is due to the presence of short-lived high-valent metal species. In the catalytic cycle P450s, a ferryl-oxo cation radical is the principal hydroxylating agent that operates through a hydroxyl rebound mechanism. In view of this, P450s have received considerable attention due to their catalytic ability in the hydroxylation of inactivated alkanes as well as numerous other traditionally difficult biotransformations.[13] Copious amounts of transition metal complexes bearing a variety of ligand designs have been developed over the last several decades in order to accomplish difficult oxidative conversions which are usually not accessible using traditional synthetic methods.[10] In particular, for the oxidation of organic sulfides, electrophilic reagents including peracids, sodium periodate, peroxy acids, and toxic oxo metal oxidants have been used with poor yields and regio-selectivities.[14]

First- and second-row transition metals have incomplete *d*-orbitals which allow for favorable interactions between the electronic structures of the metal complex with that of an organic substrate. Transition-metal catalytic systems have the added benefit of enhancing the rate of a reaction by supplying an alternate mechanistic pathway with lower activation energy than the un-catalyzed pathway. Many of these transition metal complexes, known as model or biomimetic compounds, have been synthesized to directly imitate the structure and function of the active oxidants involve in the catalytic cycles of various metalloenzymes such as P450.[15–17] Enzyme-like oxidation catalysts are often utilized in the manufacturing of useful intermediates and fine chemicals, such as alcohols and epoxides, in the chemical and pharmaceutical industries.[14] The use of biomimetic catalysts will contribute to the development of green, eco-friendly chemical processes by

improving the efficiency of industrial-scale reactions and implementing nontoxic terminal oxidants.[14,18]
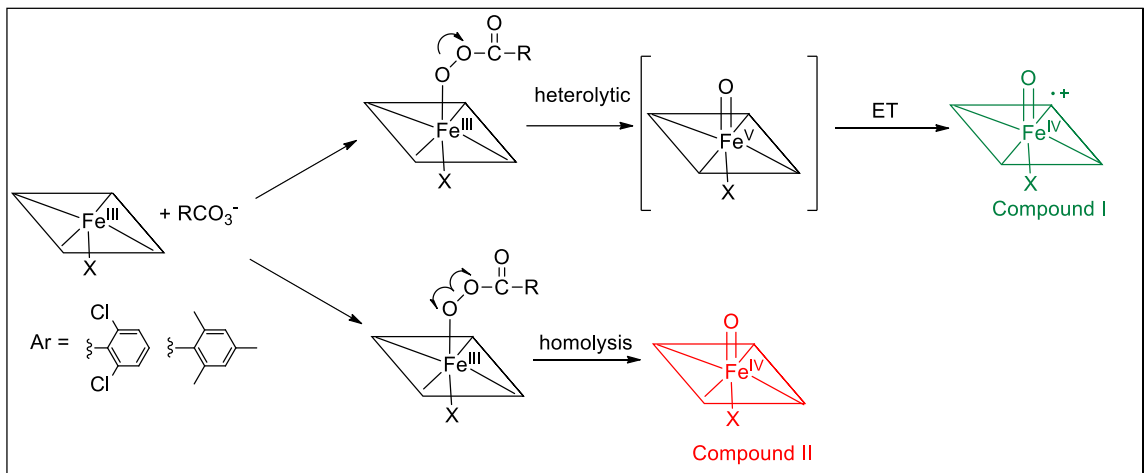
Figure 1-4. Generation of compound I and compound II models by chemical oxidation of porphyrin-iron(III) complexes.

Metalloporphyrins have functioned as excellent model compounds for the active intermediates found in the catalytic cycle of P450 enzymes. An iron(IV) oxo porphyrin cation species has been extensively characterized in the catalytic cycles of catalases, horseradish peroxidases, and chloroperoxidases.[1,7,19] Groves et al. in 1979 developed the first metalloporphyrin catalytic system for hydroxylation and epoxidation of adamantane and olefins, respectively, using PhIO as the terminal oxidant.[20] In 1981, Groves and colleagues generated and detected Compound I model species upon chemical oxidation using 1.5 equivalents (equiv.) of *m*-chloroperoxybenzoic acid (mCPBA) as terminal oxidant and the porphyrin-iron(III) complex [Fe^{III}(TMP)Cl] (TMP = 5,10,15,20 tertramesitylporphyrinato) in a CH_2Cl_2:MeOH solutions at -78 °C (Figure 1-4).[21] The dark-green Compound I model was assigned to iron(IV)-oxo porphyrin radical cation

intermediate [$Fe^{IV}(TMP^{+\bullet})(O)X$]. In the same report, Groves et al. demonstrated that iron(IV)-oxo species (Compound II) models can be generated *via* the oxidation of [$Fe^{III}(TMP)Cl$] with stoichiometric amounts of PhIO in CH_2Cl_2 at -78 °C.[21] The Compound I model was further characterized using X-ray absorption edge and extended X-ray absorption fine structure spectroscopy (XANES and EXAFS) in subsequent reports by Groves et al.[22,23] The reaction of [$Fe^{II}(DCTPP)(ClO_4)$] (DCTPP = 5,10,15,20-tetrakis(2,6-dichloro)phenylporphyrinato) with iodopentafluorobenzene, O_3, or mCPBA in CH_3CN solutions at -35 °C generated a Compound I model.[24] Furthermore, chemical oxidation of [$Fe^{II}(DCTPP)(ClO_4)$] with mCPBA in THF or DMF also produced neutral porphyrin-iron(IV)-oxo species.[25] Compound I models, consisting of an iron(IV)-oxo porphyrin radical cation, are generally more active for OAT reactions than neutral iron(IV)-porphyrin-oxo complexes, Compound II models, because of the complexes radical character.[7] Although short-lived and not spectroscopically observable, iron(V)-oxo complexes are more reactive towards oxidation reaction than Compound I models due to their higher valency.

Over the last couple of decades, the reaction scope of oxidative transformations achieved by metalloporphyrin catalytic systems consisting of different transition metals and terminal oxidants has been extensively expanded including oxidations, such as epoxidation and hydroxylation, of conventionally inert olefin and alkane substrates (Figure 1-5).[15] Of note, asymmetric metalloporphyrin catalysts have been developed to carry out enantioselective epoxidation of alkenes.[26]
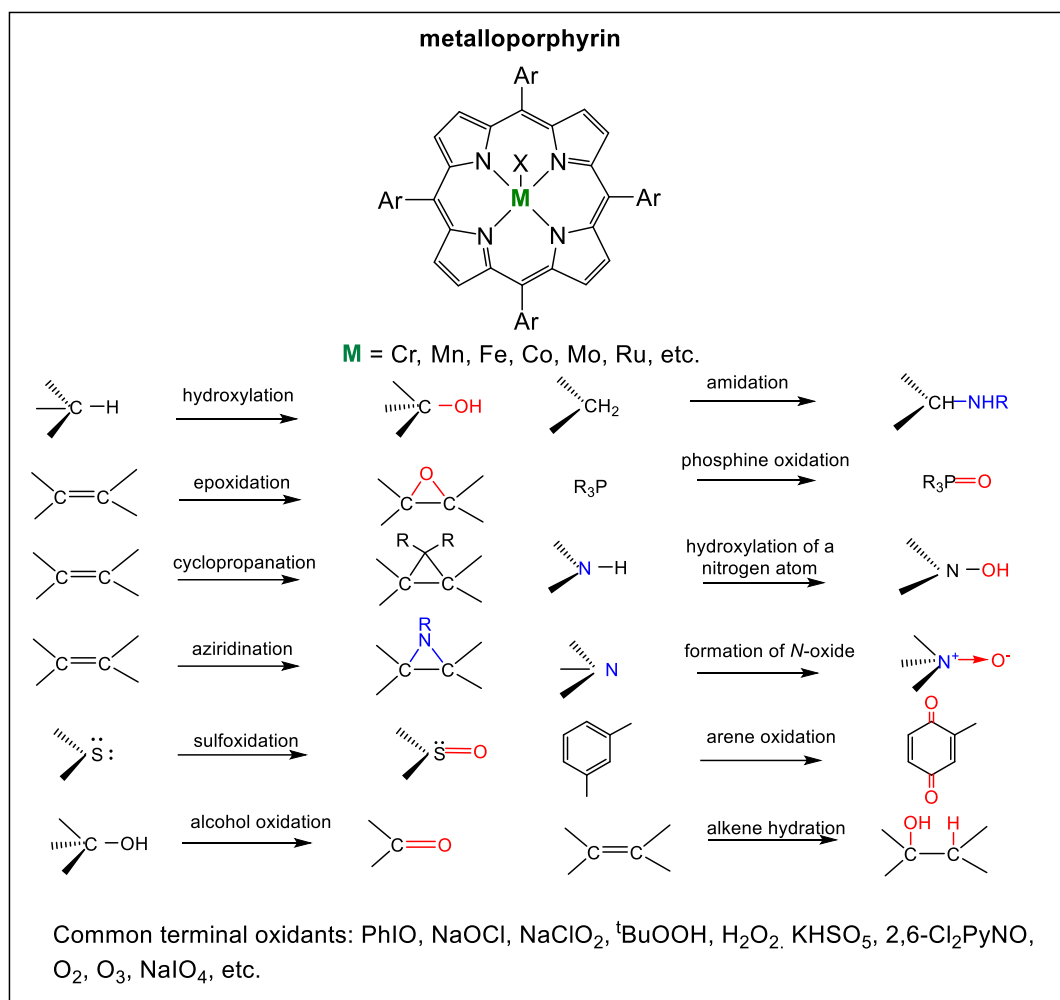
Figure 1-5. Metalloporphyrin-catalyzed oxidative reactions.

1.4   Metallosalen-Catalyzed Oxidations

Metallosalen complexes (salen = N,N'-bis(salicylidene)ethylenediamine) have garnered increased attention due to their synthetic utility in catalytic reactions.[27,28] Metallosalens share similar characteristics with metalloporphyrins and the active site of heme-based enzymes with respect to their tetradentate binding pattern, structure, and catalytic properties.[29] Metallosalens are considered "privileged" catalysts meaning that they can achieve a vast array of different organic transformations while preserving enantioselectivity. Compared to the porphyrin macrocycle, synthetic preparation of salen

9

ligand is a relatively straightforward process involving the condensation reaction of 2 equiv. of salicylaldehyde to 1 equiv. diamine analogue. Most notably, the diamine backbone of the salen ligand can easily be modified to create an asymmetric environment surrounding the metal ion, unlike metalloporphyrin analogues where the chiral element is predominately located on the *meso*-aryl moiety.[26,29] In general, enantioselective transition-metal catalysts are effective at the low substrate to catalyst ratios, therefore these catalysts are implemented for macro-scale syntheses in the chemical industry.[30,31] Many of the chemical building blocks of Nature, such as amino acids and carbohydrates, are biosynthetically made to exclusively produce a single enantiomer. Asymmetric oxidations also play a particularly important role in the synthesis of pharmaceuticals because enantiomers of a compound could cause different biological activities.
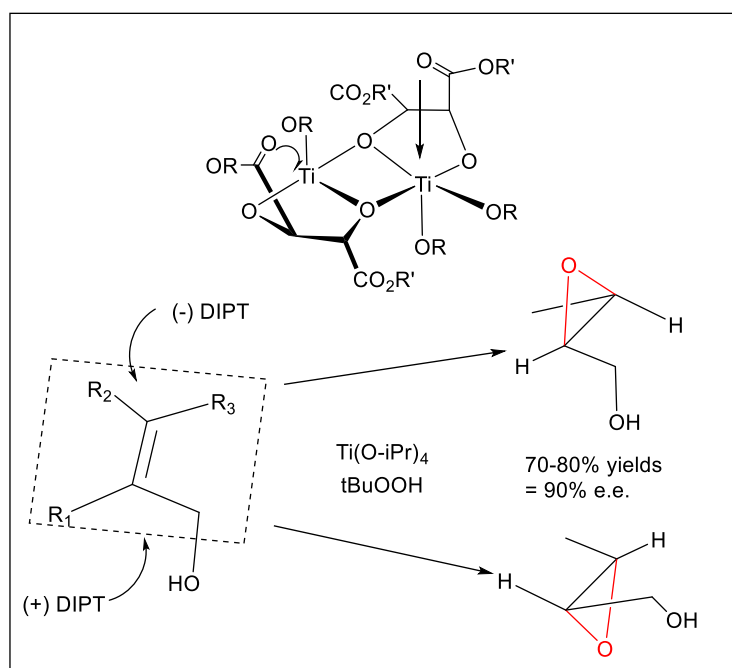
Scheme 1-3. Sharpless epoxidation of allylic alcohols.

10

As shown in Scheme 1-3, in the 1980s, Sharpless and Katsuki were the first to develop asymmetric epoxidation of allylic alcohols using a titanium tartrate complex and ^{t}BuOOH as terminal oxidant, achieving enantiomeric excesses (ee) greater than 90%.[32] Sharpless was a recipient of the 2001 Nobel Prize in Chemistry for his part in the discovery of asymmetric oxidations including his hallmark asymmetric dihydroxylation reaction of alkenes using an osmium tetroxide chiral quinine-complex.[33,34] Although the Sharpless and Katsuki epoxidation reaction has been implemented in the design of synthetic intermediates in the total synthesis of complex natural products, such as erythromycin and methmycin, there is a prominent disadvantage to this reaction.[35] Without the presence of the allylic alcohol moiety, the alkene reaction is functionally inert thus the reaction will not proceed. However, in the early 1990s, the research groups of Jacobson and Katsuki independently developed chiral salen-manganese complexes that can accomplish the asymmetric epoxidation of unfunctionalized olefin substrates (Scheme 1-4).[36,37]
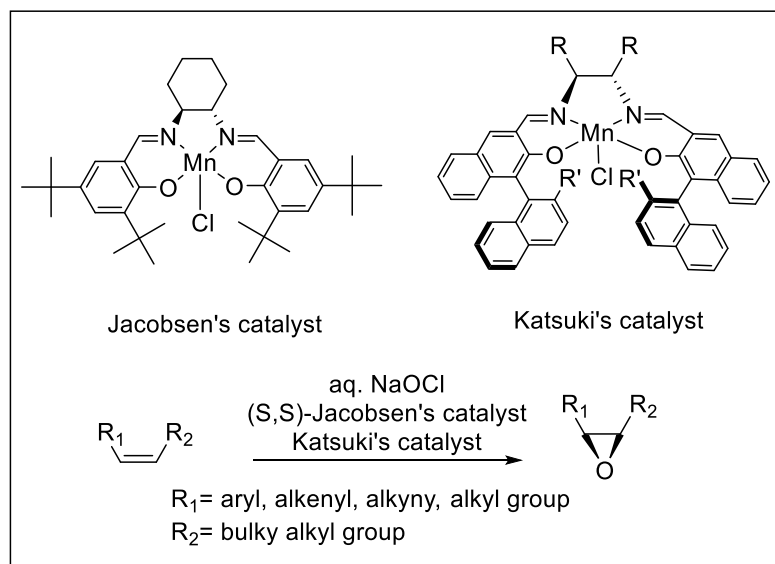
Scheme 1-4. Manganese-salen catalyzed epoxidation of olefins.

Recent reviews have contended that metallosalen-catalyzed reactions can achieve a plethora of highly selective asymmetric and achiral organic transformations including epoxidation, epoxide ring openings, carbonyl additions, cycloadditions, enol oxidations, C-H activations, etc.[27,30,38–40] Figure 1-6 surmises a myriad of reactions that can be administered using metallosalen-catalytic systems using various terminal oxidants.
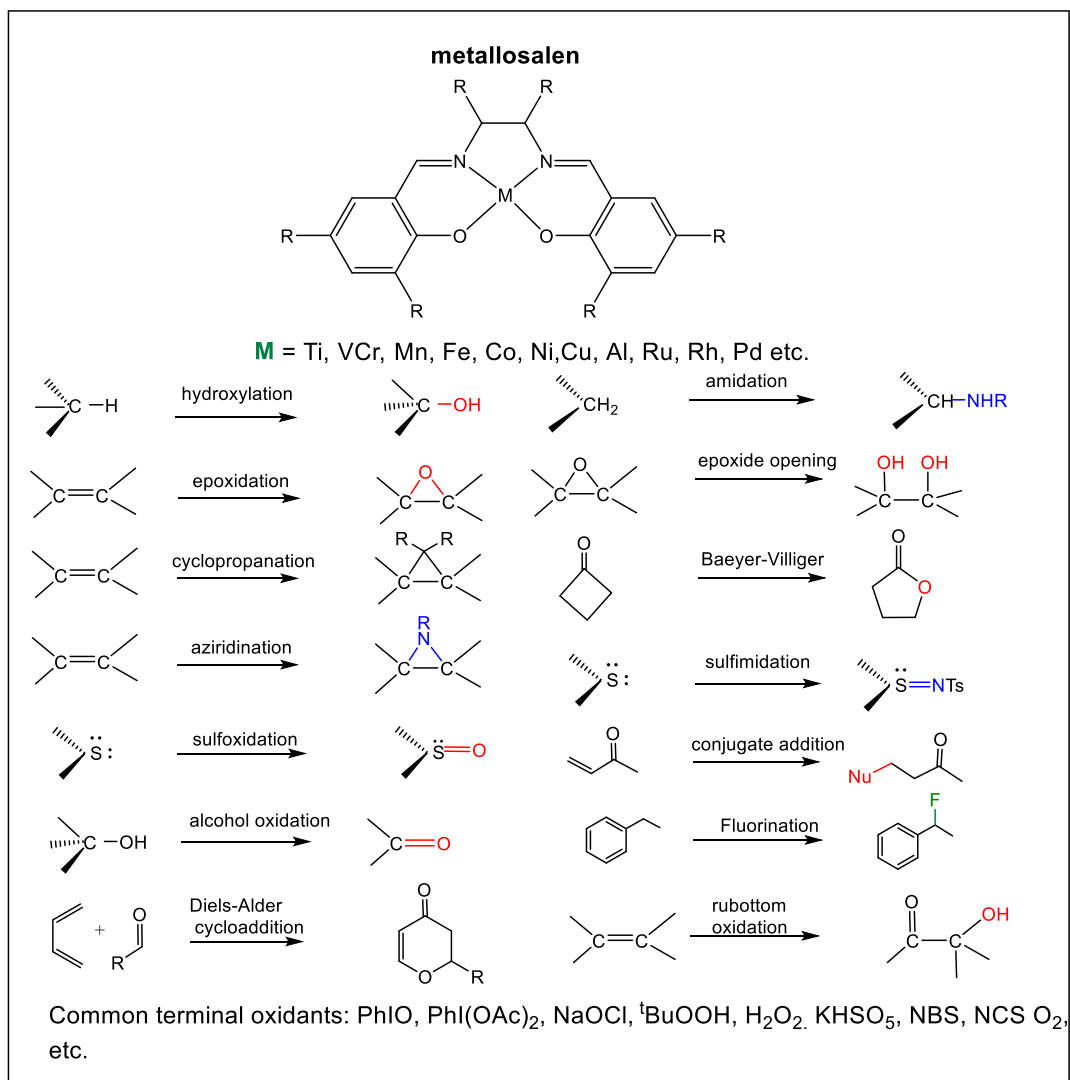
Figure 1-6. Metallosalen-catalyzed reactions.

1.5   Photochemical Generation of High-Valent Metal-Oxo Complexes

Visible light is a constant renewable energy source that could be employed in environmentally sustainable chemical syntheses. Recent developments in photochemical methods have heightened the need to produce and investigate reactive metal-oxo intermediates in OAT reactions. An OAT species generated through photochemical processes is acquired through the absorption of a photon which prevents the accumulation of byproducts like in conventional chemical oxidations.[41,42] The principal advantage to photochemical production is that short-lived intermediates can be detected with greater temporal resolution than fast-mixing reactions. [43–45] Second- and higher-order rate constants and mechanistic elucidations under photochemical approaches are significantly simplified because real-time kinetic studies of high-valent metal-oxo species can be conducted under single turnover conditions without equilibrium convolution from terminal oxidants.[46,47] In this context, production and kinetic investigation of several high-valent transition metal-oxo intermediate using laser flash photolysis (LFP) techniques have been extensively been reported in the literature.[46]

Over the last decade, our laboratory has developed two different photochemical approaches involving photo-induced ligands cleavage reactions and photo-disproportionation of μ-oxo metal *bis*-porphyrins to generate high-valent metal oxo species (Figure 1-7). Newcomb et al. pioneered the visible-light ligand cleavage reaction method for the generation of metal-oxo analogues.[45,47,48] Photo-induced ligand cleavage reactions utilize the homolysis of the O-X bond in the photo-liable haloate precursor resulting in single-electron oxidation of the metal ion. In addition, the precursors can undergo heterolysis causing two-electron oxidation of the metal complex. To illustrate, in electron

13

enriched porphyrin ligands, visible light irradiation of porphyrin-iron(II) bromate or chlorates generated porphyrin-iron(IV)-oxo cationic radicals (Compound I models). However, photolysis or porphyrin-iron(III) bromate precursors with electron demanding ligands created iron(IV)-oxo porphyrins (Compound II models).[49,50] By the same token, laser flash photolysis (LFP) of porphyrin-manganese(III) perchlorate and chlorate complexes generated porphyrin-manganese(V)-oxo and porphyrin-manganese(IV)-oxo species allowing for direct kinetic studies of organic substrates.[51]
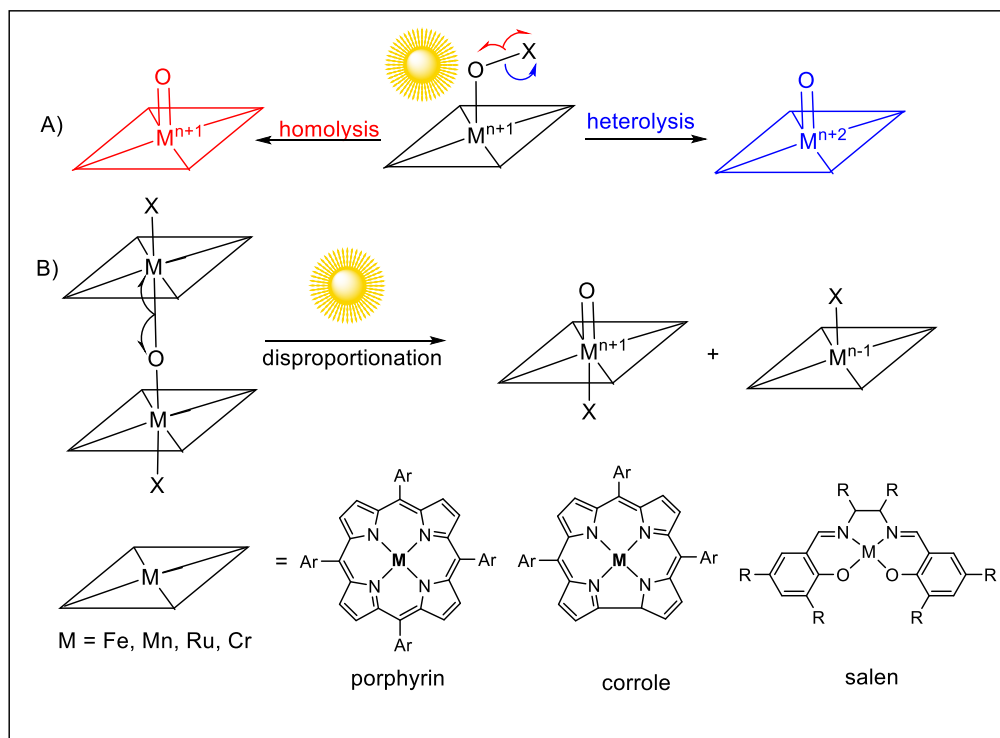
Figure 1-7. Photochemical approach of reactive high-valent metal-oxo intermediates through (A) visible light-induced ligand cleavage and (B) photo-disproportionation reactions.

14

More recent attention has focused on the provision of cofacial μ-oxo dimeric metal complexes bearing various macrocyclic ligands in view of their catalytic ability in the development of sustainable oxidative processes.[52,53] A recent study examined the photo-disproportionation of diiron(III)-μ-oxo *bis*-porphyrin complexes that generated an iron(II) and iron(IV)-oxo porphyrin pair in which the higher-valent species led to the oxidation of organic substrates under aerobic conditions.[54] Intriguingly, light irradiation of the dimeric complex activated dioxygen for OAT with the use of certain coreductants. By way of contrast, one major disadvantage of this particular cleavage reaction is that the quantum yields are poor due to the reaction of iron(IV)-oxo and iron(II) complexes to generate the initial μ-oxo-bis-porphyrins. In one well-known recent study, Nocera and colleagues developed "Pacman" ligands of diiron(III)- μ-oxo complexes that utilized spacer-hinges to maintain the cofacial arrangement of the iron ion centers thus improving the overall catalytic efficiency.[55,56] Our laboratory previously showed that the photo-disproportionation reaction of a bis-porphyrin-diruthenium(IV) μ-oxo dimer using LFP generated a porphyrin-ruthenium(V)-oxo species which served as a potent OAT reagent.[57] The *bis*-porphyrin-diruthenium(IV) μ-oxo dimer also displayed unique photocatalytic aerobic oxidations of activated alkenes and alkanes where the principal oxidant was attributed to a rare ruthenium(V)-oxo species. The following chapters will discuss attractive and novel oxidation processes that can be achieved through photochemistry. The achieved results of this investigation lay an excellent foundation for the design of innovative photo-chemical approaches to assemble active high-valent metal oxo species supporting porphyrin and salen ligands with special emphasis on the use of mild and 'green' terminal oxidants for chemical approaches.

CHAPTER 2

EXPERIMENTAL SECTION

2.1   Materials

Reagent-grade purity was utilized for all commercially available reagents and reagents were used as supplied unless specified. Organic solvents used in synthetic preparations and chromatographic purification including acetone, acetonitrile, dichloromethane (CH_2Cl_2) ethanol, ethyl acetate, *N,N*-dimethylformamide (DMF), methanol, n-hexane, and propionic acid, and tetrahydrofuran (THF) were purchased from either MilliporeSigma or Thermo Fisher Scientific Co. Additional purification of HPLC grade ($\geq$99.9%) acetonitrile, chloroform, CH_2Cl_2, or methanol and was carried out through column chromatography using dry activated Al_2O_3 (Grade I, basic or neutral). Organic reductants used in oxidation kinetics and catalytic investigations including cyclohexane, *cis*-cyclooctene, 1-phenylethanol, diphenylmethane *cis*-stillbene, substituted sulfides and styrenes were purified *via* flash column chromatography using silica gel or dry activated Al_2O_3. Pyrrole was freshly distilled before use in synthesis. Mesitaldehyde, 2,6-difluorbenzaldehyde, 2,3,4,5,6-pentafluorobenzaldehyde, 2-hydroxy-1-naphthaldehyde, 3,5-di-tert-butyl-2-hydroxybenzaldehyde, hydrochloric acid (HCl), boron trifluoride diethyl etherate ($BF_3 \cdot OEt_2$), 2,3-dichloro-5,6-dicyano-*p*-benzoquinone (DDQ), iodobenzene diacetate, hydrogen peroxide (H_2O_2, 30%), *tert*-butyl hydroperoxide (^tBuOOH, 70%), tetramethylsilane (TMS), 1,2,4-trichlorobenzene, sodium chloride, potassium carbonate, manganese(II) acetate tetrahydrate, chromium(II) chloride, chloroform-*d* (CDCl$_3$), (*R,R*)-*N,N'*-Bis(3,5-di-tert-butylsalicylidene)-1,2-cyclohexanediaminochromium(III) chloride, (*R,R*)-(−)-*N,N'*-Bis(3,5-di-*tert*-

butylsalicylidene)-1,2-cyclohexanediaminomanganese(III) chloride, triphenyl phosphine, pyridine, pyridine N-oxide (PyNO), imidazole (Imid) were obtained Millipore Sigma Co. and used as supplied. The oxygen source, m-chloroperoxybenzoic acid (mCPBA) was purchased from Millipore Sigma Co. and was then recrystallized in n-hexane:CH_2Cl_2 (3:1) at -20 °C before use. The reagent (±)-$trans$-1,2-diaminocyclohexane was purchased from Tokyo Chemical Co. (TCI) and used as such. All the silver salts mentioned below were also purchased. All precursor salts were prepared by stirring excess $AgBrO_3$, $AgClO_3$, $AgClO_4$, $AgNO_2$, $AgNO_3$, with $[Mn^{III}(Por)Cl]$, $[Cr^{III}(Salen)Cl]$, or $[Mn^{III}(Salen)Cl]$ complexes. Silver salts were also purchased from Millipore Sigma Co. The corresponding salt solutions were then filtered using PTFE (hydrophobic) syringe filters and then immediately employed for kinetic and catalytic studies.

2.2   Methods

2.2.1   Physical Measurements and Instrumentation

^{1}H-NMR was conducted on JEOL-ECA-400 spectrometer (Figure 2-1A) equipped with an autosampler at 298K using 0.03% TMS as an internal standard and chloroform-d as solvent. The chemical shifts are reported with respect to an internal TMS standard. Ultraviolet-visible spectroscopy (UV-Vis) was performed on either an Agilent 8453 diode array spectrometer (Figure 2-1B) using a 1.0-cm quartz cuvette or an Applied Photophysics SX20–stopped-flow spectrometer equipped with a photodiode array detector (PDA) (Figure 2-1C). The sequential three-syringe stopped-flow system has a total of 400 μL/shot into a 1.0-cm light path cuvette, and the fastest time for mixing two solutions and recording the first data point was $ca.$ 1 ms. Visible light irradiation was produced using a SOLA SE II light engine (Lumencor) tailored with a liquid light guide (6-120 W) (Figure 2-1D). For

some preliminary investigations, a Newport Xenon arc lamp solar simulator (Figure 2-1E) was also used to produce visible light matching solar spectra. Gas-Chromatography Mass-Spectrometry (GC-MS) was performed on an Agilent GC6890/MS5973 equipped with a flame ionization detector (FID), J&W Scientific DB-5 capillary column, and an auto-sampler injector (Figure 2-1F). Electrospray ionization-mass spectroscopy (ESI-MS) was conducted on an Agilent 500 LCMS Ion Trap System (Figure 2-1G).
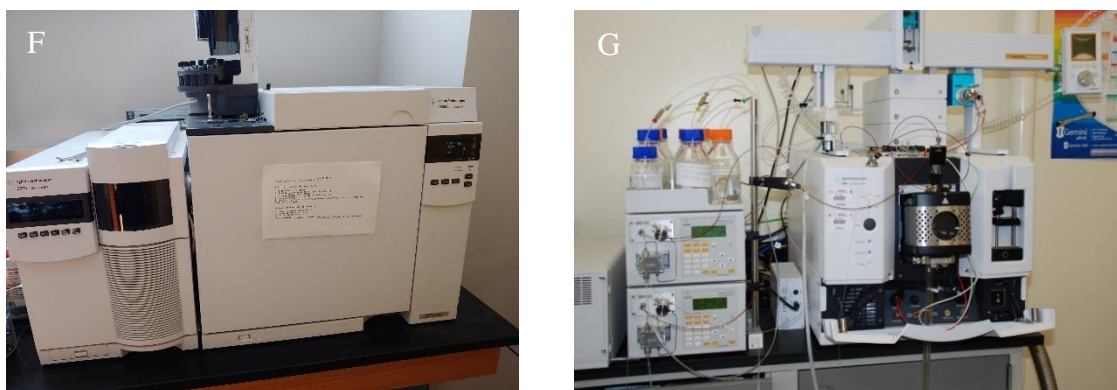
Figure 2-1. JEOL ECA-400 MHz spectrometer. (B) Agilent 8453 diode array spectrometer. (C) Applied Photophysics SX20–stopped-flow spectrometer (D) Lumencor SOLA SE II light engine. (E) Newport Xenon arc lamp solar simulator. (F) Agilent GC7820A/MS5975. (G) Agilent 500 LCMS Ion Trap System.

2.2.2 General Procedure for Photo-Induced Axial Ligand Cleavage Reactions of Manganese(III) porphyrin [Mn^{III}(Por)X], Chromium(III) Salen [Cr^{III}(Salen)X], and Manganese(III) Salen [Mn^{III}(Salen)X]

Successful axial ligand exchange of the chloride counter ions in the manganese(III) and chromium(III) porphyrin and salen complexes was achieved by stirring excess of a silver salt (AgBrO$_3$, AgClO$_3$, AgNO$_2$) in anaerobic CH$_3$CN. The reaction generated photo-labile precursors of the corresponding salt products: [Mn^{III}(Por)ClO$_3$], [Mn^{III}(Por)BrO$_3$], [Cr^{III}(Salen)BrO$_3$], [Cr^{III}(Salen)ClO$_3$], [Cr^{III}(Salen)NO$_2$]. As a driving force for the ligand-exchange reaction, AgCl precipitates out of CH$_3$CN and is subsequently filtered out using a syringe filter. The exchange reactions were monitored using UV-Vis Spectroscopy, and upon full conversion to the photolabile intermediate, the complexes were immediately deployed for photochemical investigations.

2.2.3 Kinetic Studies on High-Valent Metal-Oxo Intermediates

Following chemical and photochemical generation of the high-valent metal oxo species, reactions were conducted in 2 mL anaerobic CH_3CN solutions at 23 ± 2 °C with excess organic reductant (> 100 equiv.) under single-turnover parameters in order to satisfy pseudo-first-order conditions. The reaction rate represented the OAT event from the high-valent metal-oxo to the organic reductant. The reaction was monitored *via* measuring the decay of the Soret band absorbance (*ca.* 420, 680, 650 nm) corresponding to the active intermediate species. The observed rate constants in this study were determined from kinetic measurements using various concentrations of organic reductant. The kinetic trace at λ_{max} of the Soret band showed excellent *pseudo*-first-order behavior (minimum of four half-lives), and the data was analytically solved to provide *pseudo*-first-order observed rate constants, i.e. k_{obs}. The second-order rate constant for reactions of the oxo species with the organic reactants were analytically solved according to Eq. (1).

$$k_{obs} = k_0 + k_{ox}[Sub] \qquad \text{Eq 1.}$$

where k_0 represents the background decomposition rate constant determined without substrate, k_{ox} is the second-order rate constant for the reaction with the substrate, and [Sub] (Sub = substrate) is the concentration of the organic substrate reductant. The slope of the linear regression line of the kinetic plot, consisting of k_{obs} values as a function of the concentration of reductant, represents the second-order rate constant and was nearly linear in all circumstances. The second-order rate constants were average of 2-3 determinations of independent kinetic measurements and the error was weighed to 2σ.

2.2.4 General Procedure for Catalytic Oxidation Investigations

Unless otherwise specified, all catalytic reactions were conducted in the presence of porphyrin complex (1 μmol, 0.2 mol%) or salen complex (10 μmol, 2.0 mol%) H_2O (5 μL), 0.2 mmol organic substrates, and 1.5 equiv. of $PhI(OAc)_2$ (0.3 mmol) as an oxygen source in 2 mL anaerobic MeOH at 23 ± 2 °C. A minute amount of H_2O (5 μL) was added to hydrolyze $PhI(OAc)_2$ and therefore activating the oxygen source. Aliquots of the reaction solution at consistent time intervals were evaluated *via* GC-MS to determine the generated oxidized products, conversions, and yields with an internal standard, 1,2,4-trichlorobenzene. Isolation of oxidized products involved flash column chromatography using silica gel adsorbent followed by elution using CH_2Cl_2: hexane (1:1). Catalytic reactions were averages of 2 to 3 determination, and the product yield as a function of reaction time displayed excellent logarithmic fitting.

2.2.5 General Procedure for Competition, Hammett Correlation, and Kinetic Isotope Effect (KIE) Investigations

With regards to other mechanistic investigations, porphyrin complex (1 μmol) or salen complex (10 μmol), H_2O (4.5 μL), $PhI(OAc)_2$ (0.1 mmol) as a limiting reagent, and equimolar amounts of thioanisole (0.2 mmol) and substituted thioanisole (0.2 mmol) in CH_3OH (2 mL) solutions with 1,2,4-trichlorobenzene (0.1 mmol) as an internal standard. The reaction mixtures were stirred for *ca.* 10 to 15 min at 23 ± 2 °C. Relative reaction rate ratios for catalytic oxidation were determined via GC-FID analysis based on the relative amounts of oxidized products generated in reference to the internal standard. Competition relative ratios are averages of 2-3 determination with standard deviation smaller than 10%

of the values. The relative rate for the conversion of sulfide should accurately reflect the reactivity toward the complex-catalyzed sulfide oxidation.

2.3 Synthetic Preparation of Porphyrin and Salen Complex and Spectroscopic Characterization

2.3.1 Synthesis of Porphyrin Ligands

The synthesis of sterically hindered porphyrin was modified from a method reported by Lindsey and colleagues as demonstrated in Scheme 2-1.[58] To a 1L round-bottom flask equipped with a reflux condenser, 500 mL of HPLC grade chloroform, mesitylaldehyde (736 µL, 5 mmol) or 2,6-difluorobenzaldyde (540 µL, 5 mmol) and freshly distilled pyrrole (347 µL, 5 mmol) and 3.47 mL anhydrous ethyl alcohol (0.5% v/v). The reaction solution was then purged with argon for *ca.* 10 min. The strong Lewis-acid $BF_3 \cdot OEt_2$ (660 µL, 1.65 mmol) was added dropwise *via* syringe and the reaction was stirred using a stir bar for 3h at rt. The reaction involves an acid-catalyzed condensation where the Lewis acid activates the electrophilic aldehyde moiety towards the nucleophilic pyrrole, initiating the ring formation to afford the porphyrinogen, a reduced porphyrin intermediate. The reaction was monitored every hour *via* silica gel thin-layer chromatography (TLC) and UV-vis to verify the formation of the porphyrinogen intermediate. The next step of the reaction involved oxidation of the porphyrinogen by adding solid 2,3-dichloro-5,6-dicyano-*p*-benzoquinone (DDQ) (957 mg, 4.2 mmol). The reaction solution was then gently refluxed for 1 h and cooled to rt. Excess trimethylamine (Et_3N) (920 µL, 6.6 mmol) was then added to the solution to neutralize $BF_3 \cdot OEt_2$. The reaction solution was evaporated to dryness under reduced pressure. The crude product was scraped from the round-bottom flask and placed on filter paper for vacuum filtration. The

crude mixture was then washed with CH₃OH until the filtrate was clear. Additional purification of the product involved column chromatography using silica gel adsorbent and elution by CH_2Cl_2.
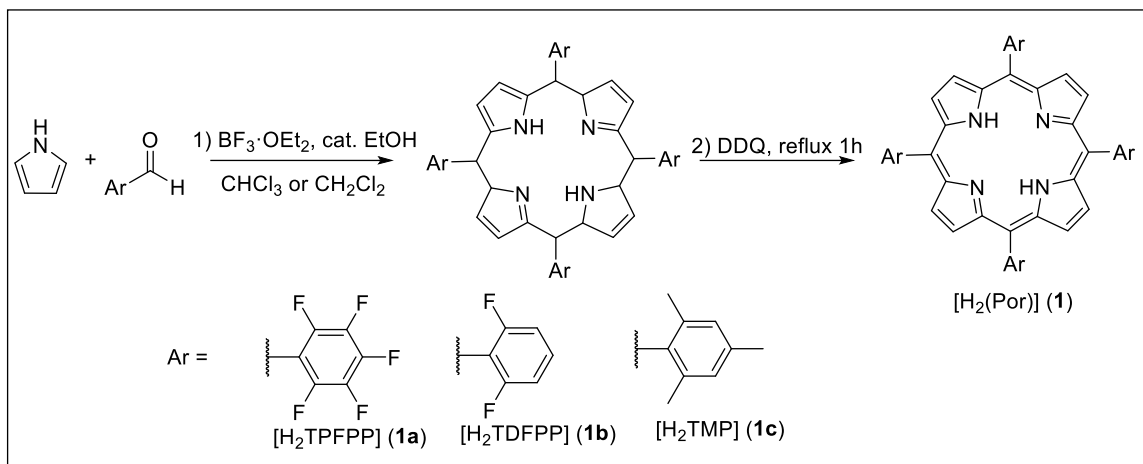
Scheme 2-1. Two-step one-pot synthesis of sterically hindered [H₂(Por)] (**1a-c**).

The reaction of H₂TPFPP was carried out in a similar manner with modification; 445 mL of CH_2Cl_2 was charged to a 1L round-bottom flask with a reflux condenser and rubber septum. Pyrrole (552 μL, 7.52 mmol) and 1,2,3,4,5-pentaflurobenzaldehyde (929 μL, 7.52 mmol) was added to the flask, and the reaction vessel was shielded from ambient light by aluminum foil. The reaction was then stirred and purged with Argon for 30 min. BF₃·OEt₂ (267 μL, 2.16 mmol) was added to the reaction solution and stirred for an additional 20 h to complete the condensation reaction. The reaction was monitored *via* TLC and UV-Vis every 5h. Upon the formation of the porphyrinogen, DDQ (708 mg, 7.52 mmol) was added to the reaction solution and refluxed for 2.5h. The reaction was then cooled to rt and the solvent was removed *via* rotary evaporation. The black crude solid was removed from the flask using a spatula and was dissolved using 236 mL of CHCl₃:*n*-hexane (7:3 v/v) and was purified using column chromatography with dried alumina basic and

23

CHCl$_3$/n-hexane (7:3 v/v) as the eluent. Characterization via UV-vis and ^{1}H-NMR of these ligands matched literature reported values.

5, 10, 15, 20-tetrakis(2,3,4,5,6-pentaflurophenyl)porphyrin [H$_2$(TPFPP)] (1a)

Yield = 902 mg (49.3%).

UV-vis (CH$_2$Cl$_2$) λ_{max}/nm: 411 (Soret), 506, 583. (Figure 2-2A)

1H-NMR (500MHz, CDCl$_3$): δ, ppm: -2.89 (s, 2H, NH), 8.94 (s, 8H, β-pyrrolic-H). (Figure 2-2B)

5, 10, 15, 20-tetrakis(2,6-difluorophenyl)porphyrin [H$_2$(TDFPP)] (1b)

Yield = 184 mg (18.6%).

UV-vis (CH$_2$Cl$_2$) λ_{max}/nm: 413 (Soret), 506, 586. (Figure 2-3A)

1H-NMR (500MHz, CDCl$_3$): δ, ppm: -2.77 (s, 2H, NH), 7.76 (m, 12H, m-ArH and p-ArH), 8.86 (s, 8H, β-pyrrolic-H). (Figure 2-3B)

5,10, 15, 20-tetramesitylporphyrin [H$_2$(TMP)] (1c)

Yield = 200 mg (%)

UV-Vis (CH$_2$Cl$_2$) λ_{max} /nm: 418 (Soret), 440, 514, 548, 591. (Figure 2-4A)

1H-NMR (500MHz, CDCl3): δ, ppm: -2.53 (s, 2H, NH), 1.84 (s, 24H, o-CH3), 2.62 (m, 12H, p-CH3), 7.25 (m, 8H, m-ArH), 8.61 (s, 8H, β-pyrrolic-H). (Figure 2-4B)
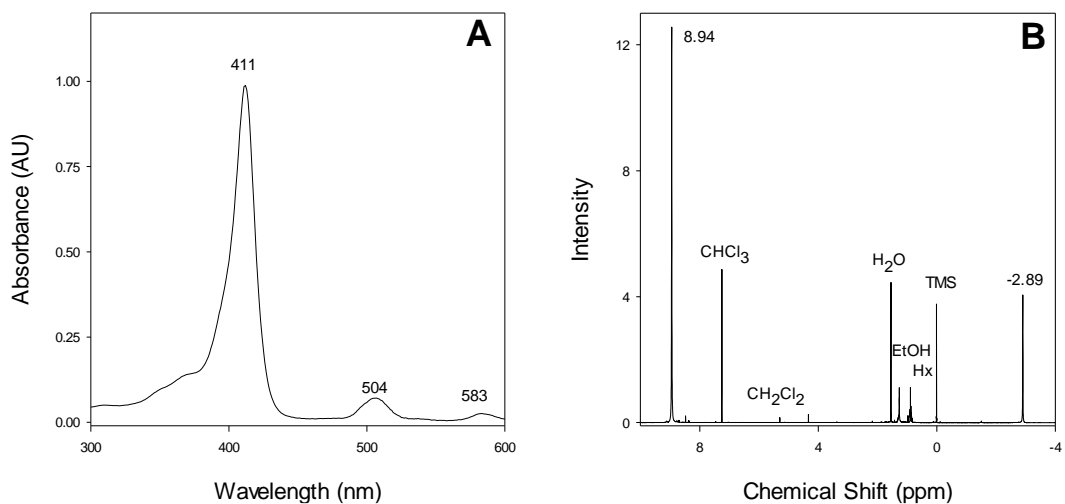
Figure 2- 2. (A) The UV-Vis spectrum of [H_2(TPFPP)] (**1a**) in CH_2Cl_2 (B) The ^{1}H-NMR spectrum of [H_2(TPFPP)] (**1a**) in $CDCl_3$.
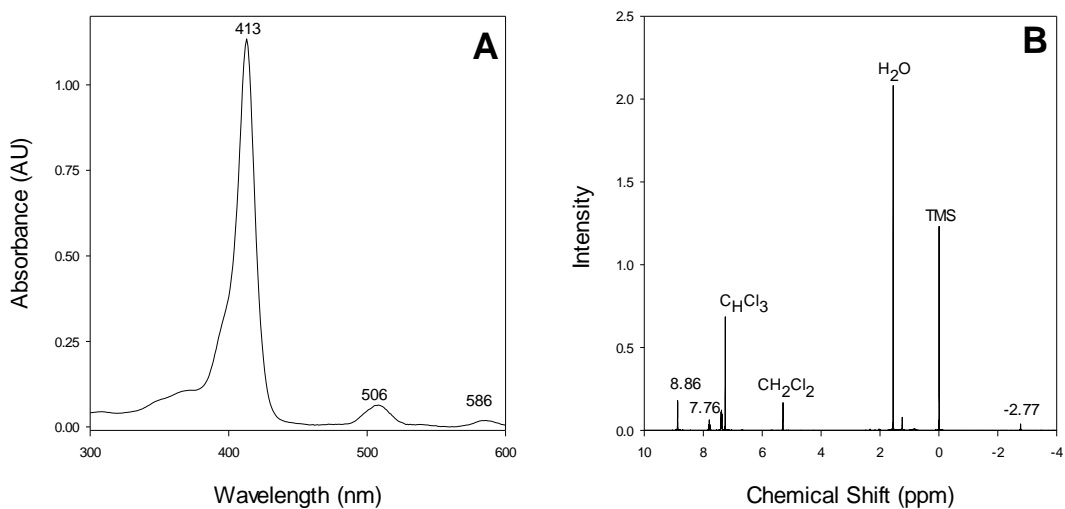
Figure 2-3. (A) The UV-Vis spectrum of [H_2(TDFPP)] (**1b**) in CH_2Cl_2 (B) The ^{1}H-NMR spectrum of [H_2(TDFPP)] (**1b**) in $CDCl_3$.
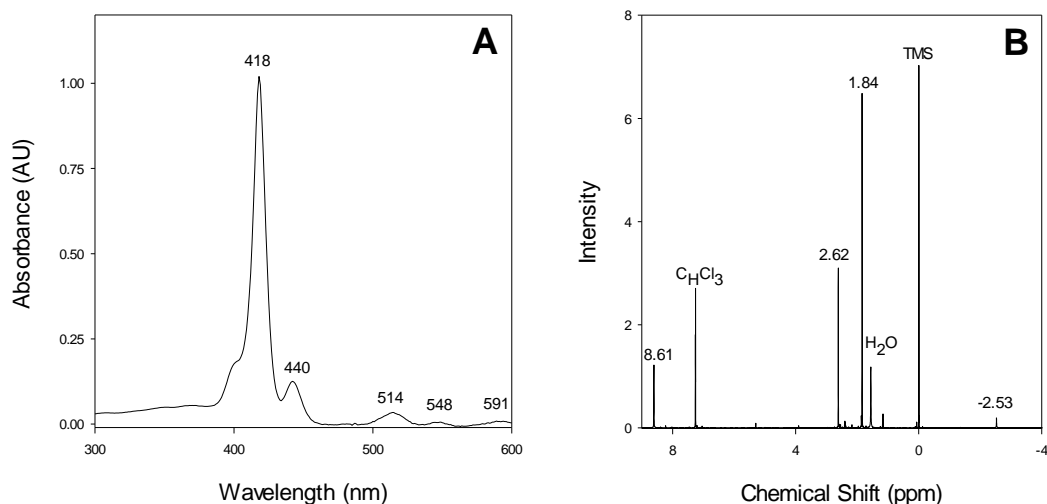
Figure 2-4. (A) The UV-Vis spectrum of [H$_2$(TMP)] (**1c**) in CH$_2$Cl$_2$ (B) The ^{1}H-NMR spectrum of [H$_2$(TMP)] (**1c**) in CDCl$_3$.

2.3.2   Synthesis of Salen Ligands

The preparation of salen ligands, commonly referred to as Schiff bases, is shown in Scheme 2-2. The procedure was modified from a report by Jacobsen and Colleagues in 1997.[38] A 25 mL round-bottom flask equipped with a stir bar and reflux condenser was charged with 10 mL of H$_2$O then 661 mg of (*R,R*)-1,2-diammoniumcyclohexane mono-(+)-tartrate salt (2.5 mmol) and 530 g of sodium carbonate (5 mol, 2 equiv.). The mixture was stirred until fully dissolved then 15 mL of anhydrous ethyl alcohol was added. The reaction was heated using a heating mantle then a solution of 3,5-di-tert-2-hydroxybenzaldehyde or 2-hydroxy-1-naphthaldehyde (5.0 mmol) in 12 mL anhydrous ethyl alcohol was added to the reaction and then refluxed for 2 h. The mechanism involves nucleophilic attack of the carbonyl moiety of the salicylaldehyde, generating a hemiaminal intermediate that rapidly undergoes dehydration to produce the imine functional group of the Schiff base. Following the reflux, the reaction vessel was submerged in an ice bath and

26

cooled to *ca.* 5°C then 15 mL of deionized H_2O was added to the solution stirred and for an additional 1 h. The yellow solid was then collected *via* vacuum filtration then washed with 10 mL of ethanol. The solid was left to dry under a vacuum and was used without further purification. UV-Vis and ^{1}H-NMR spectroscopy were then used to characterize the Schiff base free ligands.
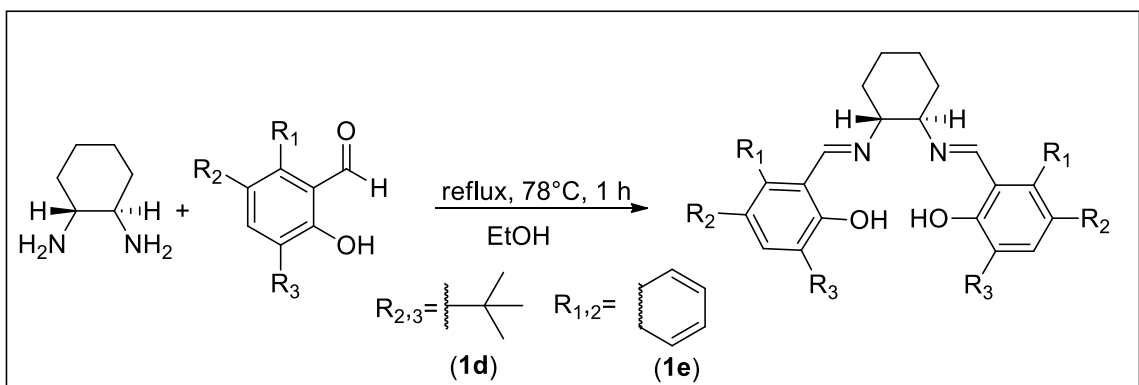
Scheme 2-2. One-step synthesis of [salen] (**1d-e**).

(*R*,*R*)-(-)-*N*,*N*'-Bis(3,5-di-*tert*-butylsalicylidene)-1,2-cyclohexanediamine

[H$_2$(Salen)] (1d) Yield = 1.2850 g (83.6%)

UV-vis (CH$_2$Cl$_2$) λ_{max}/nm: 262, 331. (Figure 2-5A)

^{1}H-NMR (500 MHz, CDCl$_3$): δ, ppm: = 13.71 (s, 2H, OH), 8.30 (s, 2H, NCH), 7.29 (d, 2H, Ar-H), 6.98 (d, 2H, Ar-H), 3.38–3.26 (m, 2H, cyclohexane-H), 1.98–1.66 (m, 8H, cyclohexane-H), 1.41 (s, 18H, *tert*-butyl), 1.23 (d, 18H, *tert*-butyl). (Figure 2-5B)

(*R*,*R*)-(-)-*N*,*N*′-Bis-(2-hydroxy-1-naphthalidene)-1,2-cyclohexanediamine

[H₂(Naphthen)] (1e) Yield = 894.2 mg (84.7%)

UV-vis (CH$_2$Cl$_2$) λ_{max}/nm: 308, 358, 402, 424 (Figure 2-6A)

^{1}H-NMR (500 MHz, CDCl$_3$): δ, ppm: = 14.64 (s, 2H, OH), 8.75(s, 2H, NCH), 7.53 (m, 4H, Ar-H), 6.98 (m, 8H, Ar-H), 3.42 (t, 2H, cyclohexane-H), 1.96 (m, 8H, cyclohexane-H). (Figure 2-6B)
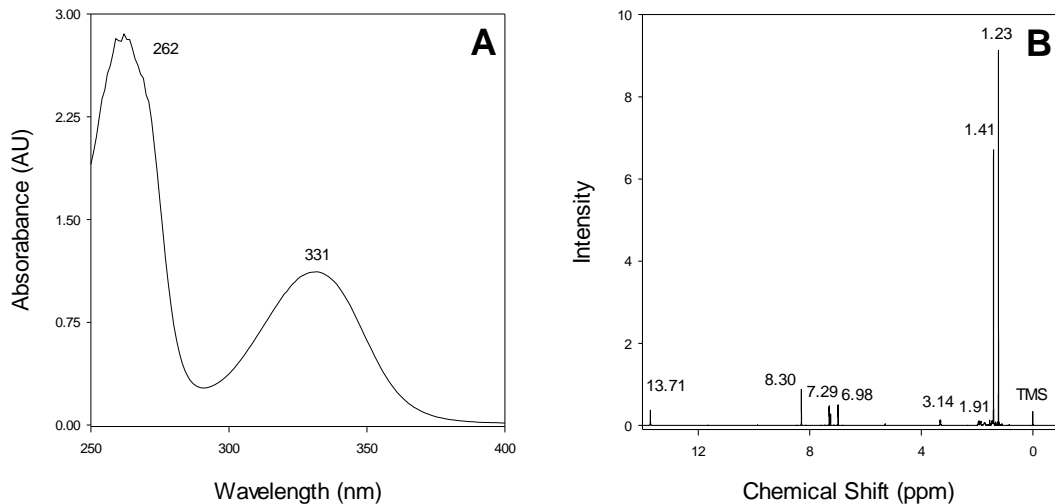
Figure 2-5. (A) The UV-Vis spectrum of [H₂(salen)] (**1d**) in CH$_2$Cl$_2$ (B) The ^{1}H-NMR spectrum of [H₂(salen)] (**1d**) in CDCl$_3$.
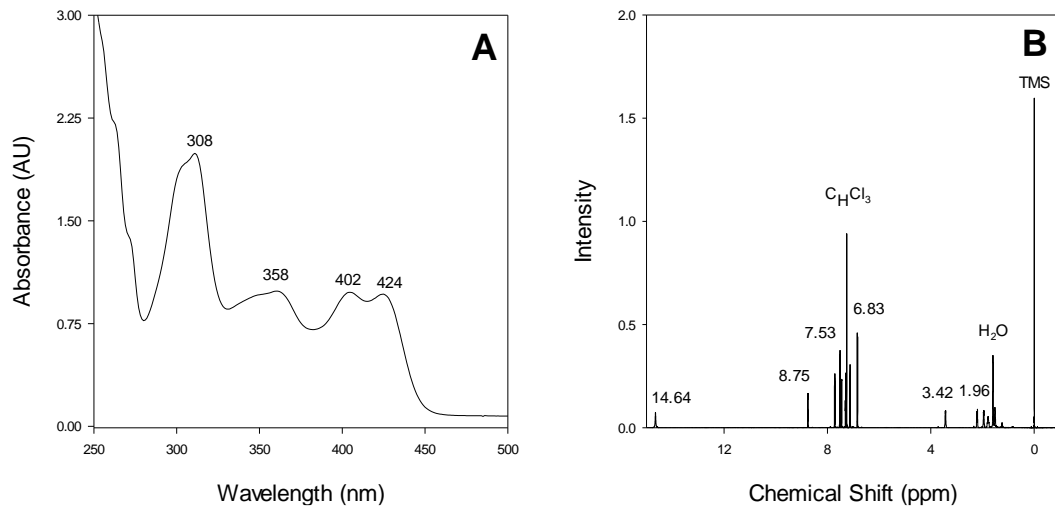
Figure 2-6. (A) The UV-Vis spectrum of [H$_2$(napthen)] (**1e**) in CH$_2$Cl$_2$ (B) The ^{1}H-NMR spectrum of [H$_2$(napthen)] (**1e**) in CDCl$_3$.

2.3.3 Synthesis of Manganese(III) Porphyrin Chloride Complexes [Mn^{III}(Por)Cl]
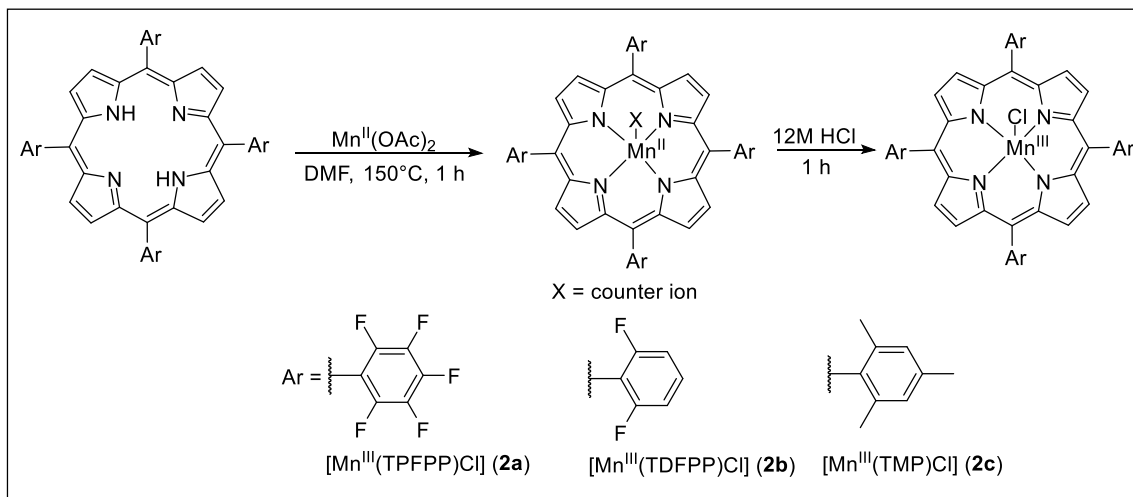
Scheme 2-3. Two-step synthesis of [Mn^{III}(Por)Cl] (**2a-c**).

In this investigation, the following porphyrin free ligands were prepared: [H$_2$(TPFPP)] (**1a**), [H$_2$(2,6-F$_2$TPP)] (**1b**), and [H$_2$(TMP)] (**1c**). The manganese (III) porphyrin complexes were prepared as detailed in Scheme 2-3. In a 100 mL round-bottom flask charged with 30 mL of *N*, *N*-dimethylformamide (DMF), 100 mg of porphyrin free ligand, and excess manganese(II) acetate tetrahydrate (300 mg). The reaction solution was degassed with argon for 10 min, refluxed for 1 h, and the reaction was monitored *via* TLC with silica adsorbent and CH$_2$Cl$_2$ eluent. The DMF was removed using a rotary evaporator. The manganese(III) porphyrin was dissolved in *ca.* 5 mL CH$_2$Cl$_2$ and 5 mL HCl (12.1 M) then stirred for 1h to exchange the OAc axial ligand to Cl. The metal complex was then dissolved with 95 mL of CH$_2$Cl$_2$, washed with H$_2$O/brine 100 mL three times, then dried over Na$_2$SO$_4$ to remove H$_2$O. Purification of the manganese(III) porphyrin involved column chromatography with silica gel adsorbent using CH$_2$Cl$_2$ as eluent. The manganese (III) complexes were characterized using UV-Vis and ^{1}H NMR spectroscopies which matched literature cited values.

5,10,15,20-tetrakis(1,2,3,4,5-pentaflurophenyl)porphyrininatomanganese(III) chloride [Mn^{III}(TPFPP)Cl] (2a)

Yield = 98 mg (98%).

UV-vis (CH2Cl2) λmax/nm: 475 (Soret), 364, 572. (Figure 2-7A)

1H-NMR (500MHz, CDCl3): δ, ppm: -22.8 (s, 8H, β-pyrrolic-H). (Figure 2-7B)

5,10,15,20-tetrakis(2,6-difluorophenyl)porphyrinatomanganese(III) chloride [Mn^{III}(TDFPP)Cl] (2b)

Yield = 80 mg (80%).

UV-vis (CH$_2$Cl$_2$) λmax/nm: 474 (Soret), 366, 570, 608. (Figure 2-8A)

1H-NMR (500MHz, CDCl3): δ, ppm: -22.0 (s, 8H, β-pyrrolic-H). (Figure 2-8B)

5,10,15,20-tetramesitylporphyrininatomanganese(III) chloride [Mn^{III}(TMP)Cl] (2c)

Yield = 78 mg (78%)

UV-Vis (CH$_2$Cl$_2$) λ_{max} /nm: 480 (Soret), 369, 401, 575, 622. (Figure 2-9A)

1H-NMR (500MHz, CDCl3): δ, ppm: -21.5 (s, 8H, β-pyrrolic-H). (Figure 2-9B)
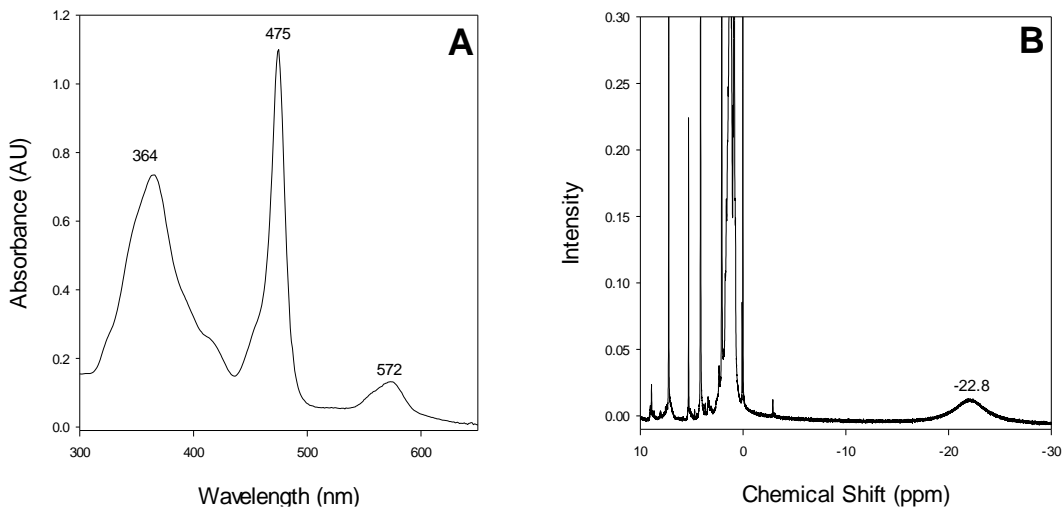
Figure 2-7. (A) The UV-Vis spectrum of [Mn^{III}(TPFPP)Cl] (**2a**) in CH$_2$Cl$_2$ (B) The ^{1}H-NMR spectrum of [Mn^{III}(TPFPP)Cl] (**2a**) in CDCl$_3$.
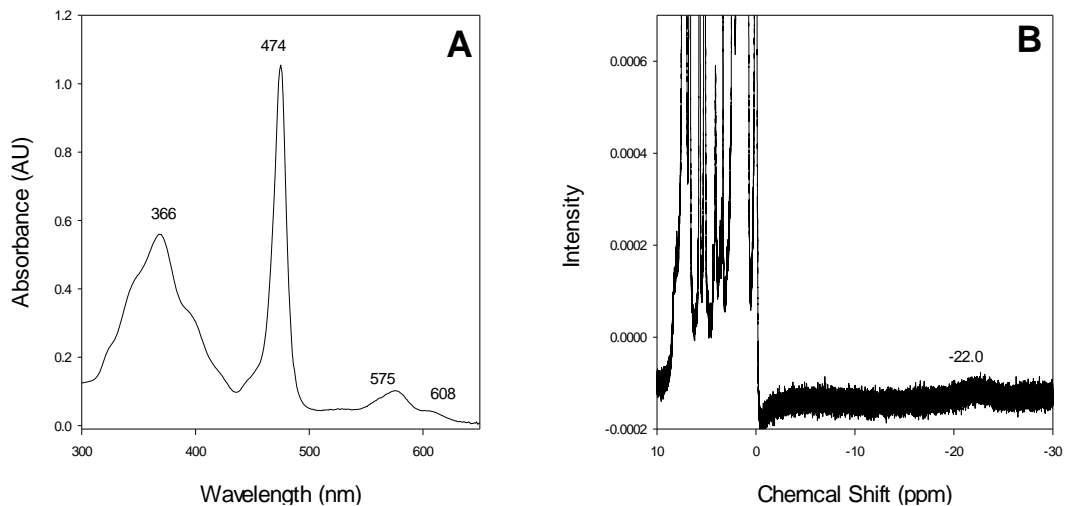
Figure 2-8. (A) The UV-Vis spectrum of [Mn^{III}(TDFPP)Cl] (**2b**) in CH$_2$Cl$_2$ (B) The ^{1}H-NMR spectrum of [Mn^{III}(TDFPP)Cl] (**2b**) in CDCl$_3$.
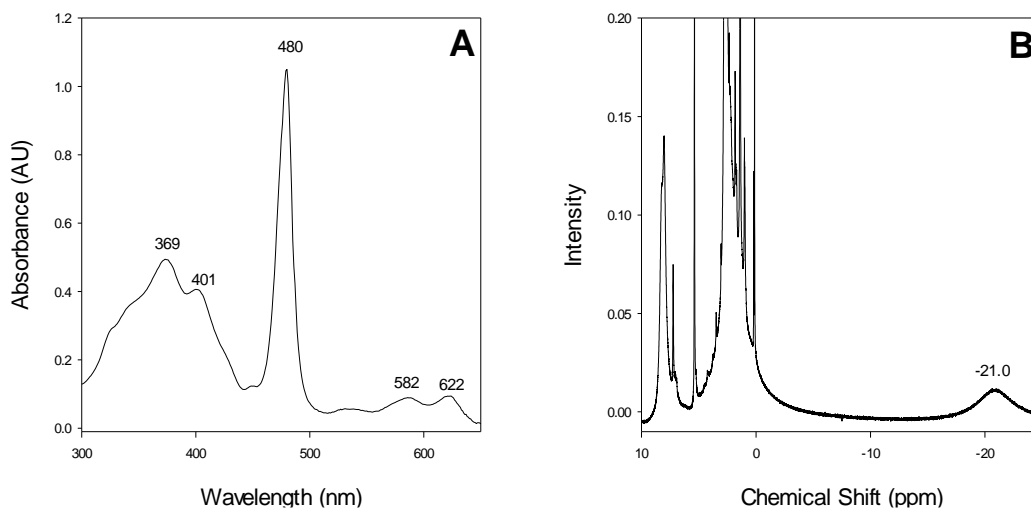
Figure 2-9. (A) The UV-Vis spectrum of [Mn^{III}(TMP)Cl] (**2c**) in CH$_2$Cl$_2$ (B) The ^{1}H-NMR spectrum of [Mn^{III}(TMP)Cl] (**2c**) in CDCl$_3$.

2.3.4 Synthesis of Chromium(III) Salen Complexes [Cr^{III}(salen)Cl] (3d-3e)
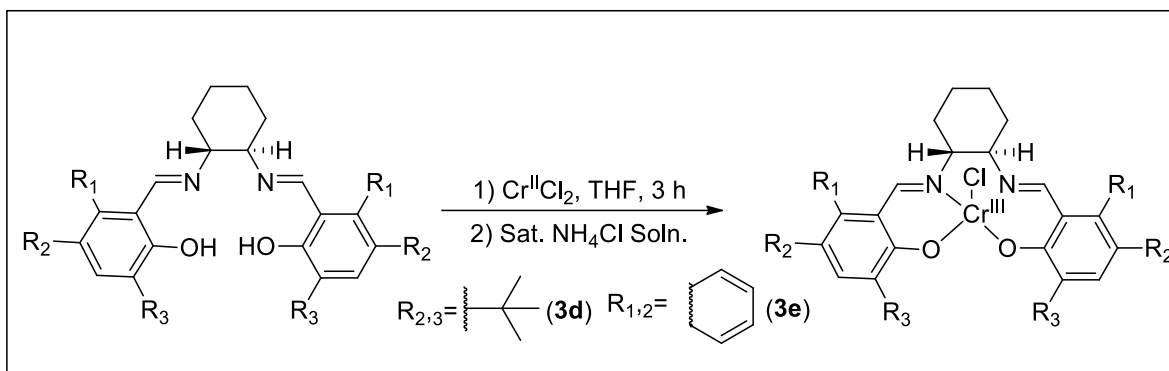
Scheme 2-4. Synthesis of [Cr^{III}(salen)Cl] and [Cr^{III}(napthen)Cl] (**3d-e**).

A 25 mL round-bottom flask was charged with 20 mL of tetrahydrofuran (THF) and then 200 mg of salen free base ligand was added followed by degassing with argon gas for 10 minutes. Excess of anhydrous chromium(II) chloride (Cr^{II}Cl$_2$) (2 equiv.) was added in three portions to solution before oxidation of chromium ion. The reaction solution was then further degassed with argon for an additional 5 min, sealed with a rubber septum equipped with a disposable needle, and then stirred for 3 h. The reaction was then exposed to air, 10 mL of saturated ammonium chloride solution was added and left to stir for another 3 h. The precipitate was then collected via vacuum filtration. The orange-brown powdery product was then washed twice with 10 mL brine, 10 mL DI H$_2$O, and 10 mL cold EtOH to remove free ligand. The metal complex was then characterized using UV-Vis and ^{1}H NMR spectroscopies without further purification.

(*R,R*)-*N*,*N*'-Bis(3,5-di-*tert*-butylsalicylidene)-1,2-cyclohexanediaminochromium(III) chloride [Cr^{III}(salen)Cl] (3d)

Yield = 195.8 mg (76.1%)

UV-vis (CH$_2$Cl$_2$) λ$_{max}$/nm: 346, 434 (Figure 2-10A)

^{1}H-NMR (500 MHz, CDCl$_3$): δ, ppm: = -25.4 (s, 18H, tert-butyl), , -39.4 (d, 18H, tert-butyl) (Figure 2-10B)

(*R*,*R*)-*N*,*N*′-Bis-(2-hydroxy-1-naphthalidene)-1,2-cyclohexanediaminochromium(III) chloride [Cr^{III}(naphthen)Cl] (3e)

Yield = 160.5 mg (66.8%)

UV-vis (CH$_2$Cl$_2$) λ$_{max}$/nm: 327, 416, 435. (Figure 2-11A)

^{1}H-NMR (500 MHz, CDCl$_3$): δ, ppm: = (m, 8H, cyclohexane-H) (Figure 2-11B)
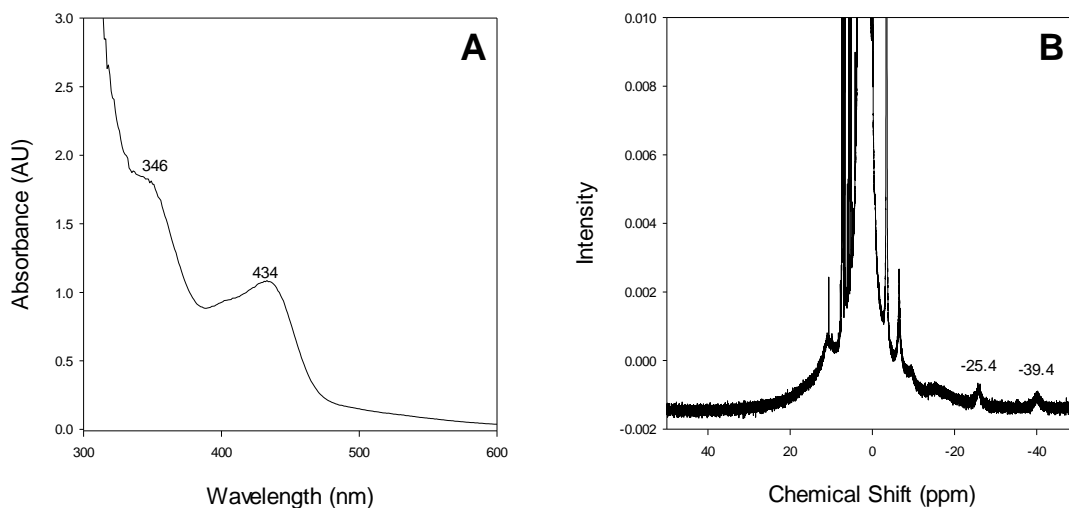
Figure 2-10. (A) The UV-Vis spectrum of [Cr^{III}(salen)Cl] (**3d**). (B) The ^{1}H-NMR spectrum of [Cr^{III}(salen)Cl] (**3d**) in CDCl$_3$.
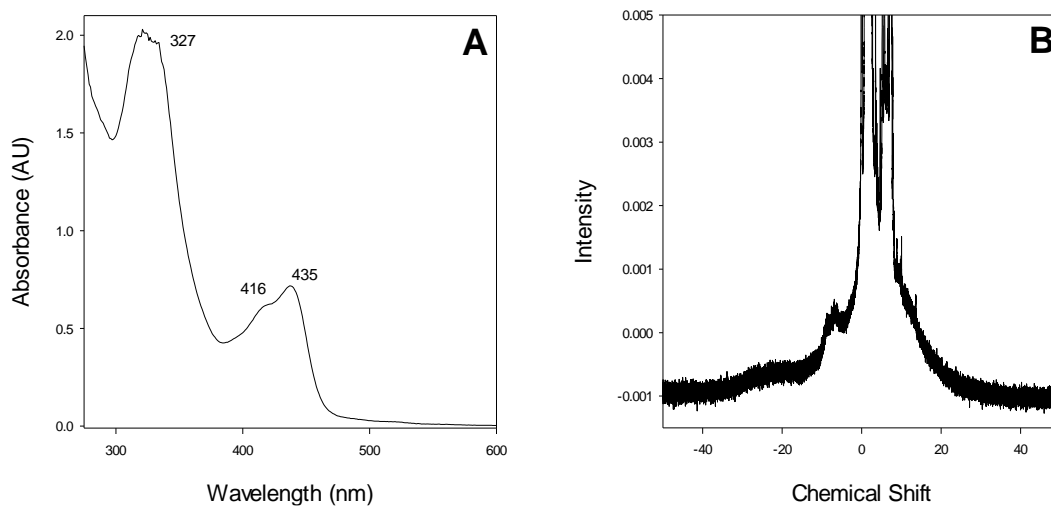
Figure 2-11. (A) The UV-Vis spectrum of [Cr^{III}(napthen)Cl] (**3e**). (B) The ^{1}H-NMR spectrum of [Cr^{III}(napthen)Cl] (**3e**) in CDCl$_3$.

2.3.5 Synthesis of Manganese(III) Salen Chloride Complexes [Mn^{III}(salen)Cl] (4d-e)
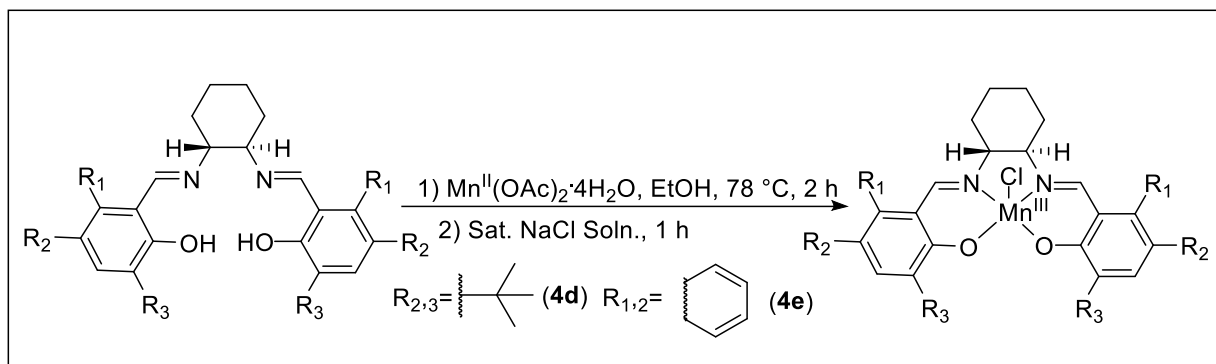
Scheme 2-5. Synthesis of [Mn^{III}(salen)Cl] and [Mn^{III}(napthen)Cl] (**4d-e**).

A 50 mL round-bottom flask was equipped with a reflux condenser and charged with 15 mL ethanol and 200 mg of salen ligand. An excess amount of manganese (II) acetate tetrahydrate [Mn^{II}(OAc)$_2$·4H$_2$O] (2 equiv.) was added to the flask and the reaction was then refluxed for 2 h and allowed to cool to rt. Upon reaching rt, a 10 mL of sat. sodium

chloride solution was added and allowed to stir in order to exchange the OAc axial ligand to Cl. The mixture was then cooled at 5°C to precipitate the product. The product was obtained using vacuum filtration, washed twice with 10 mL brine, 10 mL DI water, and 10 mL cold EtOH. The dark-brown powdery product was left overnight to dry in a desiccator. The product was then characterized using UV-Vis and ^{1}H NMR spectroscopies without further purification.

(*R,R*)-(−)-N,N′-Bis(3,5-di-tert-butylsalicylidene)-1,2-cyclohexanediaminomanganese(III) chloride[Mn^{III}(salen)Cl] (4d)

Yield = 195.8 mg (76.1%)

UV-vis (CH$_2$Cl$_2$) λ_{max}/nm: 322, 436, 498 (Figure 2-12A)

^{1}H-NMR (500 MHz, CDCl$_3$): δ, ppm: = -22.8, (s, 18H, *tert*-butyl), -27.0 (d, 18H, *tert*-butyl) (Figure 2-12B)

Manganese(III) (*R,R*)-N,N′-Bis-(2-hydroxy-1-naphthalidene)-(*R,R*)1,2-cyclohexanediamine chloride [Mn^{III}(naphthen)Cl] (4e)

Yield = 160.5 mg (66.8%)

UV-vis (CH$_2$Cl$_2$) λ_{max}/nm: 337, 443. (Figure 2-13A)

^{1}H-NMR (500 MHz, CDCl$_3$): δ, ppm: = -5.87, -7.12, -8.44 (t, 2H, cyclohexane-H), -13.5 - 38.1(m, 8H, cyclohexane-H). (Figure 2-13B)
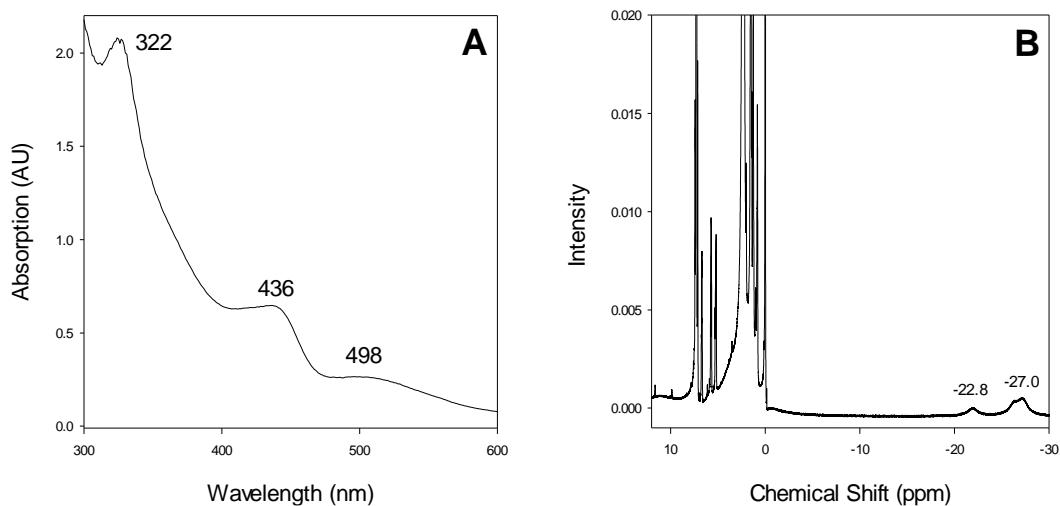
Figure 2-12. (A) The UV-Vis spectrum of [Mn^{III}(salen)Cl] (**4d**). (B) The ^{1}H-NMR spectrum of [Mn^{III}(salen)Cl] (**4d**) in CDCl$_3$.
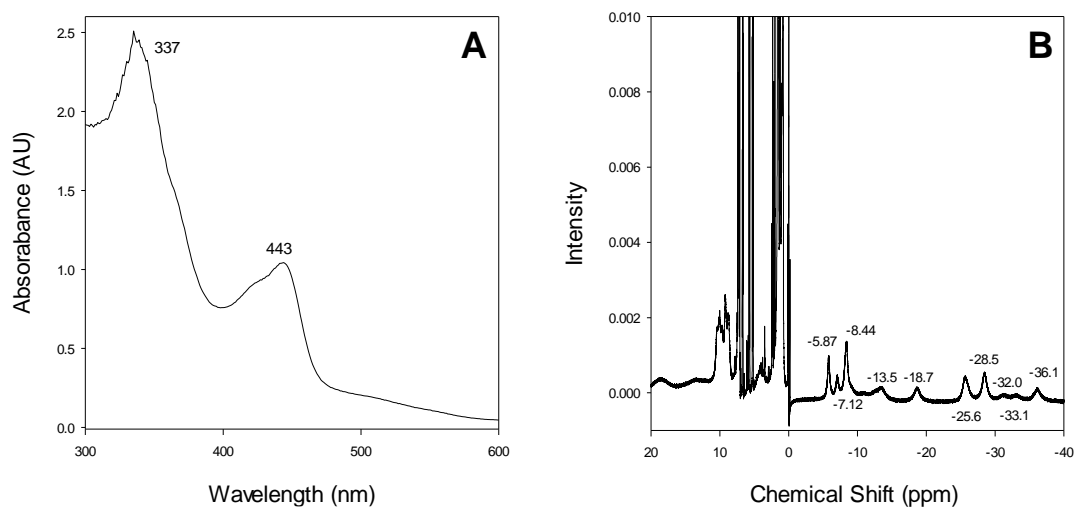
Figure 2-13. (A) The UV-Vis spectrum of [Mn^{III}(napthen)Cl] (**4e**). (B) The ^{1}H-NMR spectrum of [Mn^{III}(napthen)Cl] (**4e**) in CDCl$_3$.

CHAPTER 3

GENERATION AND OXIDATION KINETIC STUDIES OF MANGANESE(IV)-OXO PORPHYRIN INTERMEDIATES

3.1 Introduction

One of the most prominent illustrations of high-valent manganese-oxo species found in Nature is the oxygen-evolving complex (OEC), the active site of the photosystem II enzyme which is found in the thylakoid membranes of chloroplasts.[59] The complex consists of a Mn_4CaO cluster which aids in the oxidation of water using visible light during photosynthesis. The catalytic cycle of this cluster most likely involves a manganese-oxido species which is involved in the O-O bond formation step of water oxidation.[60] Manganese-oxo species have been utilized as catalysts in a plethora of different organic transformations.[15,61–63] In many of these transformations, the proposed reactive intermediates in the catalytic cycle are high-valent porphyrin-manganese(V)-oxo species.[46,51,64–66] Groves and colleagues also reported spectroscopic evidence of *trans*-dioxomanganese(V) porphyrin complexes where protonation yields reactive intermediates useful for catalytic transformations.[67] On the other hand, manganese(IV)-oxo porphyrins are less investigated in part due to their reduced reactivity, unlikely to serve as the primary oxidants for oxidative transformations. Previous studies have reported the characterization of porphyrin-manganese(IV) oxos using UV-Vis, electron paramagnetic resonance (EPR), X-ray absorption (EXAFS), infrared (IR), and Raman spectroscopies.[68–71] In 2019, Nam and coworkers provided evidence that manganese(IV)-oxo porphyrin complexes were able to activate C-H bonds of inert alkanes, including cyclohexane, to afford halogenated products.[72] Previous literature of kinetic studies of porphyrin-manganese(IV)-oxo

intermediates are restricted to primarily alkene epoxidation; moreover, there is a limited kinetic investigation on the oxidation of heteroatom compounds such as organic sulfides.[73]

In this chapter, we will discuss the photochemical and chemical generation of reactive manganese(IV)-oxo intermediates bearing different electron demanding ligands as demonstrated in Scheme 3-1.[74] The substituents located on the *ortho* positions of the *meso* phenyl groups of the porphyrin macrocycle allowed for the ligand systems (**a-c**) to adopt a sterically encumbered molecular geometry. The geometry of the aryl substituent prevented the generation of μ-oxo dimers which were not of interest in this particular study. The order of the most electronic demanding to the least demanding porphyrin free ligand was TPFPP (**1a**), TDFPP (**1b**), and TMP (**1c**) respectively. The rate constants for the OAT events of porphyrin-manganese(IV)-oxo intermediates with organic sulfides in acetonitrile media were on average a magnitude greater than activated hydrocarbons. The kinetic studies as well as the spectral behavior of the intermediates provided insightful information on the mechanisms at play in terms of the reactivity pathways of the manganese(IV)-oxo species in the sulfide oxidative transformations. The inverted reactivity pattern of the second-order rate constants where the most electron-demanding ligand systems showed higher reactivity than the electron-donating systems suggested a disproportionation pathway for hydrocarbon substrates. In addition, the spectroscopic detection of a transient [Mn^{II}(Por)Cl] provides evidence of a direct OAT event.
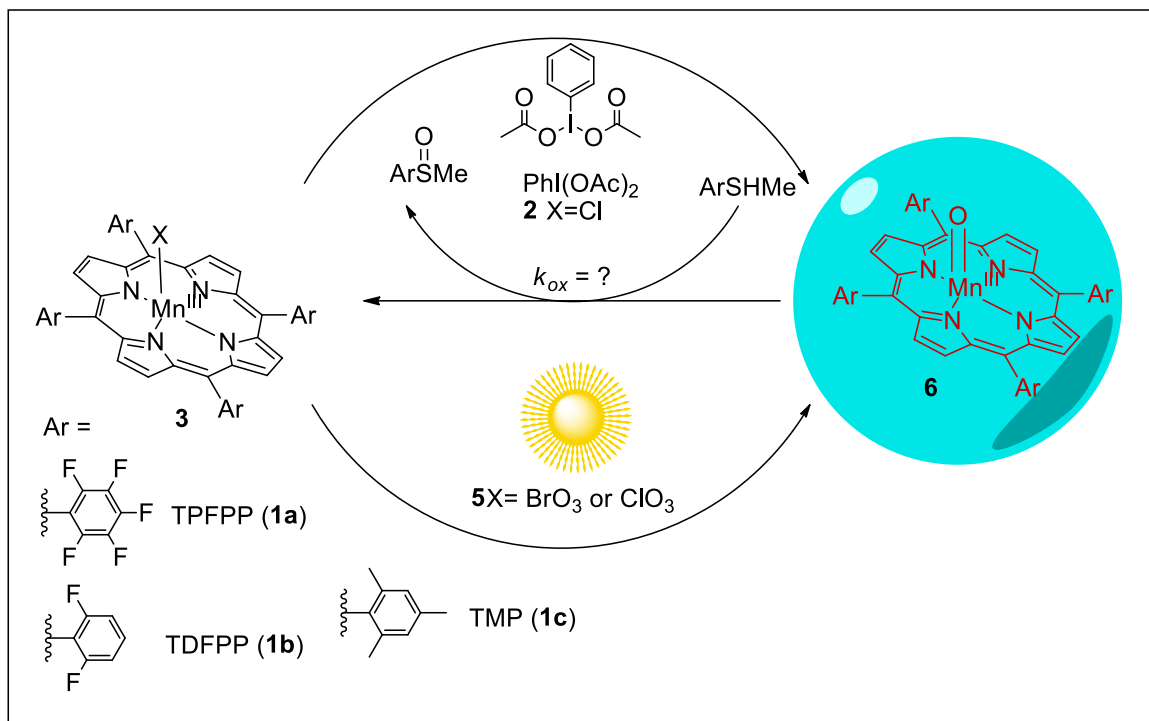
Scheme 3-1. Photochemical and chemical generation of porphyrin-manganese(IV)-oxo derivatives and kinetic studies of sulfide oxidation.

3.2 Results and Discussions

3.2.1 Photochemical Generation of Porphyrin-Manganese(IV)-Oxo Intermediates and Stoichiometric Oxidation

Axial ligand exchange reaction of the porphyrin complexes with 2-fold excess $Ag(XO_3)$ (X = Cl and Br) in anaerobic CH_3CN solutions generated the corresponding haloate salts $[Mn^{III}(Por)(XO_3)]$ as shown in Scheme 3-2. The formation of the chlorate or bromate salts was verified using UV-Vis spectroscopy (Figure 3-1).
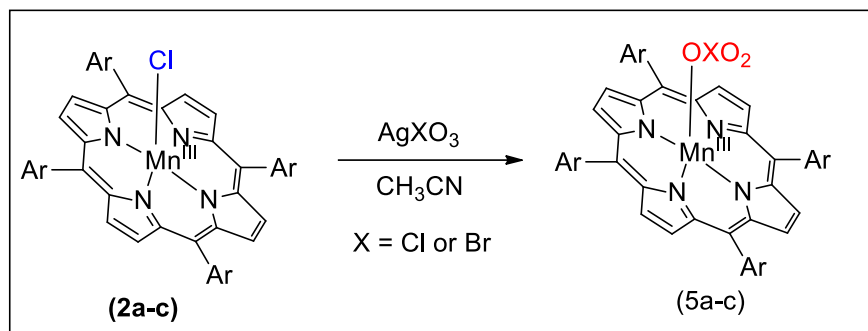
Scheme 3-2. Axial ligand exchange reaction from [Mn(Por)Cl] to [Mn(Por)XO$_3$].
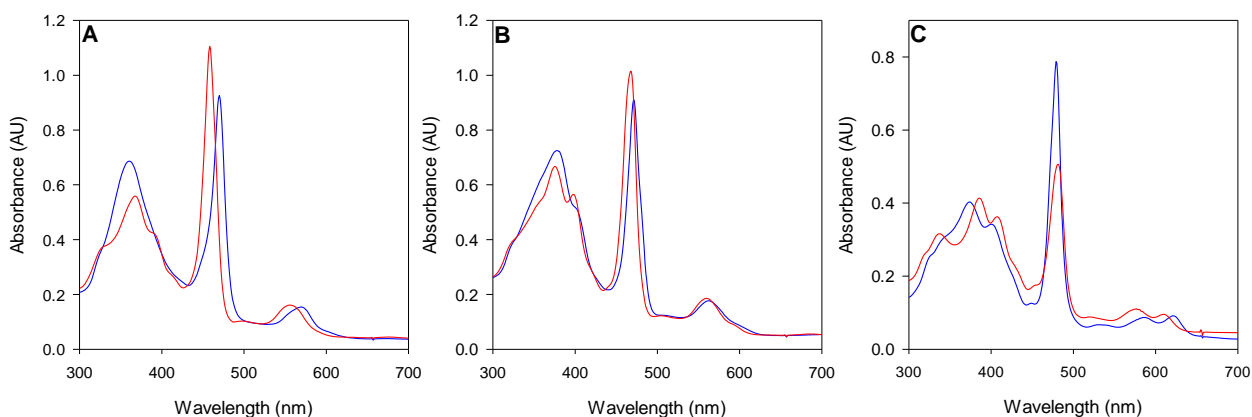
Figure 3-1. Axial ligand exchange monitored by UV-visible spectroscopy: (A) Mn^{III}(TPFPP)Cl (**2a**, blue) and [Mn^{III}(TPFPP)(ClO$_3$)] (**5a**, red) in CH$_3$CN; (B) Mn^{III}(TDFPP)Cl (**2b**, blue) and Mn^{III}(TDFPP)(ClO$_3$) (**5b**, red) in CH$_3$CN. (C) Mn^{III}(TMP)Cl (**2c**, blue) and Mn^{III}(TMP)(ClO$_3$) (**5c**, red) in CH$_3$CN.

Visible light irradiation of the chlorate complex [Mn^{III}(TPDPP)(ClO$_3$)] **5c** in CH$_3$CN using SOLA Engine (120 W) caused changes in the absorption spectra with clearly resolved isosbestic points at 550, 442, 390, and 320 nm as presented in Figure 3-2. Isosbestic points suggest the direct formation of the oxo species with no accumulation of other intermediates.
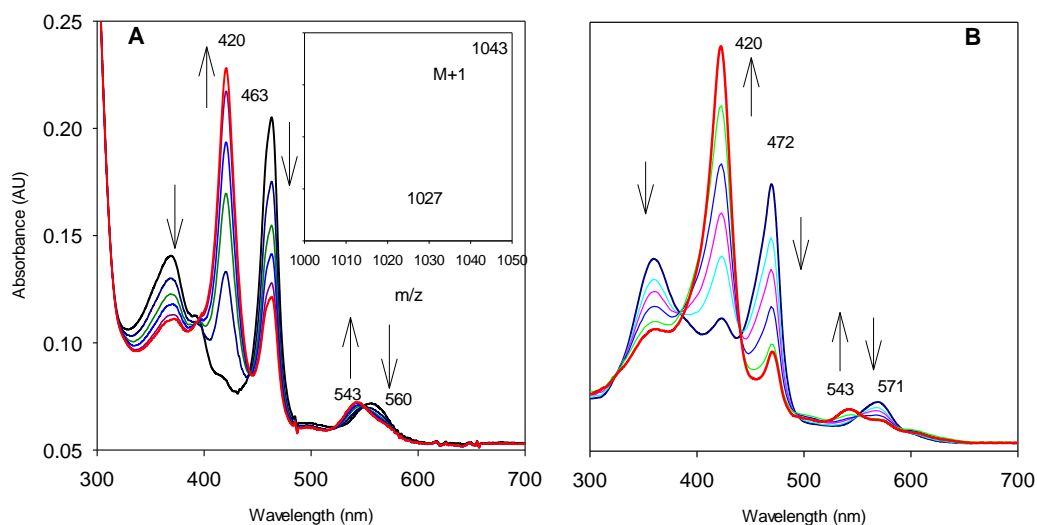
Figure 3-2. (A) Time-resolved spectra of **6a** following photolysis of **5a** with visible light (120 W) in CH₃CN solution at 23 ± 2 °C over 5s; Inset showing the ESI-MS of **6a** in a positive mode. (B) Time-resolved spectra of **6c** following oxidation of **2c** with PhI(OAc)₂ (10 equiv.) over 4s in CH₃CN.

[Mn^III(TPFPP)Cl] was transformed into the new species **6a** within the time frame 5 s, and the absorption spectrum showed a blue-shifted and heightened Soret band at 420 nm and a Q-band at 540 nm which is characteristic of [Mn^V(TPFPP)(O). In a similar manner, the bromate complex, [Mn^III(TPFPP)(BrO₃)], upon irradiation quickly generated the same intermediate **6** using low-powered visible light. The photo-generated **6a** was metastable, having a half-life of *ca*. 5 min, which was then furthered characterized *via* ESI-MS using a positive mode as shown in the inset of Figure 3-2A. The MS spectrum revealed a peak at a mass-to-charge ratio (*m/z*) at 1043 corresponding to the theoretical [M+H]⁺ of [Mn(TPFPP)(O)]. The peak at 1047 shifted to 1027 upon decomposition of **6a** representing a transient species [Mn(TPFPP)]⁺. Based on the UV-Vis absorption and ESI-MS spectra,

the intermediate was ascertained to be [Mn^{IV}(TPFPP)(O)]. As previously mentioned, the same oxo species **6a** were generated by chemical oxidation of **1a** with excess PhI(OAc)$_2$ (10 equiv.), showing the same spectral behavior which is representative of porphyrin-manganese(IV) intermediates (Figure 3-2B).

Similarly, formation of [Mn^{IV}(TDFPP)(O)] (**6b**) and [Mn^{IV}(TMP)(O)] (**6c**) was also achieved using photolysis of the corresponding [Mn^{III}(Por)(ClO$_3$)] salts as displayed in Figure 3-3A and B, respectively. In all cases, there was no evidence of photodecomposition of the complexes in the presence of visible light irradiation using UV-Vis spectroscopy. In the case of [Mn^{IV}(TMP)(O)] (**6c**), only 60% formation of the intermediate under visible light irradiation was detected using UV-Vis spectroscopy for the initial manganese(III) salt precursor. The excellent efficiency of photolysis of porphyrin systems bearing more electron-withdrawing ligands i.e., TFPPP and TDFPP, was attributed to the polar nature of the O-X bond of the axial ligand.
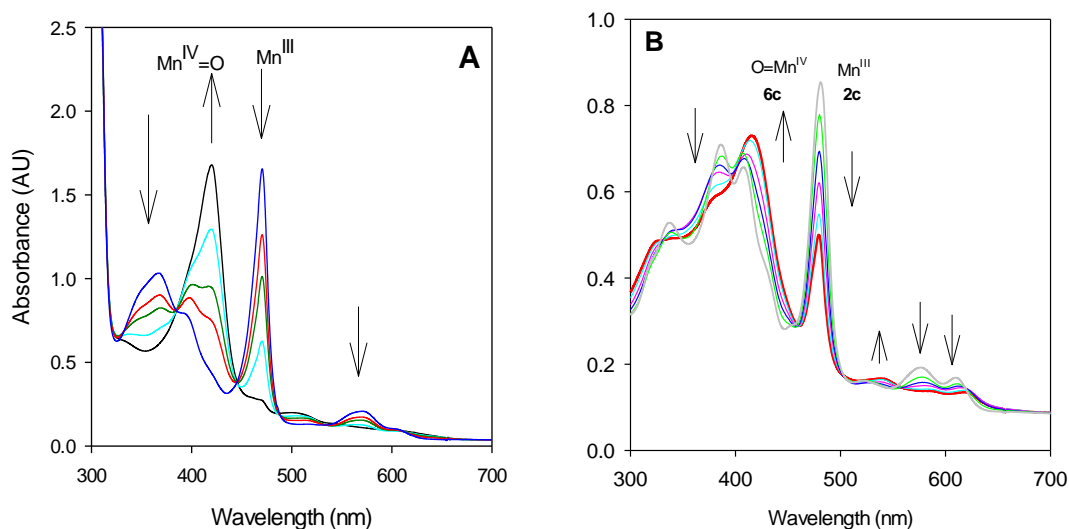
Figure 3-3. (A) Time-resolved spectra for generation of [Mn^{IV}(TDFPP)O] (**6b**) by visible light irradiation of [Mn^{III}(TDFPP)ClO$_3$] (**5b**) over 3 s after axial ligand exchange of [Mn^{III}(TDFPP)Cl] (**2b**) with AgClO$_3$. (B) Time-resolved spectra for generation of [Mn^{IV}(TMP)(O)] (**6c**) by visible light irradiation of [Mn^{III}(TMP)ClO$_3$] (**2c**) over 30 s after axial ligand exchange of [Mn^{III}(TMP)Cl] (**1c**) with AgClO$_3$ in the CH$_2$Cl$_2$ solution.

In addition, control experiments were conducted in the absence of visible light indicating that no species **6a** was generated. Non-coordinating solutions such as CH$_2$Cl$_2$ displayed similar results to CH$_3$CN; however, in the presence of strongly coordinating media such CH$_3$OH and H$_2$O, there was no formation of [Mn^{IV}(Por)(O)] (**6**). The results of the solvent effects study suggest that the weakly coordinating chlorate counter ion in the axial position of the complex can be readily dissociated in a strongly coordinating solvent such as MeOH. The photochemistry involved in the generation of [Mn^{IV}(TPFPP)(O)] (**6**) can be rationalized by the homolytic cleavage of the O-X halogen bond in the axial ligand

of the chlorate or bromate precursors (**5**). Likewise, chemical generation of the porphyrin-manganese(IV)-oxo intermediates in the study was ascribed to a possible comproportionation reaction, where the initially formed $[Mn^V(Por)(O)]$ reacts with residual manganese(III) complex. In previous literature, the use of strong oxidizing reagents such as mCPBA or NaClO for the oxidation of manganese(III) complexes generally results in the formation of a higher valent manganese(V)-oxo intermediate.[46,51,64]

In this study, the chemical conversion of the electron-withdrawing **2a** to manganese(V)-oxo was slow in part because of the reduced oxidative ability of $PhI(OAc)_2$. The comproportionation reaction is under thermodynamic control, thus the $[Mn^{IV}(Por)(O)]$ species was generated from the fast comproportionation of $[Mn^V(Por)(O)]$ with residual manganese(III) complex. Groves and coworkers previously reported that $[Mn^V(Por)(O)]$ served as OAT agents in the oxidative conversion of organic substrates such as alkenes and hydrocarbons.[64] The photo-formed complexes served as a potent OAT agent with various thioanisoles as anticipated. Stoichiometric sulfide oxidations were then carried out where **6a** reacted with *ca.* 1.5 equiv. of $Ag(ClO_3)$ in anaerobic CH_3CN in the presence of visible light. Upon subsequent addition of a large excess of thioanisole, the reaction was allowed to stir for *ca.* 5 min under ambient conditions. GC analysis indicated the presence of a mixture of oxidized products (sulfoxide: sulfone = 76:24) in 63% yield, which was determined based on stoichiometric amounts of **6a** with thioanisole.

3.2.2 Sulfide Oxidation Kinetic Studies *via* [Mn^{IV}(Por)(O)]

In this investigation, the oxidation kinetic studies for porphyrin-manganese(IV) oxo intermediates towards various thioanisoles were conducted. For comparison, several olefins and activated paraffins were also included as organic substrates. A stopped-flow

kinetic instrument using a three-syringe setup was used to measure the fast kinetics of sulfide oxidations. [Mn^{III}(Por)Cl] (**2**) in anaerobic CH_3CN solution was rapidly mixed with *ca.* 10 equiv. of $PhI(OAC)_2$. A delay of 1 to 5s was set on the stopped-flow system to allow for the generation of the manganese(IV)-oxo intermediate (> 90% conversion). The solution of [Mn^{IV}(Por)(O)] was then combined with a solution consisting of excess reductant. In the absence of substrate, the time-resolved spectra in Figure 3-4A showed complete conversion from [Mn^{IV}(TMP)(O)] to regenerate manganese(III) porphyrin complexes with no direct evidence for the generation of a manganese(II) transient.

The reaction between porphyrin-manganese(IV) intermediate and sulfides in this study indicated a two-electron transfer process; however, there is the possibility of different mechanistic oxidation pathways taking place. In order for the two-electron transfer process to occur, the rates of the aerobic oxidation reactions of the [Mn^{II}(Por)] product proceeding sulfide oxidation must be higher than the rate of reaction [Mn^{IV}(Por)(O)] towards sulfide (OAT event). On the other hand, if the rate of the OAT event is higher than the rate of aerobic oxidation then the accumulation of [Mn^{II}(Por)] species (**7**) would be spectroscopically detectable. To further investigate this process, we examined the kinetics of the oxidation of the most reactive sulfide, 4-flurothioanisole, with an extremely high concentration (400 mM) under ambient conditions.
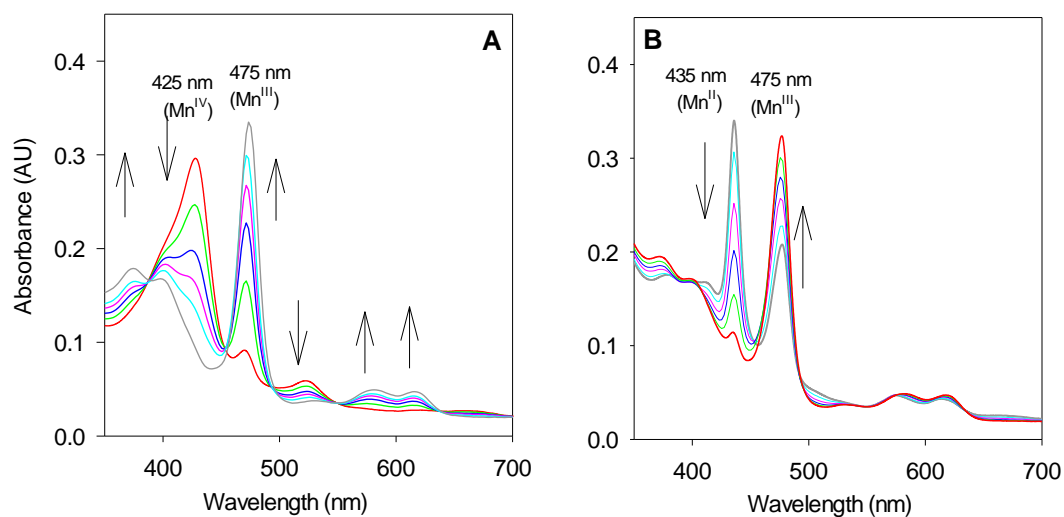
Figure 3-4. (A) Time-resolved spectra of [Mn^{IV}(TMP)(O)] (**6c**) reacting in CH$_3$CN solution with 4-chlorothioanisole (50 mM) over 40vs at 23 ± 2 °C; (B) Time-resolved spectra of **2a** reacting with 4-fluorothioanisole (400 mM) in anaerobic CH$_3$CN solution over 80 s. Inset showing the kinetic trace at 435 nm of Mn^{II} intermediate (**7c**).

As displayed in Figure 3-4B, [Mn^{IV}(TMP)(O)] was instantly transformed to form to a transient [Mn^{II}(TMP)] (**7c**) species which was rapidly oxidized by air to form [Mn^{III}(TMP)(X)] (where X = X-type ligand i.e. chloride). Hoshino and colleagues previously showed that an intermediate [Mn^{II}(TPP)] (TPP = 5,10,15,20-tetrakisphenylporphyrin) had a λ_{max} at 433 nm.[75] In this study, the λ_{max} of the intermediate was at 435 nm, matching the spectral signature of a [Mn^{II}(TMP)] (**7c**) species. Analogously, the presence of sulfide, serving as a potent sigma-donor ligand, could stabilize the Mn^{II} product. Our group previously reported that photolysis of dimanganese(III) μ-oxo bis-porphyrins in the presence of triphenylphosphine or pyridine donor ligands stabilized Mn^{II} products.[76]

With respect to kinetic studies of **6**, the decay of the Soret band at $\lambda_{max} = 420$ nm (**6a**), 422 nm (**6b**), and 425 (**6c**) corresponding to the $[Mn^{IV}(Por)(O)]$ species was measured during the reaction of various organic substrates as reductants. The linear regression of the kinetic plots provided second-order rate constants which gave insights into the reactivity of the generated species. A representative kinetic plot showing the k_{obs} for the OAT event of $[Mn^{IV}(TMP)(O)]$ as a function of concentrations of 4-chlorothioanisole is shown in Figure 3-5. The apparent second-order rate constant for the oxidations of $[Mn^{IV}(Por)(O)]$ systems with other organic reductants were also procured as detailed in Table 3-1.
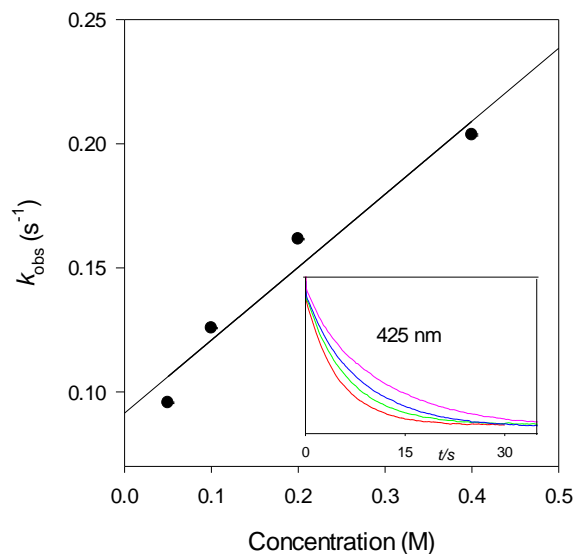
Figure 3-5. Kinetic plot of the observed rate constants for the reaction of $[Mn^{IV}(TMP)(O)]$ (**6c**) versus the concentrations of 4-chlorothioanisole. Inset showing traces at 425 nm for decaying of $[Mn^{IV}(TMP)(O)]$ (**6c**) with 4-chlorothioanisole at various concentrations.

Table 3-1. Second-order rate constants for manganese(IV)-oxo species **6**.[a]

Substrate	k_{ox} (M^{-1}s^{-1}) × 10		
	[Mn^{IV}(TPFPP)O]	[Mn^{IV}(TDFPP)O]	[Mn^{IV}(TMP)O]
	6a	**6b**	**6c**
thioanisole	17.4 ± 3.0	4.2 ± 0.1	3.5 ± 0.7
4-fluorothioanisole	20.2 ± 1.0	16.9 ± 0.9	8.8 ± 0.7
4-chlorothioanisole	2.3 ± 0.8		1.8 ± 0.4
4-methylthioanisole	5.8 ± 0.7		1.2 ± 0.1
4-methoxylthioanisole	3.2 ± 0.4	1.0 ± 0.1	0.7 ± 0.2
cis-stilbene	1.5 ± 0.1	0.40 ± 0.1	0.20 ± 0.07
cyclohexene		0.62 ± 0.06	0.24 ± 0.05
ethylbenzene	7.1 ± 0.3	2.0 ± 0.1	
ethylbenzene-d_{10}	0.72 ± 0.09		

[a]CH$_3$CN at 23 ± 2 ºC, reported values are the average of 2-3 runs with a deviation of 2σ.

The second-order rate constants of the oxidation reactions of [Mn^{IV}(Por)(O)] with various substrates followed the anticipated reactivity pattern where **6a** > **6b** > **6c**. The more electron-withdrawing systems such as TPFPP reacted readily with a given reductant compared to the TMP system. Normally, we would detect notable rate acceleration of sulfide reactivity *via* the electrophilic metal oxo-species because of the superior nucleophilicity and approachability of the sulfur atom for oxidation compared to alkenes and activated alkanes. However, in this study, the k_{ox} values imply that there was not a significant rate acceleration of sulfoxidation by porphyrin-manganese(IV)-oxo

intermediates. As shown in Table 3-1, the organic sulfides presented similar reactivities in comparison to *cis*-stilbene and cyclohexene. The rate constant for ethylbenzene and ethylbenzene-d_{10} *via* [Mn^{IV}(TPFPP)(O)] yielded a KIE of $K_H/K_D = 9.9$. The KIE value suggests that the rate-determining step of C-H activation necessitates an H atom abstraction from the benzylic C-H. Likewise, KIE values of 11 and 12 were also reported by Nam and coworkers for the oxidation of ethylbenzene using [Mn^{IV}(TMP)(O)] and [Mn^{IV}(TDCPP)(O)].[72]

In addition, the electronic properties of the transition state of the benzylic sulfur of the thioanisoles during oxidation were explored using the abovementioned kinetic measurements. The second-order rate constants for the *para*-substituted thioansioles showed a discrete substituent dependence. For example, the rate constants were smaller for sulfides bearing electron-rich moieties in the *para*-position of the phenyl group of thioanisoles. The logk_{rel} ($k_{rel} = k$(Y-thioanisoles/k(thioansiole) where Y-thioansiole = 4-MeO, 4-Me, 4-F and 4-Cl) versus Hammett σ constants plot showed a near-linear correlation (R = 0.80) (Figure 3-6). The reaction constant (ρ) of the plot was determined to be 1.73 ± 0.7, which indicated that there was a development of negative charge at the transition state of the sulfur during the rate-determining step (RDS).
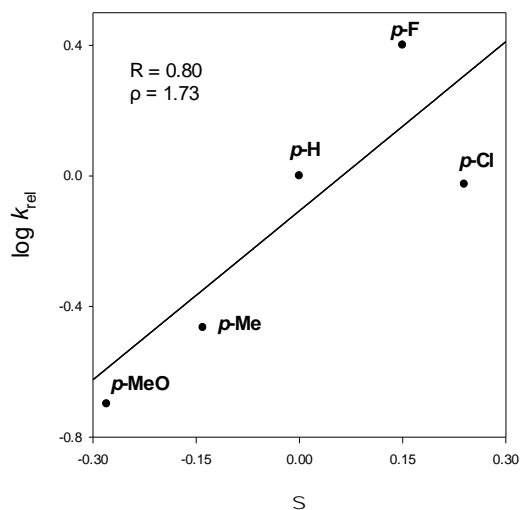
Figure 3-6. Near-linear Hammett plot for the rate constants for reactions of $[Mn^{IV}(TMP)(O)]$ (**6c**) with Hammett σ constants, where the labels represent the substituent on thioanisoles.

The majority of experimental results in this study could be explained by the possible mechanism demonstrated in Scheme 3-3. Porphyrin-manganese(IV)-oxo intermediates most likely serve as a direct OAT agent (pathway **a**). The oxygen transfer event occurs from the electrophilic manganese ion to sulfide with a possible radical intermediate. The spectral signature shown in Figure 3-4B suggests that the manganese(II) species would undergo aerobic oxidation to generate the observed manganese(III) complex. In addition, direct OAT is also supported by the reactivity series of **6a** > **6b** > **6c**. The direct OAT pathway becomes less kinetically favorable when less reactive substrates such as activated paraffins are involved. Therefore, the disproportionation reaction of $[Mn^{IV}(Por)(O)]$ to form $[Mn^{V}(Por)(O)]$ as the primary OAT agent becomes the predominant reaction pathway (pathway **b**).
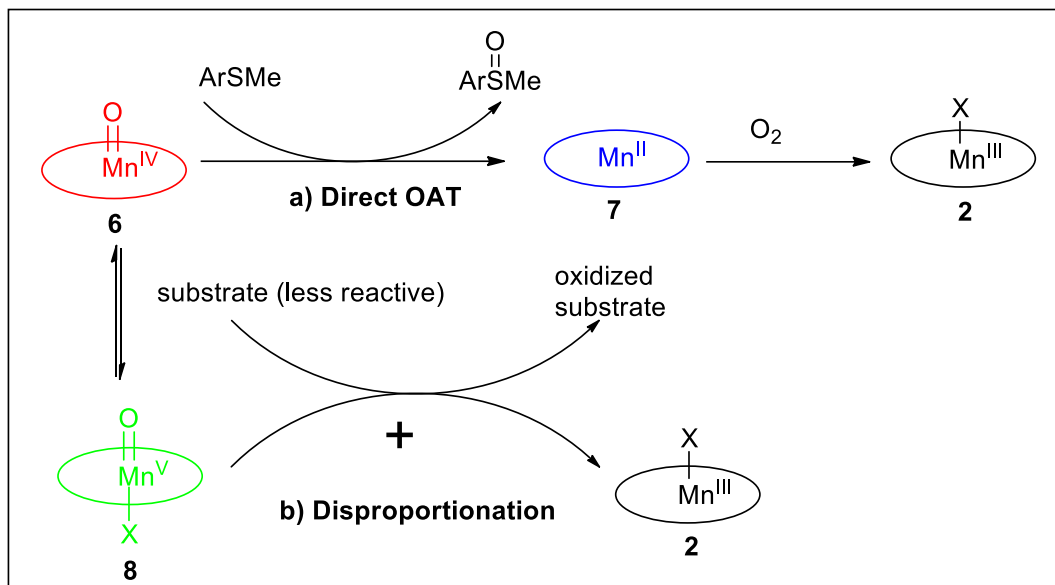
Scheme 3-3. A proposed OAT mechanism of species **3** involving (a) direct OAT to

sulfides and (b) alternative disproportionation mechanism.

In addition, we conducted several kinetic experiments to obtain the apparent pseudo-first-order rate constant for the reaction of **6a** in the presence of manganese(III) hydroxide precursor at different concentrations. As the concentration of **6a** increases, the observed rate constant decreases as shown in Figure 3-7. The results convey that, in the absence of substrate, there is a suppression effect for the reaction of $[Mn^{IV}(Por)(O)]$ with $[Mn^{III}(Por)(X)]$ resulting in an attainable disproportionation mechanism.
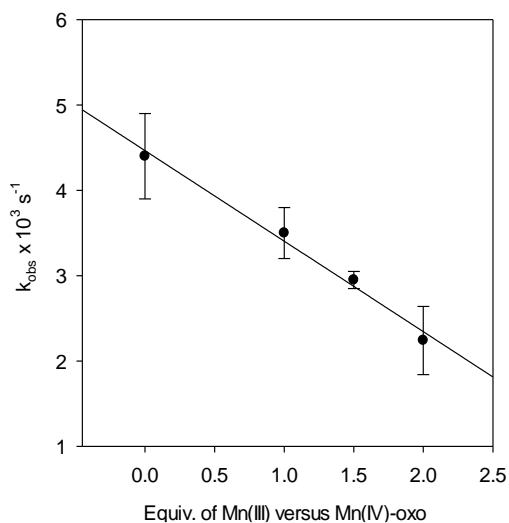
Figure 3-7. Observed apparent pseudo-first-order rate constants for reaction of **6a** in CH₃CN in the presence of Mn(III) hydroxide precursor at varied concentrations (equivalency of concentration of **6a**).

We previously showed that a disproportionation mechanism could also explain the reactivity pattern of laser flash photolysis (LFP) generated manganese(IV)-oxo porphyrin.[51] There is the possibility that both manganese(V)-oxo and manganese(IV)-oxo served as oxidizing agents in the presence of reactive sulfide; however, the inverted reactivity pattern implies that the primary OAT agent was indeed $[Mn^{IV}(Por)(O)]$.

3.2.3 Catalytic Studies of Sulfide Oxidation Reactions

In the present work, we have found that manganese(III)-porphyrins can expeditiously catalyze the oxidation of aryl sulfides. As shown in Table 3-2, thioanisoles in methanolic solutions can be oxidized with near-quantitative conversions and excellent chemoselectivity for sulfoxide over the over oxidized product, sulfones. The minute amounts of sulfone are produced because of the over oxidation of sulfoxide under standard

turnover conditions. In the control experiments using PhI(OAc)$_2$ and water without catalyst, there was no significant accumulation of oxidized products (< 1% by GC-MS).

Table 3-2. Catalytic oxidation of thioanisoles by manganese(III) porphyrins (**2**) and PhI(OAc)$_2$.[a]

Entry	Catalyst	Substrate	Time (h)	Conv. (%)	Product	Selectivity%
1	Mn^{III}(TPFPP)Cl		1.5	100		95:05
2	Mn^{III}(TDFPP)Cl		1.5	100		92:08
3	Mn^{III}(TMP)Cl		2	100		95:05
4			1.5	100		88:12
5			2	100		85:15
6			1	94		85:15
7			1	100		93:07
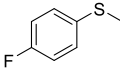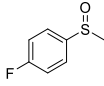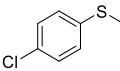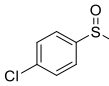
[a] All reactions were conducted in CH$_3$OH (2 mL) at *ca*. 23 °C with 1.5 equiv. of PhI(OAc)$_2$ (0.75 mmol), substrate (0.5 mmol, 0.2 mol% catalyst in the presence of H$_2$O (4.5 μL); sulfoxide and small amounts of sulfone were detected by GC analysis of the crude reaction mixture.

Competition studies of the sulfoxidations catalyzed by porphyrin-manganese(III) systems (**2**) with PhI(OAc)$_2$ were conducted in order to investigate the nature of the active oxidant species formed during the catalytic cycle. Approximately 100 equiv. of PhI(OAc)2 (0.1 mmol) was used in the competition studies to maintain conversion <20% sulfoxide and the quantities of oxidized products were determined using GC-MS analysis. With near-quantitative conversions, the thioanisoles were transformed to the corresponding sulfoxide without over-oxidation to sulfone. The relative rate constants (k_{rel}) were determined from direct kinetic studies with **6** and catalytic competition reactions (Table 3-3).

Table 3-3. Relative rate constants from kinetic studies and competition catalytic oxidations

Porphyrin	Substrates	Method	k_{rel}
TPFPP	p-F-PhSMe/PhSMe	Kinetic results	1.16
		$PhI(OAc)_2$	0.45
TPFPP	p-Cl-PhSMe/PhSMe	Kinetic results	0.13
		$PhI(OAc)_2$	0.18
TPFPP	p-Me-PhSMe/PhSMe	Kinetic results	0.18
		$PhI(OAc)_2$	1.96
TPFPP	p-MeO-PhSMe/PhSMe	Kinetic results	0.33
		$PhI(OAc)_2$	5.98
TMP	p-F-PhSMe/PhSMe	Kinetic results	2.50
		$PhI(OAc)_2$	0.44
TMP	p-Cl-PhSMe/PhSMe	Kinetic results	0.51
		$PhI(OAc)_2$	0.16
TMP	p-Me-PhSMe/PhSMe	Kinetic results	0.34
		$PhI(OAc)_2$	2.37
TMP	p-MeO-PhSMe/PhSMe	Kinetic results	0.29
		$PhI(OAc)_2$	6.42

[a] A reaction solution containing equivalent amount of two substrates e.g., thioanisole (0.2 mmol) and substituted thioanisole (0.2 mmol), manganese(III) porphyrin catalyst (1 μmol) and an internal standard of 1,2,3-trichlorobenzene was prepared in CH_3OH (2 mL)

iodobenzene diacetate PhI(OAc)$_2$ (0.1 mmol) was added with 4.5 μL H$_2$O, and the mixture was stirred for ca. 10 to 15 min at $23 \pm 2\,^{\circ}$C.

[b] Relative ratios of absolute rate constants from kinetic results with manganese(IV)-oxo porphyrin complexes (**6**) and for competitive oxidations with various manganese(III) porphyrin catalysts at ambient temperature, All competition ratios are averages of 2-3 determinations with standard deviations smaller than 10% of the reported values.

As shown in Table 3-3, the ratios of absolute rate constants from the kinetic data were different than the oxidation ratios from the catalytic competition oxidation reactions of the two substrates in two different systems in this study. Specifically, 4-fluorothioanisole exhibited the highest reactivity in kinetic studies, but 4-methoxythioanisole was the most reactive under catalytic conditions. The results suggest that the observed [Mn^{IV}(Por)(O)] species **6** in the aforementioned kinetic studies is most likely not the active metal-oxo oxidant under catalytic turnover conditions.

Upon examination the linear free-energy analysis for competitive oxidations of the series of substituted thioanisoles (Figure 3-8), we propose a different oxidant involved in the catalytic oxidation instead of the porphyrin-manganese(IV) oxo intermediate. The Hammett plot shows a linear correlation (R = 0.91) of logk_{rel} versus Hammett σ^+ constants. The reaction constant (ρ^+) was $-(1.61 \pm 0.42)$, suggesting the development of positive character on the benzylic sulfur in the transition state of the RDS. We previously showed that [Mn^{III}(TPFPP)Cl]-catalyzed oxidation of substituted styrene showed a lower reaction constant of ($\rho^+ = -0.42$).[77] The following Hammett substituent correlation analysis indicates that the observed porphyrin-manganese(IV)-oxo species is improbable to serve as the

reactive metal-oxo species during the catalytic cycle. Although it was not spectroscopically observed, the principle oxidant is anticipated to be a higher valent [Mn^V(Por)(O)] (**8**) species.
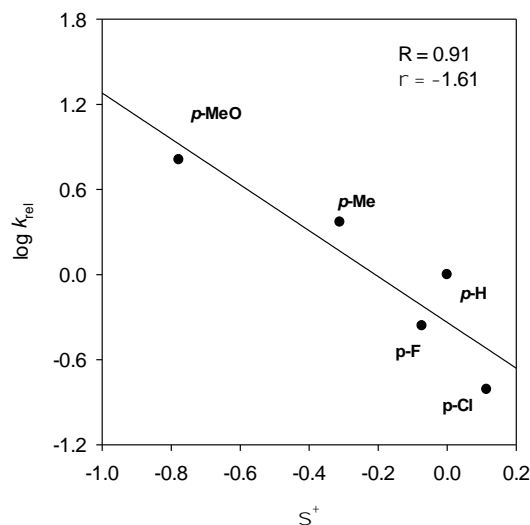
Figure 3-8. Hammett correlation studies (log k_{rel} vs σ^+) for the [Mn^{IV}(TMP)(Cl)]-catalyzed oxidation of substituted thioanisoles by $PhI(OAc)_2$ in CH_3CN at 23 ± 2 °C.

3.3 Conclusion

In closing, we have reported the formation of manganese(IV)-oxo porphyrins with different electronic demands which could be used for selective sulfide oxidations. Notably, we have developed a photochemical approach that implements visible light ligand cleavage reaction of manganese(III) chlorate and bromate precursors to generate manganese(IV)-oxo porphyrins. The oxidation kinetics of the sulfide reactions using porphyrin-manganese (IV)-oxo intermediates exhibited atypical low reactivity towards sulfide activation. The reactivity series for the porphyrin-manganese(IV)-oxo species was TPDPP > TDFPP > TMP which is anticipated for electrophilic metal-oxo oxidants based on the electron-withdrawing nature of the porphyrin ligands. The Hammett analysis from the kinetic

studies generated a near-linear correlation, suggesting a development of a negative charge on the sulfur at the transition state of the RDS. The relatively small second-order rate constants indicate [Mn^{IV}(Por)(O)] species likely undergo a direct OAT event through a transient [Mn^{II}(Por)] species that was spectroscopically detected. The catalytic and competition sulfide oxidation using porphyrin-manganese(III) complexes and PhI(OAc)$_2$ in this study reveals that the manganese(IV)-oxo species is unlikely to act as the major oxidant. Additional experimental studies are being undertaken in our laboratory to spectroscopically characterize these active intermediate as well as O^{18}-isotopic labeling investigations.

CHAPTER 4

VISIBLE LIGHT FORMATION OF CHROMIUM(V)-OXO SALEN COMPLEXES AND MECHANISTIC ILLUCIDATION OF CATALYTIC SULFIDE OXIDATION

4.1   Introduction

Metallosalen complexes (salen =*N,N'*-bis(salicylideneethylenediamine) have been extensively used as catalysts for organic transformations, especially asymmetric oxidations.[38,78,79] As discussed in Chapter 1, metallosalens share similar structural features to metalloporphyrins in terms of catalytic capability, tetradentate binding pattern, and ability to coordinate to numerous transition metals.[79] Jacobsen and Katsuki, in the early 1990s, developed asymmetric salen-manganese(III) complexes to accomplish catalytic enantioselective epoxidations of alkenes.[36,37]

Although there has been great success with regards to catalytic oxidations involving metallosalen complexes, mechanistic studies of the active species of these transformations have been impeded in part due to the ephemeral nature of the intermediates.[79,80] Most of the mechanistic interpretations for OAT events are derived predominantly from the isolation and characterization of a single chromium(V)-oxo intermediate by Kochi and coworkers.[81] The use of visible light instead of oxidizing reagents serves as an environmentally sustainable means of generating reactive metal-oxo species. Higher temporal resolution and direct, real-time kinetic studies of oxidation reaction are a couple of advantages to photochemical reactions.[45,48,51] In addition, a consistent problem with chemically generated active intermediates is that the kinetics and overall equilibria are complex compared to photochemical generation.[82] In this investigation, we implemented

photo-induced ligand cleavage reactions to produce active high-valent salen-metal-oxo species in order to illuminate mechanistic pathways and identify the nature of the oxidant.[83] As demonstrated in Scheme 4-1, visible-light photolysis of photo-labile chromium(III) chlorate or bromate salts produced cationic salen-chromium(V)-oxo complexes supported by the renowned Jacobsen's ligand and a naphthalene derivative.
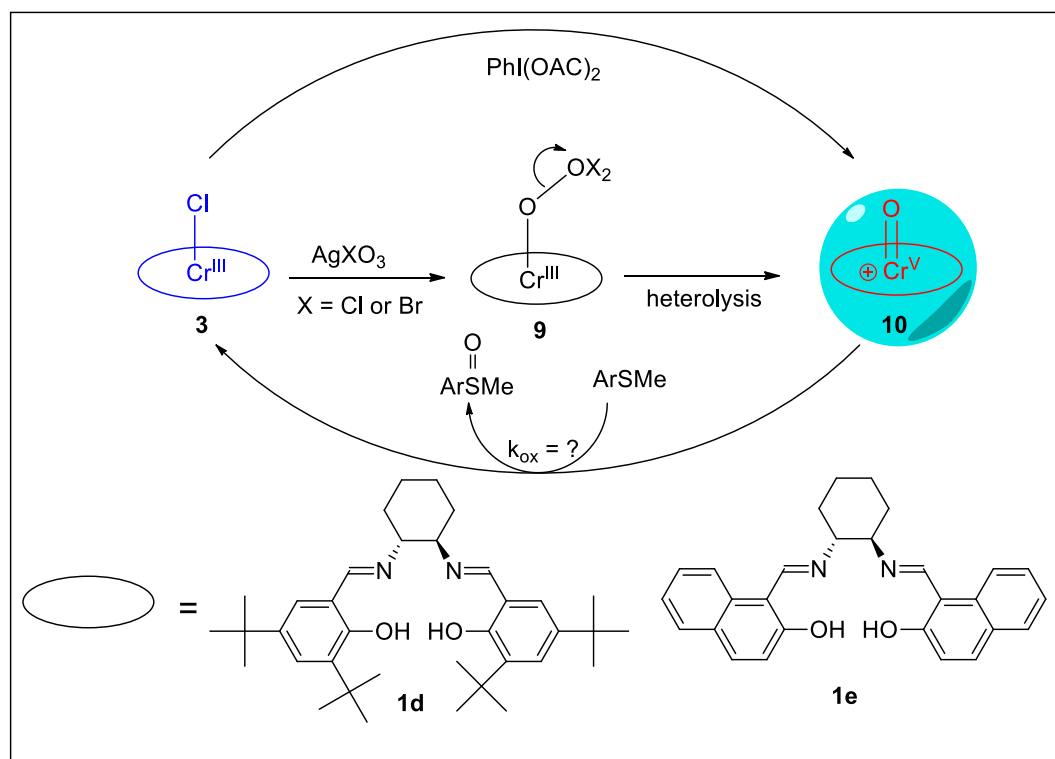
Scheme 4-1. Visible light-induced formation and chemical generation of salen-chromium(V)-oxo complexes.

The findings of this study indicated that the photochemical production of metal-oxo intermediates bearing salen ligands is not limited to metal-oxos supporting conventional porphyrin and corrole ligands. The rate constants for the oxidation reactions *via* salen-chromium(V)-oxo cations with organic sulfides were on average two orders of magnitude lower than the activated alkanes and alkenes suggesting strong coordination

between the sulfoxide and the electrophilic chromium(V) ion. The mechanistic pathways and the reactivities of the principal oxidant through the kinetic and competition catalytic oxidations indicate that the active intermediates are not identical under the two different methods.

4.2 Results and Discussion

4.2.1 Visible Light Ligand Cleavage Reaction of [Cr^{III}(salen)ClO$_3$] and [Cr^{III}(salen)BrO$_3$]

The reaction of [Cr^{III}(salen)Cl] (**3d**) with excess *ca.* 10 equiv. of AgClO$_3$ caused the quick substitution of the chloride counterion to afford the corresponding chlorate complex [Cr^{III}(salen)ClO$_3$] (**9d**) with precipitation of AgCl. The spectral signature of **9d** showed a blue-shifted band at 422 nm using UV-Vis spectroscopy, as shown in Figure 4-2A.
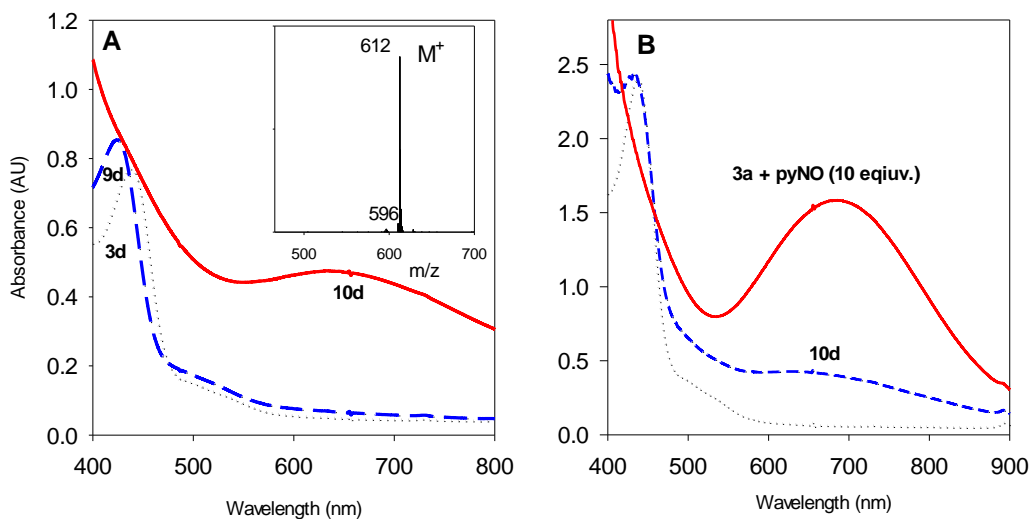
Figure 4-1. (A) UV–visible spectrum: [Cr^{III}(salen)Cl] (**3d**, dotted) and [Cr^{III}(salen)(ClO$_3$)] (**9d**, dash), and [Cr^V(salen)(O)](ClO$_3$) (**10d**, solid) formed upon visible light photolysis of

9d in CH₃CN; Inset showing ESI-MS spectrum of photo-generated **10d** in a positive mode. (B) UV–visible spectrum: **3d** (dashed), **10d** formed by oxidation of **3d** with PhI(OAc)₂ (2.5 equiv.) in CH₃CN, and the adduct of **10d** (solid) in the presence of pyridine N-oxide (10 equiv.).

The metastable **9d** was directly used for the photochemical reaction because of its highly photolabile nature. The formation of a new species with a notable color change was observed upon photolysis of [Cr^{III}(salen)ClO₃] (**9d**) in anaerobic CH₃CN media using visible light produced from a SOLA engine with an intensity of 60W. The light yellow **9d** species decayed over 12 min and a dark-green intermediate **10d** was generated. The UV-Vis spectrum, as shown in Figure 4-2A, showcased a sweeping band ranging from 550 to 800 nm which is characteristic for chromium(V)-oxo salen complexes as previously observed by Kochi et al..[81] The metastable [Cr^{V}(salen)(O)]$^+$ intermediate (**10d**) was then additionally characterized using ESI-MS in a positive mode, as demonstrated in the inset of Figure 4-2A. The spectrum showed a prevalent peak at an *m/z* of 612, which is characteristic of [Cr^{V}(salen)(O)]$^+$ composition. Based on the ESI-MS and the aforementioned UV-Vis absorption spectra, the species was designated as [Cr^{V}(salen)(O)](ClO₃). In a subsequent chemical oxidation experiment, the identical fleeting intermediate **10d** was produced by reacting 2.5 equiv. of PhI(OAC)₂ with [Cr^{III}(salen)Cl] (Figure 4-2B). Formation of [Cr^{V}(salen)(O)](pyNO) was achieved in the presence of 10 equiv. of pyridine *N*-oxide (pyNO) as a strong sigma-donor ligand, and the UV-Vis spectrum of the salen-chromium(V)-oxo adduct showed a well-defined band expanding past 800 nm in the visible absorption range; consistent with the previous report

by Kochi and colleagues.[81] In addition, the extensive tail band of the photo-generated **10d** was not modified upon the addition of PyNO as the donor ligand.

In the absence of light, $[Cr^V(salen)(O)]^+$ (**10d**) was not generated in a control experiment. Increasing the intensity of the visible light to 120W accelerated the conversion of $[Cr^{III}(salen)(ClO_3)]$ to **10d**, as anticipated. In coordinating solvents such as CH_3OH, there was no observed generation of **10d**; however, non-coordinating solvents such as $CHCl_3$ yielded similar outcomes. As previously mentioned in the porphyrin-manganese(V)-oxo chapter, it is analogously expected that disassociation would occur between the chlorate-chromium bond in the presence of coordinating solvent. There was no observable photo-decomposition of the chromium complexes under visible light irradiation as determined by UV-Vis spectroscopy.

As displayed in Figure 4-3A, salen-chromium(III) bromate precursors in the presence of visible light irradiation more efficiently generated **10d** intermediates at a significantly faster rate. The naphthalene salen ligand derivative (**3e**) (napthen =(*R,R*)-*N*, *N*'-bis-(2-hydroxy-1-naphthalidene)-1,2-cyclohexanediamine), as shown in Figure 4-3B, generated the transient **10e** upon visible light photolysis of the corresponding chlorate and bromate precursors. In a similar fashion, **10e** was also generated by combining **3e** with 2.5 equiv. of $PhI(OAc)_2$, presenting a UV-Vis spectrum with the featured wide band from 600 to 800 nm.
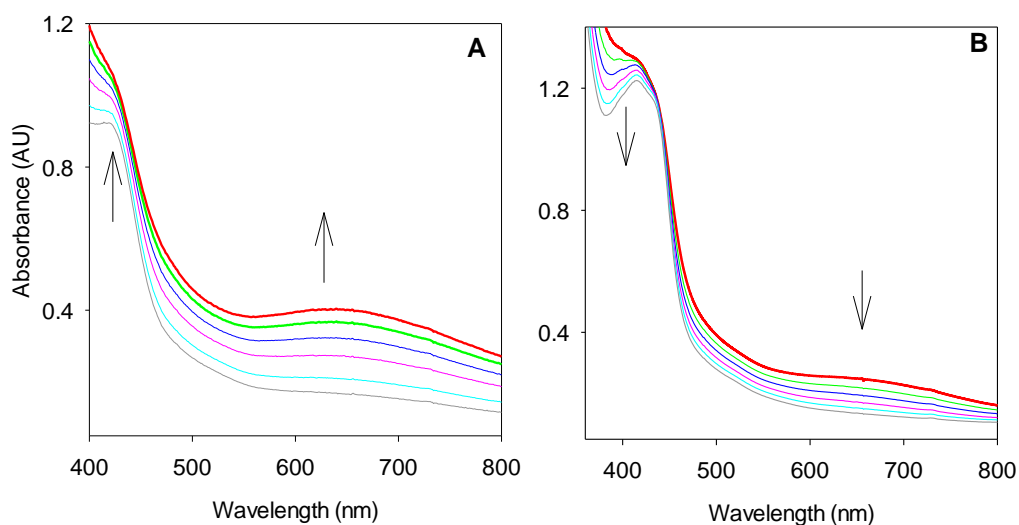
Figure 4-2. (A) Time-resolved formation spectra of **10d** (red line) following irradiation of $[Cr^{III}(salen)(BrO_3)]$ (1.0 mM) over 5 min with visible light in anaerobic CH_3CN at 23 °C; (B) Time-resolved spectra of the photo-generated **10e** decaying in the absence of a substrate in CH_3CN over 10 min.

We previously showed that porphyrin-iron(IV)oxo cationic radical intermediates, also termed Compound I models, can be generated *via* the photolysis of electron-rich porphyrin-iron(III) bromates proceeding through heterolytic cleavage of the O-Br bond.[49,77] In this investigation, two-electron photo-oxidation most likely occurs where the chromium(V)-oxo transient **10** is formed upon photolysis of the chlorate or bromate **9**. The photochemistry involves heterolysis of the O-X (X = Cl or Br) bonds in the axial ligand. Likewise, photolysis of the bromate precursor was more efficient than chlorate precursors creating the $[Cr^V(napthen)(O)]^+$ species under equivalent conditions.

4.2.2 Kinetic Studies of Sulfide Oxidation *via* [Cr^V(salen)(O)]$^+$ Species

Direct kinetic studies of oxidation of salen-chromium(V)-oxo intermediate **10d** towards organic reductants can be monitored by following the exponential decay of the broad peak at λ_{max} =680 nm. As shown in Figure 4-4A, the time-resolved spectra displayed a clear transition of **10d** to reform the initial **3d** at a λ_{max} = 420 nm.
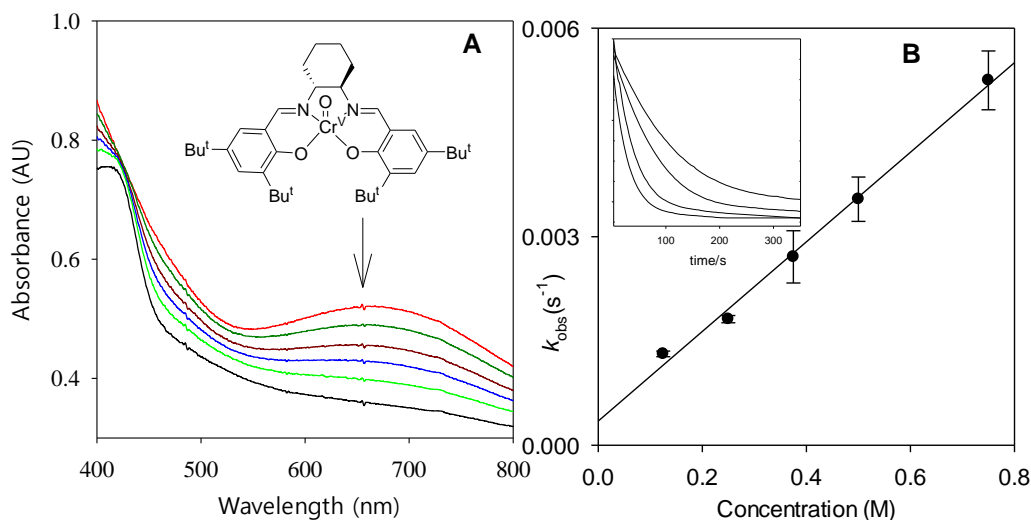
Figure 4-3. (**A**) Time-resolved spectra of the photo-generated **10d** reacting with cyclohexene (0.15 M) in CH$_3$CN over 10 min. (**B**) Kinetic plot of observed rate constants versus concentration of cyclohexene. Inset shows the kinetic traces at 680 nm for the reactions of **10d** with cyclohexene at different concentrations (0.15, 0.25, 0.5, and 0.75M from the top to bottom).

The absorbance in the Q band region at 680 nm was measured during the kinetic studies which decayed during the reaction (Inset in Figure 4-4B). The reactions were conducted under pseudo-first-order conditions and the kinetic traces were fitted to single exponential decay. The decay of the photo-formed species **10d** expedited in a linear manner

with the substrate concentration as in the case of cyclohexene (Figure 4-4B). The second-order rate constant (k_{ox}) was determined to be $(8.7 \pm 0.9) \times 10^{-3}\,M^{-1}\,s^{-1}$ for cyclohexene in the presence of the photo-generated intermediate. The **10d** species generated using chemical oxidation with PhI(OAc)$_2$ revealed a k_{ox} value similar to the photochemical method. Table 4-1. exhibits the k_{ox} values for the reaction of cyclohexene, diphenylmethane, and aryl sulfides with the chemical and photo-generated oxo species **10**.

Table 4-1. The second-order rate constants for chromium(V)-oxo salens **10**[a]

Entry	Substrate	k_{ox} ($M^{-1}s^{-1}$) x 10^{-3}	
		3a	**3b**
1	cyclohexene	8.7 ± 0.9	35.0 ± 1.5
	diphenylmethane	33.0 ± 3.0	70.0 ± 6.0
2	1-phenylethanol	32.0 ± 3.0	78.5 ± 10.0
3	Thioanisole	0.41 ± 0.02	58.5 ± 6.0
4	4-fluorothioanisole	1.1 ± 0.08	
5	4-chlorothioanisole	0.33 ± 0.02	
6	4-methylthioansiole	0.37 ± 0.04	
7	4-methoxythioanisole	0.37 ± 0.02	

[a] Generated either by photochemical or chemical methods in CH$_3$CN at 23 ± 2 °C. Reported values are the average of 2-3 runs with a deviation of 2σ

The reactivity of the two different salen-chromium(V)-oxo complexes towards the same substrates showed a distinct difference. The steric effects of the ligands most likely played a role in the increased reactivity of **10e** whereas the sterically encumbered **10d** complexes bearing bulky *tert*-butyl groups on the 3,5-position i.e. the "buttressing" effect

showed reduced reactivity. [Cr^{III}(napthen)Cl] is highly conjugated and has a planar naphthalene structure, unlike **10d,** although both structures have the analogous square-pyramidal geometry surrounding the chromium(V) ion. Unexpectedly, parrafins including cyclohexene and diphenylmethane (Ph$_2$CH$_2$) showed higher reactivity than thioanisoles. Conventional electrophilic metal-oxo intermediates show rate acceleration for sulfoxidation because of the increased nucleophilicity of thioanisoles. The second-order rate constants did not show a rate acceleration effect for the sulfide oxidation by salen-chromium(V)-oxo species, suggesting that a different mechanistic pathway is involved in contrast to porphyrin or corrole-metal-oxo intermediates. The modest k_{ox} values indicate that mechanism is unlikely to involve nucleophilic attack of the sulfide towards the chromium(V) center.[84] The results also suggest that the reactivity of the electrophilic salen-chromium(V)-oxo cation was inhibited by powerful coordination of the sulfoxide to the inner-sphere of the chromium center.

The *para*-aryl position of the sulfides showed a mild kinetic effect on the rate of oxidation at room temperature for **10d**, and the second-order rate constants for the reaction of *para*-substituted sulfide generally showed little variation with regards to reactivity. However, in the case of 4-fluorothioanisole, there was a significant rate acceleration in contrast to the other substituted sulfides. The significant rate acceleration of 4-fluorothioanisole indicates that the electron-withdrawing nature of the *para*-fluoro moiety of the sulfide draws electron density away from the benzylic sulfur and thus enhancing the overall nucleophilicity of the substrate. A Hammett analysis was conducted using the kinetic data obtained from the reaction of *para*-substituted thioanisoles with **10d**, but there was neither a linear relationship between the logk_{rel} values as a function of σ nor σ$^+$

substituent constants (Figure 4-5). The results indicate that there was no substantial charge development on the benzylic sulfur during the RDS of the OAT event. However, the non-linear Hammett plots could potentially indicate the development of radical character in the transition state of the RDS like in the case of iron(IV)-oxo and *trans*-dioruthenium(IV) porphyrin. [85,86]
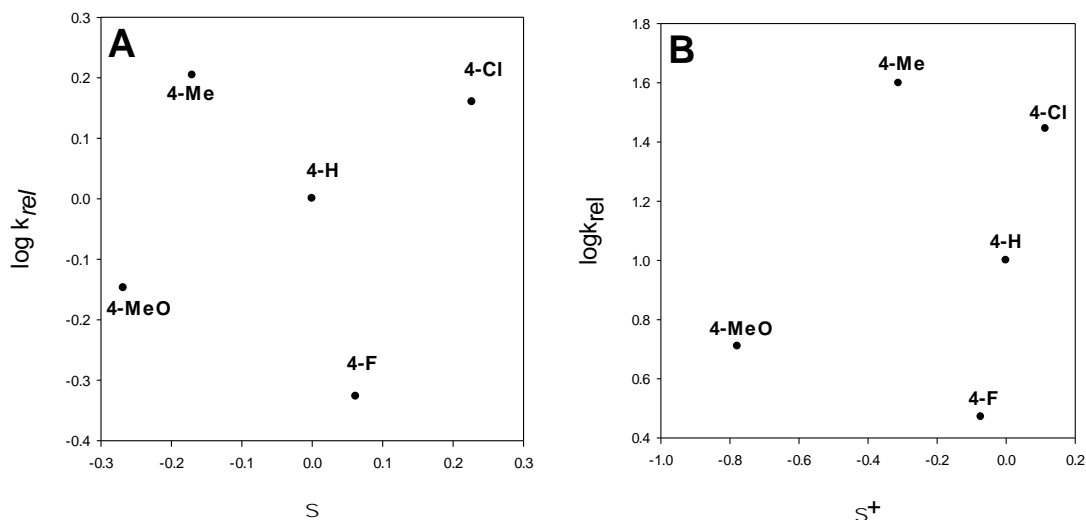
Figure 4-4. Hammett plots for the rate constants for reactions of $[Cr^{III}(salen)(O)]^+$ (**10d**) with Hammett σ (A) and σ^+ (B) constants.

4.2.3 Catalytic and Competition Studies of Sulfide Oxidations by $[Cr^V(salen)(O)]^+$

Transition metal-mediated methodologies for the enantio- and regioselective transformations of organic sulfide to chiral sulfoxidations are of importance in the synthesis of certain pharmaceutical compounds that require a pertinent oxidation pattern.[84] In this context, salen-chromium(III) complexes catalyzed the highly efficient and selective oxidation of thioanisoles. As shown in Table 4-2, aryl sulfides in methanolic solutions can be near-quantitatively converted to sulfoxides with good chemoselectivity over sulfone.

Table 4-2. Catalytic oxidation of thioanisoles by chromium(III) salens (**3**) and PhI(OAc)$_2$.[a]

Entry	Catalyst	Substrate	Time (min)	Conv.[b] (%)	Product	Selectivity%[b]
1	[Cr^{III}(salen)Cl]		30	100		91:09
2	[Cr^{III}(napthen)Cl]		10	100		85:15
3	[Cr^{III}(salen)Cl]		30	100		92:08
4			60	99		87:13
5			60	100		89:11
6			20	92		84:16
7			20	97		92:08
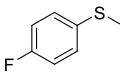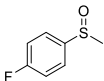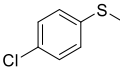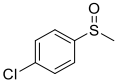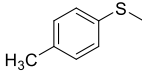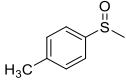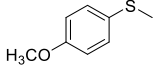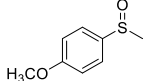
[a] All reactions were conducted in CH$_3$OH (2 mL) at ca. 23 °C with 1.5 equiv. PhI(OAc)$_2$ (0.75 mmol), sulfide substrate (0.5 mmol), 2.0 mol% catalyst loading in the presence of H$_2$O (5.0 µL); sulfoxide and small amounts of sulfone were detected by GC-MS analysis of the crude reaction mixture. [b] Based on the product ratios (sulfoxide: sulfone) determined by GC-MS analysis with an internal standard on the crude reaction mixture after the reaction; material balance > 95%. [c] Carried out in the presence of pyridine *N*-oxide.

However, **10e** showed greater catalytic activity with lower selectivity under equivalent reaction conditions. There was no noticeable effect with regards to selectivity when excess PyNO (10 equiv.) was added to the reaction, and in the control experiment, there were no oxidized products generated in the absence of catalyst with $PhI(OAc)_2$ and H_2O (< 1% GC). When other solvents were used including CH_2Cl_2. $CHCl_3$, and CH_3CN, there was a decrease in the reactivity with respect to MeOH. Under catalytic turnover conditions, there was no substantial degradation of the catalyst as indicated by UV-Vis spectroscopy. The superior reactivity for sulfoxidations suggests that chromium salens are robust catalysts that are resistant to mild oxidizers such as $PhI(OAc)_2$. Conversely, in the case of olefin substrates such as styrene and cyclohexene, poor reactivities (< 10% conversion) were observed over 12 h.

The introduction of electron releasing substituents on the *para*-position of the sulfide such as methoxy or methyl moieties showed increased catalytic reactivities; on the other hand, substituents that are electron-withdrawing in nature such as fluoro and chloro groups exhibited reduced reactivities. Competition studies on the sulfide reactions catalyzed by chromium(III) salen (**10d**) using $PhI(OAc)_2$ as an oxygen source were conducted to evaluate the nature of the principal oxidant in the catalytic cycle. Hammett analysis where the $logk_{rel}$ as a function of Hammett substituent constant gave an excellent linear fitting (R = 0.99) under competitive conditions (Figure 4-6). The slope of the Hammett plot was determined to be -2.72, suggesting the transition states at the benzylic sulfur of the RDS during the reaction entails the development of a positive charge.
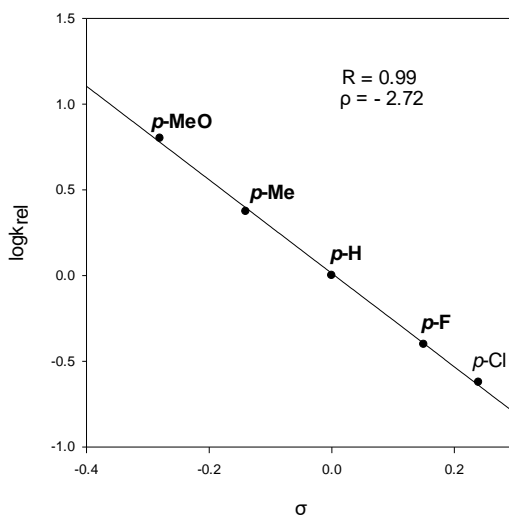
Figure 4-5. Hammett correlation studies (log k_{rel} vs σ) for the $[Cr^{III}(salen)(Cl)]$-catalyzed oxidation of substituted aryl sulfides by PhI(OAc)$_2$ in CH$_3$OH at 23 ± 2 $^{\circ}$C.

As previously mentioned, salen-chromium(V)-oxo species **10** were formed upon oxidation of chromium(III) salen complexes **3** using PhI(OAc)$_2$. In 2004, Gross and coworkers showed that the catalytic aerobic oxidation cycle for corrole-chromium complexes involved the regeneration of a chromium(V)-oxo intermediate *via* the reaction of corrole-chromium(III) with molecular oxygen.[87] The terminal oxidant under catalytic turnover conditions is most likely not the active species in the observed salen-chromium(V)-oxo intermediate **10** in the kinetic studies. The oxidation conversion ratios for the competitive oxidations of the two sulfide substrates under turnover conditions differ significantly from the ratios obtained from the absolute rate constants from the kinetic data (Table 4-3). The relative rate constants from the two different methods indicated that the principal oxidant under catalytic turnover conditions is not the detected chromium(V)-oxo intermediate **10** in the kinetic or spectroscopic investigations.

Table 4-3. Relative rate constants from kinetic studies and competition catalytic oxidations.[a]

Substrates	Method	k_{rel}[b]
p-F-PhSMe/PhSMe	Kinetic results	2.68
	PhI(OAc)$_2$	0.40
p-Cl-PhSMe/PhSMe	Kinetic results	0.80
	PhI(OAc)$_2$	0.23
p-Me-PhSMe/PhSMe	Kinetic results	0.90
	PhI(OAc)$_2$	2.36
p-MeO-PhSMe/PhSMe	Kinetic results	0.90
	PhI(OAc)$_2$	6.30

[a] A reaction solution containing an equivalent amount of two substrates e.g., thioanisole (0.2 mmol) and substituted thioanisole (0.2 mmol), chromium(III) salen catalyst (10 μmol) and an internal standard of 1,2,3-trichlorobenzene was prepared in CH$_3$OH (2 mL) Iodobenzene diacetate PhI(OAc)$_2$ (0.1 mmol) was added with 5.0 μL H$_2$O, and the mixture was stirred for ca. 10 to 15 min at 23 ± 2 °C.

[b] Relative ratios of absolute rate constants from kinetic results with chromium(V)-oxo salen complexes (**10e**) and for competitive oxidations with Chromium(III) salen catalysts (**3e**) at ambient temperature, All competition ratios are averages of 2-3 determinations with standard deviations smaller than 10% of the reported values.

A possible mechanism is that the salen-chromium(V) oxo species serves as a Lewis acid in the activation of PhI(OAc)$_2$ in which the oxygen atom in the coordinated PhIO transfers to the aryl sulfide. Absolute detection and characterization i.e., EPR and X-ray absorption near edge structure (XANES) spectroscopies of the transient oxidant would

provide amble mechanistic information on organic sulfide oxidation *via* salen-chromium(III) complexes and PhI(OAc)$_2$.

4.3 Conclusion

To conclude, a simple photochemical technique was developed using visible light photolysis of salen-chromium(III) chlorate and bromate complexes to produce high-valent chromium(V)-oxo intermediates which were then subsequently studied in real-time. Two-electron oxidation of the chromium ion was achieved *via* heterolytic cleavage of the O-X bond in the apical axial ligand to yield the active oxochromium(V) species. The visible light-generated [Cr^V(salen)O]$^+$ and [Cr^V(napthen)O]$^+$ intermediates were indistinguishable from the species generated from the reaction of salen-chromium(III) complexes with PhI(OAc)$_2$ in terms of their kinetic and spectroscopic behavior. The active oxidant in the catalytic cycle of chromium(III)-salen-catalyzed sulfide oxidations with PhI(OAc)$_2$ is unlikely to be the same oxidant in the kinetic studies based on the relative rate constants from kinetic and competition studies. As explained in the following chapter, other salen-metal-oxo intermediates i.e. manganese(V)-oxo salens can be generated and spectroscopically and kinetically investigated for alkane C-H activation and olefin epoxidation.

CHAPTER 5

PHOTOCHEMICAL GENERATION OF MANGANESE(V)-OXO SALEN COMPLEXES AND MECHANISTIC INSIGHTS OF CATALYTIC SULFOXIDATIONS

5.1   Introduction

Asymmetric metallosalens have garnered much attention in light of their extensive synthetic utility as oxidation catalysts for reactions that create fine chemicals with a high level of stereochemical enhancement.[27] Following their research on salen-chromium-catalyzed epoxidations, Kochi et al. designed salen-manganese(III) complexes that were able to achieve achiral epoxidation of olefins with iodosylbenzene (PhIO) as the oxygen source.[81] Kochi and colleagues proposed the active intermediate was a transient cationic manganese(V)-oxo species, although they only spectroscopically detected μ-oxomanganese(IV) dimer intermediates. In the 1990s, Jacobsen and Katsuki independently developed salen-manganese-catalyzed epoxidations of unactivated olefins and achieved high enantioselectivities.[36,88] The structural design of chiral the salen-manganese complexes was largely founded on the OAT mechanism of heme-containing enzymes with a tetradentate binding arrangement.[29] The mechanism of Jacobson-Katsuki epoxidation is still under debate, but the most probable active oxidant in the catalytic cycle is a salen-oxomanganese(V) cationic species upon oxidation of salen-manganese(III).[36] Three different mechanistic pathways hitherto been proposed for the oxidation reactions including a step-wise pathway, a concerted pathway, and an atypical metallaoxetane pathway.[28] Of the following mechanisms, the concerted oxygen insertion pathway is largely accepted. In the case of Jacobsen's catalyst, the olefin trajectory involves a "top-

on" approach where the olefin is forced to travel alongside the asymmetric cyclohexane diamine backbone of the catalyst due to the restricting nature of the bulky *tert*-butyl substituent on the 3, 5 position of the aryl moiety. The chiral backbone of the salen ligand enhances the stereochemical communication with the olefin transition state at the RDS. Upon arrival, the olefin undergoes nucleophilic attack on the oxo-ligand of the manganese(V) ion to generate the corresponding epoxide.

Although there have been great advances in catalytic transformations of heteroatom-heteroatom bonds using metallosalen complexes,[27] the usefulness of manganese-salen complexes specifically for the oxidation of organic sulfides is relatively limited. Jacobsen and colleagues reported the application of salen-manganese(III) with H_2O_2 as the terminal oxidant to achieve excellent yields of sulfoxide (84-95%) with moderate enantioselectivity (34-68% ee); likewise, Katsuki and coworkers developed salen-manganese(III) and PhIO catalytic systems that carried out the excellent conversion of aryl sulfide to sulfoxide (84-95%) with moderate to excellent enantioselectivity (30-80%).[89] Although there is promise for manganese-salen-catalyzed sulfide oxidation reactions, there is limited spectroscopic and kinetic evidence of the existence of a manganese(V)-salen oxo intermediate involved in this particular catalytic cycle. Herein, we show our ongoing progress on visible light production of cationic manganese(V)-oxo complexes bearing the well-known Jacobsen's ligand (**4d**) and a naphthalene derivative (**4e**) (Scheme 5-1).

Scheme 5-1. Chemical and photochemical generation of salen-manganese(V)-oxo complexes.

The second-order rate constants for the reactions of generated salen-manganese(V)-oxo species with various organic reductants bared resemblance to the salen-chromium(V)-oxos. The second-order rate constants for the OAT reaction for sulfides were on average one magnitude less than in the case of activated alkanes and alkenes. Preliminary competitive and kinetic studies provided some mechanistic insights into the reactivity and nature of the oxidant involved in catalytic sulfide oxidation reactions. The results suggest that the principal oxidant from the kinetic method is not identical to the intermediate produced from the competitive oxidation method.

5.2   Results and Discussion

5.2.1   Photolysis of [Mn^{III}(salen)(BrO₃)] and [Mn^{II}(napthen)(BrO₃)] and Chemical Generation of Salen-Manganese(V) Intermediates

As shown in Scheme 5-1, rapid axial ligand exchange to the corresponding bromate [Mn^{III}(salen)(BrO$_3$)] (**11d**) or chlorate [Mn^{II}(napthen)(ClO$_3$)] (**11e**) precursor using excess AgBrO$_3$ or AgClO$_3$, respectively. The generation of **11d** was further characterized by UV-Vis which displayed a spectrum in which the initial shoulder peaks of **4d** at 421 and 495 nm vanished; however, in the case of **11e**, the UV-Vis spectrum showed a slightly blue-shifted band at 435 nm. Species **11d** and **11e** were photolabile species thus the precursors were promptly used for the photochemical reaction without isolation. Visible light photolysis using a SOLA light engine (output power 60 W) of the photolabile complexes in anaerobic CH$_3$CN triggered the production of a *dark-brown* species **12** which displayed a broad band sweeping from 420 nm to 800 nm.
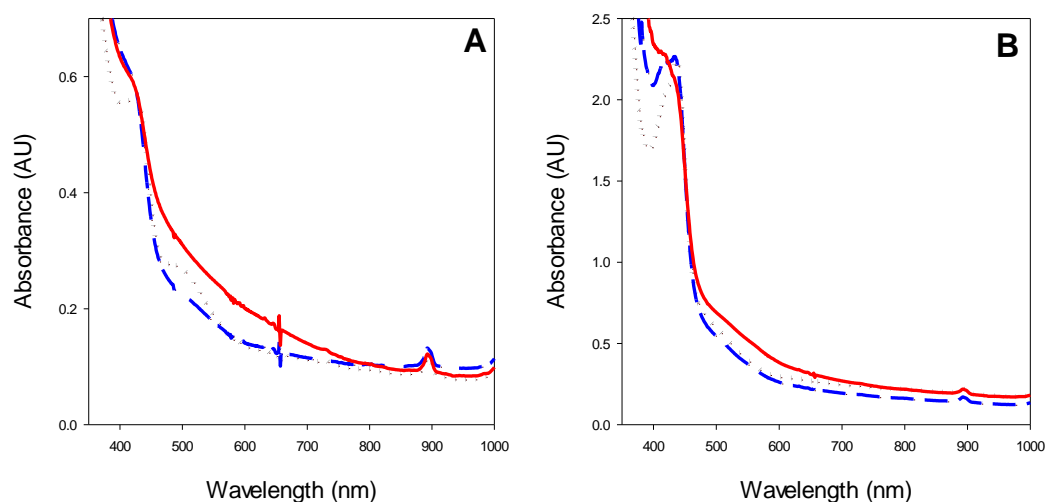
Figure 5-1. (A) UV–visible spectrum: [Mn^{III}(salen)Cl] (**4d**, dotted) and [Mn^{III}(salen)(BrO$_3$)] (**11d**, dashed), and [Mn^{III}(salen)(O)](BrO$_3$) (**12d**) formed upon visible light photolysis of **11d** in CH$_3$CN. (B) UV–visible spectrum: [Mn^{III}(napthen)Cl] (**4e**, dotted) and [Mn^{II}(napthen)(ClO$_3$)] (**11e**, dash), and [Mn^{V}(salen)(O)](BrO$_3$) (**12e**, solid) formed upon visible light photolysis of **11d** in CH$_3$CN.

As presented in Figure 5-2, the time-resolved absorption spectra show the formation of species **11d** upon 11 min of visible light irradiation. On the other hand, generation of **11e** occurred over the span of 6 min in the presence of visible light. The baseline drift in the time-resolved spectra can be attributed to the emergence AgCl precipitate upon axial ligand exchange of the precursors. The control experiments showed that species **12** was not generated in the absence of light. In contrast to our previous studies, visible light irradiation of [Mn^{III}(napthen)(ClO$_3$)] generating species **12d** was a more efficient photochemical process in comparison to that of [Mn^{III}(napthen)(BrO$_3$)] which contained more photolabile BrO$_3$ ligand. There was no observable photo-degradation of the complexes under visible light irradiation under all circumstances. The addition of 10

79

equiv. of donor ligands such as pyNO or imidazole (Imid) in this investigation showed no improvement in the tail band of the photogenerated intermediates **12d** and **12e**.
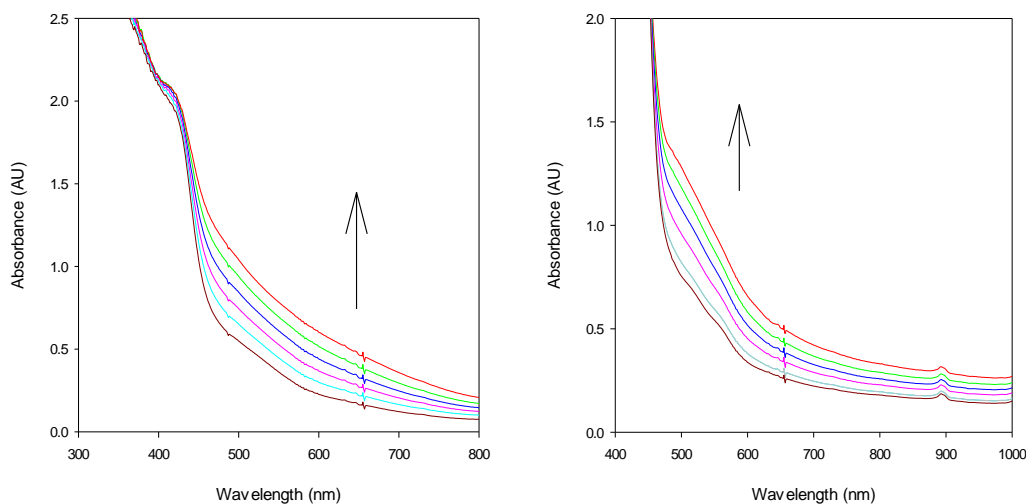
Figure 5-2. (A) Time-resolved formation spectra of **12d** (red line) following irradiation of $[Mn^{III}(salen)(BrO_3)]$ (4.4 x 10^{-4}M) over 11 min with visible light in anaerobic CH_3CN at 23 °C; (B) Time-resolved spectra of the **12e** following irradiation of $[Mn^{III}(napthen)(ClO_3)]$ (4.4 x 10^{-4} M) over 6 min.

The spectral signature of the intermediate was further verified using chemical oxidation of **4** using stoichiometric amounts of mCPBA (Figure 5-3). The time-resolved spectra of the chemical generation of **12d** display a Soret band at 421 nm and a broad band at 630 nm and the time-resolved spectra of **12e** showed a wide band from 470 nm into the visible region. Although not observed in the absorption spectra of **12d**, there is a moderately resolved isosbestic in the case of **12e** suggesting there is no accumulation of other intermediates during the reaction. In general, the time-resolved spectra of chemical generation of the high-valent oxo species were similar to the photochemical method. The

chemically-generated intermediate **12d** was metastable and was then further characterized

using ESI-MS (positive mode) (Figure 5-3 inset). The spectrum revealed a noticeable peak

at a mass-to-charge ratio (*m/z*) of 617 which corresponds to the molecular composition of

$[Mn^V(salen)(O)]^+$. Similar to the photochemical method, the presence of 10 equiv. of donor

ligands such as pyNO or Imid to the chemically-generated intermediates showed no

improvement in the wideband spanning into the visible absorption spectrum. Similar to

salen-oxochromium(V) species, the photochemistry involved in this reaction can be

ascribed to the heterolysis of the O-X bonds in the apical counter ion to give rise to the

salen-oxomanganese(V) intermediate in the presence of visible light, and the manganese

ion proceeds through a two-electron photo-oxidation process.
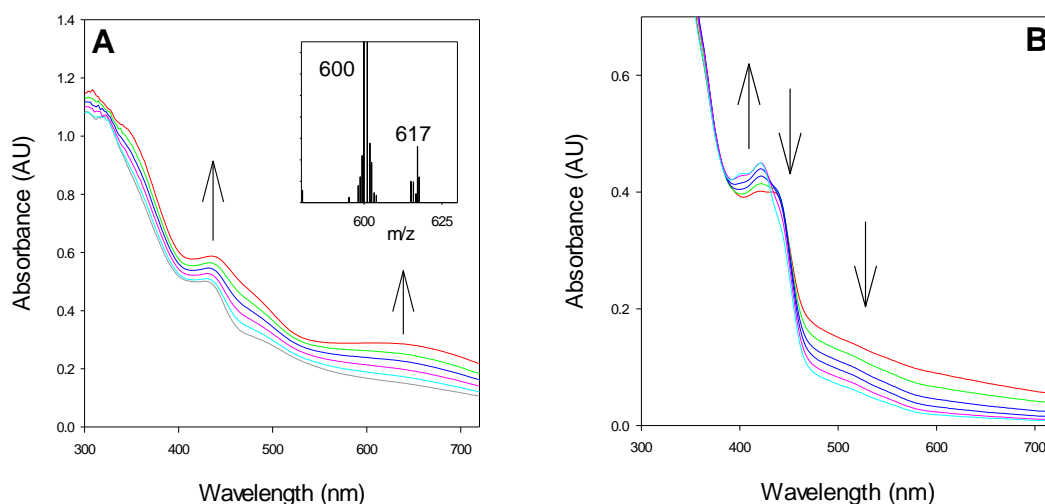
Figure 5-3. (A) Time-resolved spectra of **12d** (1×10^{-4}M) following oxidation of **4d** with

mCPBA (1 equiv.) over 10s in CH_3CN at 23 °C; Inset showing the ESI-MS of **12d** in a

positive mode. (B) Time-resolved spectra of the decomposition of **12e** (1×10^{-4}M)

following oxidation of **4e** in over 17 min in CH_3CN at 23 °C.

5.2.2 Kinetic Studies of Aryl Sulfides *via* [Mn^V(salen)(O)]$^+$ Intermediates

Upon generating the manganese (V)-oxo species **12**, the oxidation kinetics for several different organic substrates including thioanisole, alkenes, and benzylic hydrocarbons were investigated. The kinetics of the reactions were monitored using a stopped-flow kinetic unit. The salen-manganese complexes **3** were combined with stoichiometric amounts of mCPBA in CH$_3$CN media, and, after a 1-5 s delay, the solution consisting of [Mn^V(salen)(O)]$^+$ was introduced to a solution containing excess concentrations of reductant in the cuvette cell. The characteristic Q band with a λ_{max} at 630 nm underwent exponential decay over the course of the reaction under pseudo-first-order conditions. The representative kinetic plot of the reaction of **12d** as shown in Figure 5-4, shows a linear relationship between k_{obs} versus the concentration of cyclohexene. The slope of the kinetic plot provided a second-order rate constant of $(12.0 \pm 1.0) \times 10^{-3}\,M^{-1}\,s^{-1}$ which had the same magnitude of the k$_{ox}$ for the photo-generated **12d**.
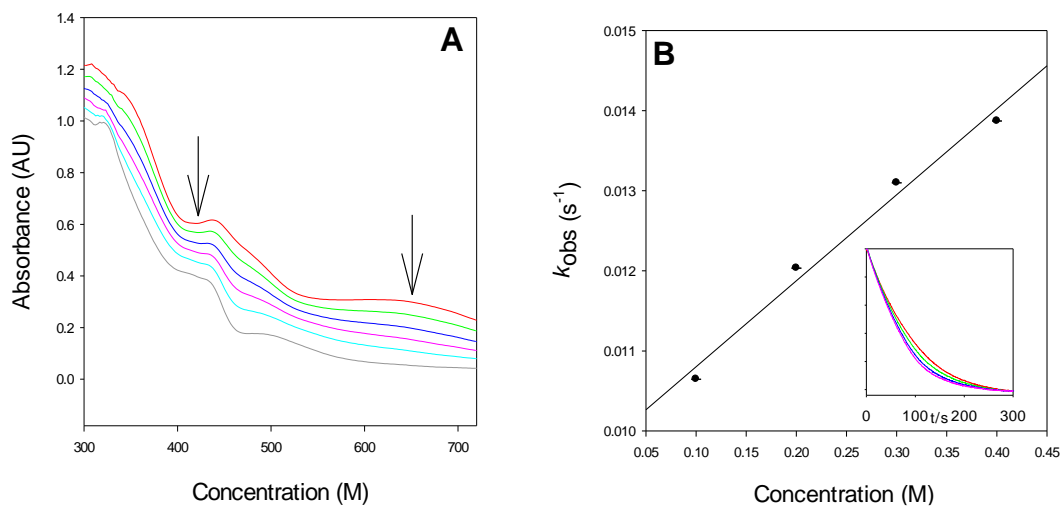
Figure 5-4(A) Time-resolved spectra of $[Mn^{III}(salen)(O)]^+$ (**12d**) reacting in CH₃CN solution with cyclohexene (0.3M) over 6 min at 23 ± 2 °C (B) Kinetic plot of the observed rate constants for the reaction of $[Mn^{III}(salen)(O)]^+$ (**12d**) versus the concentrations of cyclohexene. Inset showing traces at 650 nm for decaying of $[Mn^{III}(salen)(O)]^+$ (**12d**) with cyclohexene at various concentrations (0.1, 0.2, 0.3, and 0.4M from the top to bottom).

The second-order rate constants for the other organic reductants using the generated salen- manganese oxo intermediate are recorded in Table 5-1.

Table 5-1. The second-order rate constants for manganese(V)-oxo salens **12**[a]

Entry	Substrate	k_{ox} (M^{-1}s^{-1}) x 10^{-3}	
		4a	**3b**
1	cyclohexene	12.0 ± 1.0	4.30 ± 0.04
	diphenylmethane	47.0 ± 5.0	18.2 ± 2.1
	ethylbenzene	10 ± 1.0	
2	1-phenylethanol	58.0 ± 6.0	78.5 ± 10.0
3	triphenylphosphine	2,700 ± 100	1600 ± 100
4	thioanisole	2.7 ± 0.09	33.0 ± 1.0
5	4-nitrothioanisole	1.6 ± 0.09	7.3 ± 1.0
6	4-fluorothioanisole	3,000 ± 200	13,000 ± 1,000
7	4-chlorothioanisole	2.0 ± 0.08	17.5 ± 1.0
8	4-methylthioansiole	3.6 ± 0.4	3.2 ± 0.3

[a] Generated either by photochemical or chemical methods in CH$_3$CN at 23±2 °C. Reported values are the average of 2-3 runs with a deviation of 2σ

The second-order rate constants for the reaction of *para*-substituted aryl sulfide showed little variance; however, 4-fluorothioanisole showed significantly higher reactivity towards oxidation compared to other sulfide substrates. As shown in Figure 5-5, the reaction of 4-flurothioanisole with photo-generated [Mn^{III}(salen)(O)]$^+$ (**12d**) was determined to have a second-order rate constant of $(576 \pm 3) \times 10^{-3}$ M^{-1}s^{-1}. The k_{ox} values determined in this investigation did not show rate acceleration of sulfide oxidation by salen-manganese(V)-oxo intermediates. Similar to our previously reported salen-oxochromium(V) complexes, the small-second order rate constants were unanticipated

because of the enhanced nucleophilicity of sulfides and indicates that sulfide oxidation proceeds through a nonconventional mechanistic pathway. Once again, it is improbable for the sulfide to undergo nucleophilic attack upon coordination with the manganese(V)-ox cation. More likely, the electrophilicity of the active salen-manganese is hampered upon the inner-sphere coordination of the sulfoxide. The second-order rate constant of 4-fluorothioanisole can once again be explained because the electron density is being drawn towards the *para*-fluoro group thus improving the nucleophilicity of the benzylic sulfur.
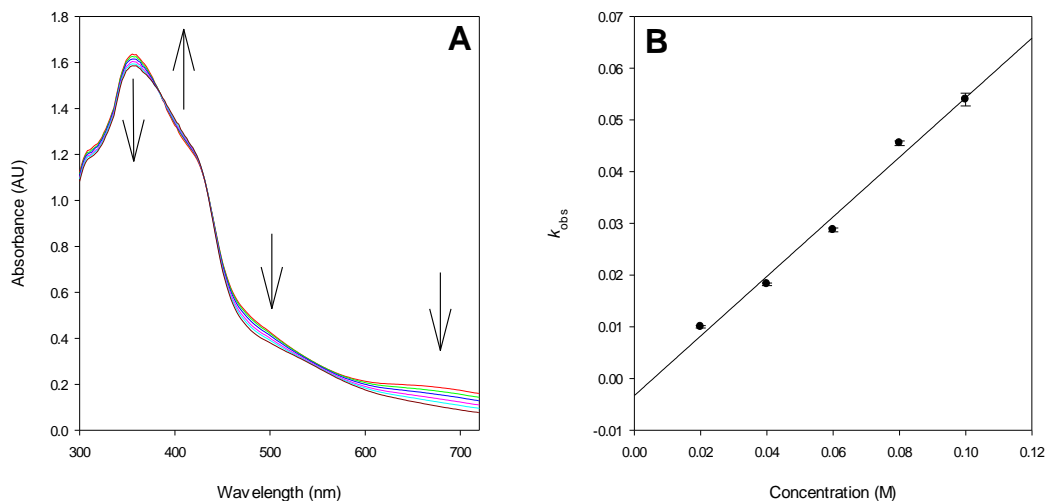
Figure 5- 5. (A) Time-resolved spectra of photo-generated $[Mn^{III}(salen)(O)]^+$ (**12e**) reacting in CH_3CN solution with 4-fluorothioanisole (0.1M) over 3 min at 23 ± 2 °C (B) Kinetic plot of the observed rate constants for the reaction of $[Mn^{III}(salen)(O)]^+$ (**12e**) versus the concentrations of 4-fluorothioanisole.

Hammett analyses were conducted using the kinetic data from the reaction of *para*-substituted aryl sulfides with **12d**. The plots of the logk_{rel} values as a function of Hammett σ or σ^+ constants showed a non-linear correlation suggesting no significant substitution

kinetic effect, as displayed in Figure 5-6. Likewise, the Hammet plots of [Mn^{III}(napthen)Cl] did not show any linear relationship. As mentioned in the previous chapter, non-linear Hammett analyses have been associated with transition states that have substantial radical character development during the RDS.
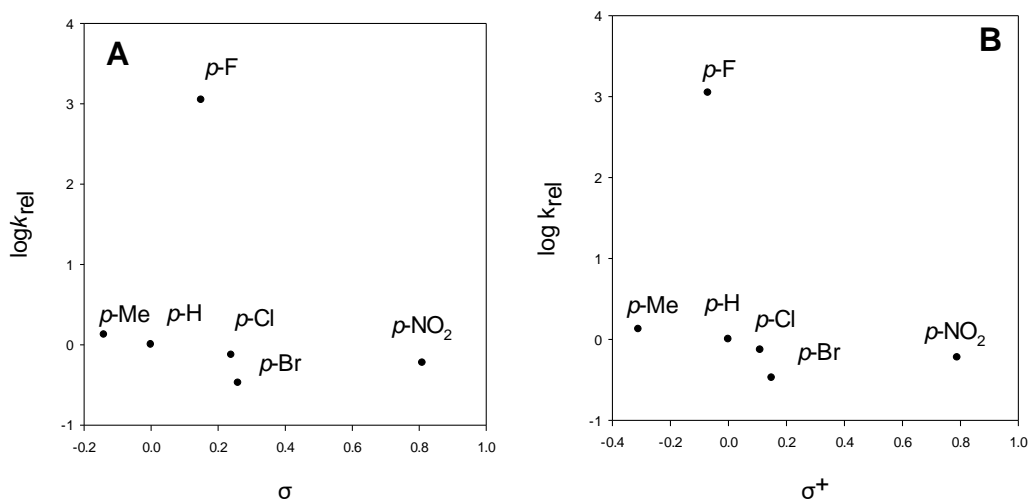
Figure 5-6. Hammett plots for the rate constants for reactions of [Mn^{III}(salen)(O)]$^+$ (**12d**) with Hammett σ (A) and σ$^+$ (B) constants.

5.2.3 Competitive Studies of Sulfide Oxidations using [Mn^{III}(napthen)Cl]

Although the catalytic activity of **4e** and **4d** towards aryl sulfides is still under investigation in our laboratory, we instead show a promising substituent kinetic effect in the aryl ring of sulfides using [Mn^{III}(napthen)Cl] **4e**. Competition studies were carried out for the sulfide oxidation catalyzed by manganese(III) salen (**4e**) with PhI(OAc)$_2$ as the terminal oxidant in order to ascertain the nature of the active species. The presence of electron-donating substituents resulted in increased reactivities compared to unsubstituted aryl sulfide; on the other hand, electron-withdrawing groups showed decreased reactivates.

The logk_{rel} versus Hammett substituent constants provided a superb linear fitting as shown in Figure 5-7. The reaction constant of the plot was determined to be $-(1.98) \pm 0.1$ indicating the possible development of a positive charge on the sulfur at the transition state of the rate-limiting steps. Of note, the use of σ^+ did not improve the fitting of the Hammett analysis.
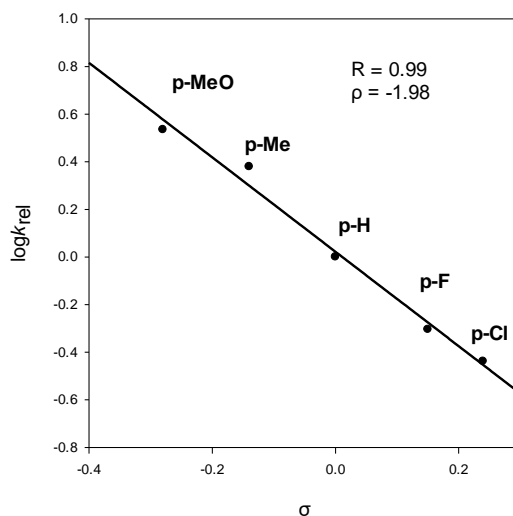
Figure 5-7. Hammett plots for relative rate constants for reactions of $[Mn^{III}(napthen)Cl]$ catalyzed sulfide oxidation of substituted aryl sulfide by $PhI(OAc)_2$ in CH_3CN 23 ± 2 ° C.

Table 5-2. Relative rate constants from kinetic studies and competition catalytic oxidations.[a]

Substrates	Method	k_{rel}[b]
p-F-PhSMe/PhSMe	Kinetic results	515
	PhI(OAc)$_2$	0.50
p-Cl-PhSMe/PhSMe	Kinetic results	0.53
	PhI(OAc)$_2$	0.36
p-Me-PhSMe/PhSMe	Kinetic results	0.10
	PhI(OAc)$_2$	2.40

[a] A reaction solution containing an equivalent amount of two substrates e.g., thioanisole (0.2 mmol) and substituted thioanisole (0.2 mmol), manganese(III) salen catalyst (10 μmol), and an internal standard of 1,2,3-trichlorobenzene was prepared in CH$_3$OH (2 mL) Iodobenzene diacetate PhI(OAc)$_2$ (0.1 mmol) was added with 5.0 μL H$_2$O, and the mixture was stirred for ca. 10 to 15 min at $23 \pm 2\,^{\circ}C$.

[b] Relative ratios of absolute rate constants from kinetic results with manganese(V)-oxo salen complexes (**12e**) using mCPBA and for competitive oxidations with manganese(III) salen catalysts (**4e**) at ambient temperature, All competition ratios are averages of 2-3 determinations with standard deviations smaller than 10% of the reported values.

As specified in Table 5-2, the ratios of direct rate constants determined in the kinetic studies were significantly different from the conversion ratios for competitive oxidations of the two substrates as dictated by catalytic turnover conditions. The most likely rationale for the observed reactivity is that the spectroscopically detected manganese(V)-oxo intermediate **12** is not the oxidant in the catalytic cycle. Bryliakov and colleagues conducted EPR studies that indicated the reaction of stoichiometric amounts of mCPBA with **4d** generated an unstable manganese(III)-acycloperoxo intermediate which rapidly transforms into predominately mononuclear salen-oxomanganese(IV) species at low temperatures.[90] A manganese(IV)-salen oxo species could account for the decreased reactivity for the oxidation of sulfides during the kinetic investigations. In the competition studies, the reaction of salen-manganese(III) complexes with $PhI(OAc)_2$ possibly produces a higher-valent species such as salen-oxomanganese(V) which oxidized aryl sulfide through a different pathway. As previously suggested, a distinct mechanistic pathway of catalytic sulfide oxidation by manganese salen complexes with either $PhI(OAc)_2$ or mCPBA will need conclusive characterization of the active oxidant through powerful spectroscopic techniques such as EPR.

5.4 Conclusion

In this investigation, a facile photochemical method was used to generate and study salen-manganese(V)-oxo intermediates upon visible light photolysis of manganese(III) chlorate or bromate precursors. The photochemistry involved the heterolysis of the O-X bond in the axial ligand resulting in two-electron oxidation of the manganese ion to generate reactive salen-manganese(V)-oxo transients. Preliminary investigations suggest that both the chemically and photo-chemically generated species were spectroscopically

and kinetically equivalent. Although the tentative kinetic studies utilized mCPBA as the oxygen source, the kinetically-detected manganese(V)-oxo species is not likely to act as the active oxidant in the competition studies using [Mn^{III}(napthen)Cl] catalyst with PhI(OAc)$_2$.

CHAPTER 6

CONCLUSIONS AND FUTURE WORKS

In conclusion, manganese(III) porphyrins, chromium(III) and manganese(III) salens were synthesized and characterized. Novel photochemical methods were cultivated to produce high-valent manganese-oxo and chromium-oxo complexes by the photolysis of corresponding photo-liable bromate and chlorate precursors. The results of these studies are pioneering, attesting to the fact that photochemical generation of reactive metal-oxo species is not restricted to porphyrin or corrole complexes, but can also be applied to facilely synthesized salen complexes. In all three different systems discussed in this thesis, the photochemistry was rationalized by either homolysis or heterolysis of the pertinent O-X bond of the haloate axial ligand that induced single or two-electron oxidation of the metal ion to afford high-valent oxomanganese and oxochromium species as potent OAT reagents.

The three different models also showed to be efficient catalytic systems for the near-quantitative conversion of aryl sulfides and several activated hydrocarbons with excellent regioselectivity using either $PhI(OAc)_2$ as an oxygen source in the presence of small amounts of H_2O. In all cases, the results of the competition studies and Hammett analyses for catalyzed oxidations indicated that the directly observed high-valent manganese and chromium-oxo intermediates found in the kinetic studies are not likely to act as the predominant oxidant under catalytic turnover conditions. Higher valent metal-oxo intermediates could potentially serve as the premier oxidants responsible for catalytic transformations even though said species were not spectroscopically detectable. In the case of manganese(III)-porphyrin-catalyzed oxidations, the mechanistic pathway involves a direct OAT event for reactive sulfides and/or a disproportionation reaction in the presence

of activated hydrocarbons. However, in the case of chromium(III) and manganese(III) salen-catalyzed reactions, the mechanistic pathways remain elusive and will require considerable spectroscopic detection and characterization of active oxidants to elucidate the premier intermediate.

The purpose of this research is to develop environmentally sustainable methods for mechanistic studies of high-valent manganese and chromium-oxo porphyrin and salen intermediates. The use of visible-light for photochemical generation of reactive metal-oxo species showed promise for the design and understanding of catalytic systems without the use of environmentally unfriendly terminal oxidants. Furthermore, we have demonstrated that highly selective and efficient oxidations of aryl sulfides and activated hydrocarbons can be achieved through the use of mild sacrificial oxidants and unsophisticated catalytic systems. Further exploration of substrate scope, optimization of reaction conditions with more environmentally benign oxygen sources, and extension of the promising photochemical approaches to produce and study new high-valent transition metal-oxo species supported by phthalocyanines are presently ongoing in our laboratory.

In addition, we recently reported the synthesis of a light-harvesting porphyrin-ruthenium(II) with 4,4-difluoro-4-bora-3a,4a-diaza-s-indacene (BODIPY) substituents that showed promise for catalytic oxidations under visible light.[91] As a proof of concept, we are developing light-harvesting metallosalen complexes that operate under a photo-induced energy-transfer (ET) mechanism which could potentially be useful for visible-light promoted catalytic oxidations as shown in Figure 6-1.
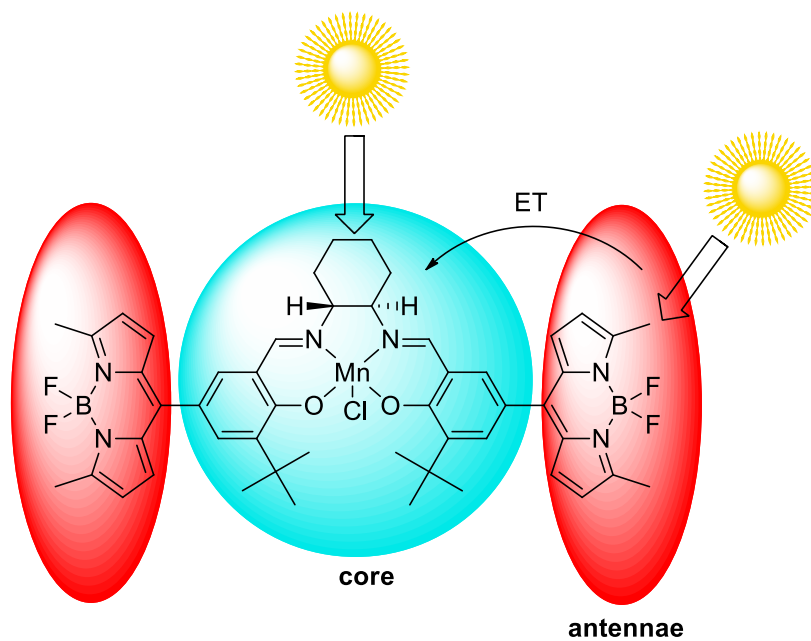
Figure 6-1. Potential structure of salen-BODIPY complex [Mn^{III}(L-salen)Cl] and visible-light induced energy transfer (ET) process.

REFERENCES

(1)   Denisov, I. G.; Makris, T. M.; Sligar, S. G.; Schlichting, I. Structure and Chemistry of Cytochrome P450. *Chem. Rev.* **2005**, *105* (6), 2253–2278.

(2)   Axelrod, J. The Enzymatic Deamination of Amphetamine (Benzedrine). *J. Biol. Chem.* **1955**, *214* (2), 753–763.

(3)   Omura, T.; Sato, R. A New Cytochrome in Liver Microsomes. *J. Biol. Chem.* **1962**, *237* (4), PC1375–PC1376.

(4)   Nelson, D. R.; Kamataki, T.; Waxman, D. J.; Guengerich, F. P.; Estabrook, R. W.; Feyereisen, R.; Gonzalez, F. J.; Coon, M. J.; Gunsalus, I. C.; Gotoh, O.; Okuda, K.; Nebert, D. W. The P450 Superfamily: Update on New Sequences, Gene Mapping, Accession Numbers, Early Trivial Names of Enzymes, and Nomenclature. *DNA Cell Biol.* **1993**, *12* (1), 1–51.

(5)   Lamb, D. C.; Lei, L.; Warrilow, A. G. S.; Lepesheva, G. I.; Mullins, J. G. L.; Waterman, M. R.; Kelly, S. L. The First Virally Encoded Cytochrome P450. *J. Virol.* **2009**, *83* (16), 8266–8269.

(6)   Nelson, D. R.; Zeldin, D. C.; Hoffman, S. M.; Maltais, L. J.; Wain, H. M.; Nebert, D. W. Comparison of Cytochrome P450 (CYP) Genes from the Mouse and Human Genomes, Including Nomenclature Recommendations for Genes, Pseudogenes and Alternative-Splice Variants. *Pharmacogenet* **2004**, *14* (1), 1–18.

(7)   Sono, M.; Roach, M. P.; Coulter, E. D.; Dawson, J. H. Heme-Containing Oxygenases. *Chem. Rev.* **1996**, *96* (7), 2841–2888.

(8)   Poulos, T. L.; Finzel, B. C.; Howard, A. J. High-Resolution Crystal Structure of Cytochrome P450cam. *J. Mol. Biol.* **1987**, *195* (3), 687–700.

(9)   Groves, J. T. The Bioinorganic Chemistry of Iron in Oxygenases and Supramolecular Assemblies. *PNAS* **2003**, *100* (7), 3569–3574.

(10)   Meunier, B.; de Visser, S. P.; Shaik, S. Mechanism of Oxidation Reactions Catalyzed by Cytochrome P450 Enzymes. *Chem. Rev.* **2004**, *104* (9), 3947–3980.

(11)   Gray, H. B.; Winkler, J. R. Living with Oxygen. *Acc. Chem. Res.* **2018**, *51* (8), 1850–1857.

(12)   Davydov, R.; Makris, T.; Kofman, V.; Werst, D.; Sligar, S.; Hoffman, B. Hydroxylation of Camphor by Reduced Oxy-Cytochrome P450cam: Mechanistic Implications of EPR and ENDOR Studies of Catalytic Intermediates in Native and Mutant Enzymes. *J. Am. Chem. Soc.* **2001**, 123, 1403-1415.

(13)   *Cytochrome P450: Structure, Mechanism, and Biochemistry*, 3rd ed.; Montellano, P. R. O. de, Ed.; Springer US, 2005.

(14)   *Modern Oxidation Methods*; Bäckvall, J.-E., Ed.; Wiley-VCH: Weinheim, 2004.

(15)   Meunier, B. Metalloporphyrins as Versatile Catalysts for Oxidation Reactions and Oxidative DNA Cleavage. *Chem. Rev.* **1992**, *92* (6), 1411–1456.

(16)   Che, C.-M.; Huang, J.-S. Metalloporphyrin-Based Oxidation Systems: From Biomimetic Reactions to Application in Organic Synthesis. *Chem. Commun.* **2009**, No. 27, 3996–4015.

(17)   Baglia, R. A.; Zaragoza, J. P. T.; Goldberg, D. P. Biomimetic Reactivity of Oxygen-Derived Manganese and Iron Porphyrinoid Complexes. *Chem Rev* **2017**, *117* (21), 13320–13352.

(18)   Sheldon, R. A. Recent Advances in Green Catalytic Oxidations of Alcohols in Aqueous Media. *Catal. Today.* **2015**, *247*, 4–13.

(19)   Dawson, J. H. Probing Structure-Function Relations in Heme-Containing Oxygenases and Peroxidases. *Science* **1988**, *240* (4851), 433–439.

(20)   Groves, J. T.; Nemo, T. E.; Myers, R. S. Hydroxylation and Epoxidation Catalyzed by Iron-Porphine Complexes. Oxygen Transfer from Iodosylbenzene. *J. Am. Chem. Soc.* **1979**, *101* (4), 1032–1033.

(21)   Groves, J. T.; Haushalter, R. C.; Nakamura, M.; Nemo, T. E.; Evans, B. J. High-Valent Iron-Porphyrin Complexes Related to Peroxidase and Cytochrome P-450. *J. Am. Chem. Soc.* **1981**, *103* (10), 2884–2886.

(22)   Penner-Hahn, J. E.; Smith Eble, Kim.; McMurry, T. J.; Renner, Mark.; Balch, A. L.; Groves, J. T.; Dawson, J. H.; Hodgson, K. O. Structural Characterization of Horseradish Peroxidase Using EXAFS Spectroscopy. Evidence for Fe = O Ligation in Compounds I and II. *J. Am. Chem. Soc.* **1986**, *108* (24), 7819–7825.

(23)   Penner-Hahn, J. E.; McMurry, T. J.; Renner, M.; Latos-Grazynsky, L.; Eble, K. S.; Davis, I. M.; Balch, A. L.; Groves, J. T.; Dawson, J. H.; Hodgson, K. O. X-Ray Absorption Spectroscopic Studies of High Valent Iron Porphyrins. Horseradish Peroxidase Compounds I and II and Synthetic Models. *J. Biol. Chem.* **1983**, *258* (21), 12761–12764.

(24)   Mandon, D.; Weiss, R.; Jayaraj, K.; Gold, A.; Terner, J.; Bill, E.; Trautwein, A. X. Models for Peroxidase Compound I: Generation and Spectroscopic Characterization of New Oxoferryl Porphyrin .Pi. Cation Radical Species. *Inorg. Chem.* **1992**, *31* (21), 4404–4409.

(25)   Gold, A.; Jayaraj, K.; Doppelt, P.; Weiss, R.; Chottard, G.; Bill, E.; Ding, X.; Trautwein, A. X. Oxoferryl Complexes of the Halogenated (Porphinato)Iron

Catalyst [Tetrakis(2,6-Dichlorophenyl)Porphinato]Iron. *J. Am. Chem. Soc.* **1988**, *110* (17), 5756–5761.

(26) Rose, E.; Andrioletti, B.; Zrig, S.; Quelquejeu-Ethève, M. Enantioselective Epoxidation of Olefins with Chiral Metalloporphyrin Catalysts. *Chem. Soc. Rev.* **2005**, *34* (7), 573–583.

(27) Shaw, S.; White, J. D. Asymmetric Catalysis Using Chiral Salen–Metal Complexes: Recent Advances. *Chem. Rev.* **2019**, *119* (16), 9381–9426.

(28) McGarrigle, E. M.; Gilheany, D. G. Chromium− and Manganese−salen Promoted Epoxidation of Alkenes. *Chem. Rev.* **2005**, *105* (5), 1563–1602.

(29) Yoon, T. P. Privileged Chiral Catalysts. *Science* **2003**, *299* (5613), 1691–1693.

(30) *Comprehensive Asymmetric Catalysis*; Jacobsen, E. N., Pfaltz, A., Yamamoto, H., Eds.; Springer-Verlag: Berlin Heidelberg, 1999.

(31) Blaser, H.-U.; Schmidt, E. *Asymmetric Catalysis on Industrial Scale Challenges, Approaches and Solutions*; 2007.

(32) Katsuki, T.; Sharpless, K. B. The First Practical Method for Asymmetric Epoxidation. *J. Am. Chem. Soc.* **1980**, *102* (18), 5974–5976.

(33) Sharpless, K. B. Searching for New Reactivity (Nobel Lecture). *Angew. Chem* **2002**, *41* (12), 2024–2032.

(34) Kolb, H. C.; VanNieuwenhze, M. S.; Sharpless, K. B. Catalytic Asymmetric Dihydroxylation. *Chem. Rev.* **1994**, *94* (8), 2483–2547.

(35) Rossiter, B. E.; Katsuki, T.; Sharpless, K. B. Asymmetric Epoxidation Provides Shortest Routes to Four Chiral Epoxy Alcohols Which Are Key Intermediates in

Syntheses of Methymycin, Erythromycin, Leukotriene C-1, and Disparlure. *J. Am. Chem. Soc.* **1981**, *103* (2), 464–465.

(36)   Zhang, W.; Loebach, J. L.; Wilson, S. R.; Jacobsen, E. N. Enantioselective Epoxidation of Unfunctionalized Olefins Catalyzed by Salen Manganese Complexes. *J. Am. Chem. Soc.* **1990**, *112* (7), 2801–2803.

(37)   Irie, R.; Noda, K.; Ito, Y.; Katsuki, T. Enantioselective Epoxidation of Unfunctionalized Olefins Using Chiral (Salen)Manganese(III) Complexes. *Tetrahedron Lett.* **1991**, *32* (8), 1055–1058.

(38)   Larrow, J. F.; Jacobsen, E. N. Asymmetric Processes Catalyzed by Chiral (Salen)Metal Complexes. In *Organometallics in Process Chemistry*; Brown, J. M., Fürstner, A., Hofmann, P., van Koten, G., Kündig, E. P., Reetz, M., Dixneuf, P. H., Hegedus, L. S., Knochel, P., Murai, S., Abe, A., Series Eds.; Topics in Organometallic Chemistry; Springer Berlin Heidelberg: Berlin, Heidelberg, 2004; Vol. 6, pp 123–152.

(39)   Katsuki, T. Some Recent Advances in Metallosalen Chemistry. *Synlett* **2003**, *2003* (3), 281–297.

(40)   Andrey, K. S. Recent Advances in Chiral Catalysis Using Metal Salen Complexes. *Curr. Org. Chem.* **2012**, *16* (15), 1788–1807.

(41)   Yoon, T. P.; Ischay, M. A.; Du, J. Visible Light Photocatalysis as a Greener Approach to Photochemical Synthesis. *Nat. Chem.* **2010**, *2* (7), 527–532.

(42)   Zhang, R.; Klaine, S.; Alcantar, C.; Bratcher, F. Visible Light Generation of High-Valent Metal-Oxo Intermediates and Mechanistic Insights into Catalytic Oxidations. *J. Inorg. Biochem.* **2020**, *212*, 111246.

(43)   Zhang, R.; Newcomb, M. Laser Flash Photolysis Generation of High-Valent Transition Metal−Oxo Species: Insights from Kinetic Studies in Real Time. *Acc. Chem. Res.* **2008**, *41* (3), 468–477.

(44)   Newcomb, M.; Zhang, R.; Chandrasena, R. E. P.; Halgrimson, J. A.; Horner, J. H.; Makris, T. M.; Sligar, S. G. Cytochrome P450 Compound I. *J. Am. Chem. Soc.* **2006**, *128* (14), 4580–4581.

(45)   Pan, Z.; Wang, Q.; Sheng, X.; Horner, J. H.; Newcomb, M. Highly Reactive Porphyrin−Iron−Oxo Derivatives Produced by Photolyses of Metastable Porphyrin−Iron(IV) Diperchlorates. *J. Am. Chem. Soc.* **2009**, *131* (7), 2621–2628.

(46)   Zhang, R.; Newcomb, M. Laser Flash Photolysis Formation and Direct Kinetic Studies of Manganese(V)-Oxo Porphyrin Intermediates. *J. Am. Chem. Soc.* **2003**, *125* (41), 12418–12419.

(47)   Harischandra, D. N.; Zhang, R.; Newcomb, M. Photochemical Generation of a Highly Reactive Iron−Oxo Intermediate. A True Iron(V)−Oxo Species? *J. Am. Chem. Soc.* **2005**, *127* (40), 13776–13777.

(48)   Pan, Z.; Zhang, R.; Fung, L. W.-M.; Newcomb, M. Photochemical Production of a Highly Reactive Porphyrin−Iron−Oxo Species. *Inorg. Chem.* **2007**, *46* (5), 1517–

(49)   Chen, T.-H.; Asiri, N.; Kwong, K. W.; Malone, J.; Zhang, R. Ligand Control in the Photochemical Generation of High-Valent Porphyrin-Iron–Oxo Derivatives. *Chem. Commun.* **2015**, *51* (49), 9949–9952.

(50)   Kwong, K. W.; Patel, D.; Malone, J.; Lee, N. F.; Kash, B.; Zhang, R. An Investigation of Ligand Effects on the Visible Light-Induced Formation of Porphyrin–Iron(IV)-Oxo Intermediates. *New J. Chem.* **2017**, *41* (23), 14334–14341.

(51) Zhang, R.; Horner, J. H.; Newcomb, M. Laser Flash Photolysis Generation and Kinetic Studies of Porphyrin−Manganese−Oxo Intermediates. Rate Constants for Oxidations Effected by Porphyrin−Mn^{V}−Oxo Species and Apparent Disproportionation Equilibrium Constants for Porphyrin−Mn^{IV}−Oxo Species. *J. Am. Chem. Soc.* **2005**, *127* (18), 6573–6582.

(52) Collman, J. P.; Wagenknecht, P. S.; Hutchison, J. E. Cofaciale Bis(metallo)diporphyrine als potentielle molekulare Katalysatoren für Mehrelektronenreduktionen und -oxidationen kleiner Moleküle. *Angew. Chem.* **1994**, *106* (15–16), 1620–1639.

(53) Sorokin, A. B. Recent Progress on Exploring M-Oxo Bridged Binuclear Porphyrinoid Complexes in Catalysis and Material Science. *Coord. Chem. Rev.* **2019**, *389*, 141–160.

(54) Wasser, I. M.; Fry, H. C.; Hoertz, P. G.; Meyer, G. J.; Karlin, K. D. Photochemical Organic Oxidations and Dechlorinations with a μ-Oxo Bridged Heme/Non-Heme Diiron Complex. *Inorg. Chem.* **2004**, *43* (26), 8272–8281.

(55) Chang, C. J.; Baker, E. A.; Pistorio, B. J.; Deng, Y.; Loh, Z.-H.; Miller, S. E.; Carpenter, S. D.; Nocera, D. G. Structural, Spectroscopic, and Reactivity Comparison of Xanthene- and Dibenzofuran-Bridged Cofacial Bisporphyrins. *Inorg. Chem.* **2002**, *41* (12), 3102–3109.

(56) Guchhait, T.; Sasmal, S.; Khan, F. S. T.; Rath, S. P. Oxo- and Hydroxo-Bridged Diiron(III) Porphyrin Dimers: Inorganic and Bio-Inorganic Perspectives and Effects of Intermacrocyclic Interactions. *Coord. Chem. Rev.* **2017**, *337*, 112–144.

(57) Vanover, E.; Huang, Y.; Xu, L.; Newcomb, M.; Zhang, R. Photocatalytic Aerobic Oxidation by a Bis-Porphyrin−Ruthenium(IV) μ-Oxo Dimer: Observation of a Putative Porphyrin−Ruthenium(V)−Oxo Intermediate. *Org. Lett.* **2010**, *12* (10), 2246–2249.

(58) Lindsey, J. S.; Wagner, R. W. Investigation of the Synthesis of Ortho-Substituted Tetraphenylporphyrins. *J. Org. Chem.* **1989**, *54* (4), 828–836.

(59) Yachandra, V. K.; Sauer, K.; Klein, M. P. Manganese Cluster in Photosynthesis: Where Plants Oxidize Water to Dioxygen. *Chem. Rev.* **1996**, *96* (7), 2927–2950.

(60) Gupta, R.; Taguchi, T.; Lassalle-Kaiser, B.; Bominaar, E. L.; Yano, J.; Hendrich, M. P.; Borovik, A. S. High-Spin Mn–Oxo Complexes and Their Relevance to the Oxygen-Evolving Complex within Photosystem II. *Proc Natl Acad Sci USA* **2015**, *112* (17), 5319–5324.

(61) Liu, W.; Groves, J. T. Manganese Catalyzed C–H Halogenation. *Acc. Chem. Res.* **2015**, *48* (6), 1727–1735.

(62) Groves, J. T.; Kruper, W. J.; Haushalter, R. C. Hydrocarbon Oxidations with Oxometalloporphinates. Isolation and Reactions of a (Porphinato)Manganese(V) Complex. *J. Am. Chem. Soc.* **1980**, *102* (20), 6375–6377.

(63) Hill, C. L.; Schardt, B. C. Alkane Activation and Functionalization under Mild Conditions by a Homogeneous Manganese(III)Porphyrin-Iodosylbenzene Oxidizing System. *J. Am. Chem. Soc.* **1980**, *102* (20), 6374–6375.

(64) Groves, J. T.; Lee, J.; Marla, S. S. Detection and Characterization of an Oxomanganese(V) Porphyrin Complex by Rapid-Mixing Stopped-Flow Spectrophotometry. *J. Am. Chem. Soc.* **1997**, *119* (27), 6269–6273.

(65) Nam, W.; Kim, I.; Lim, M. H.; Choi, H. J.; Lee, J. S.; Jang, H. G. Isolation of an Oxomanganese(V) Porphyrin Intermediate in the Reaction of a Manganese(III) Porphyrin Complex and H2O2 in Aqueous Solution. *Chem. Eur. J.* **2002**, *8* (9), 2067–2071.

(66) Song, W. J.; Seo, M. S.; DeBeer George, S.; Ohta, T.; Song, R.; Kang, M.-J.; Tosha, T.; Kitagawa, T.; Solomon, E. I.; Nam, W. Synthesis, Characterization, and Reactivities of Manganese(V)−Oxo Porphyrin Complexes. *J. Am. Chem. Soc.* **2007**, *129* (5), 1268–1277.

(67) Jin, N.; Ibrahim, M.; Spiro, T. G.; Groves, J. T. Trans-Dioxo Manganese(V) Porphyrins. *J. Am. Chem. Soc.* **2007**, *129* (41), 12416–12417.

(68) Groves, J. T.; Stern, M. K. Synthesis, Characterization, and Reactivity of Oxomanganese(IV) Porphyrin Complexes. *J. Am. Chem. Soc.* **1988**, *110* (26), 8628–8638.

(69) Schappacher, M.; Weiss, R. Formation of Manganese(IV)-Oxo-Porphyrin Derivatives by Decomposition of Peroxycarbonate Complexes. *Inorg. Chem.* **1987**, *26* (8), 1189–1190.

(70) Charnock, J. M.; Garner, C. D.; Trautwein, A. X.; Bill, E.; Winkler, H.; Ayougou, K.; Mandon, D.; Weiss, R. Characterization of an Oxo(Porphyrinato)Manganese(IV) Complex by X-Ray Absorption Spectroscopy. *Angew. Chem. Int. Ed. Engl.* **1995**, *34* (3), 343–346.

(71) Fukuzumi, S.; Fujioka, N.; Kotani, H.; Ohkubo, K.; Lee, Y.-M.; Nam, W. Mechanistic Insights into Hydride-Transfer and Electron-Transfer Reactions by a

Manganese(IV)−Oxo Porphyrin Complex. *J. Am. Chem. Soc.* **2009**, *131* (47), 17127–17134.

(72) Guo, M.; Seo, M. S.; Lee, Y.-M.; Fukuzumi, S.; Nam, W. Highly Reactive Manganese(IV)-Oxo Porphyrins Showing Temperature-Dependent Reversed Electronic Effect in C–H Bond Activation Reactions. *J. Am. Chem. Soc.* **2019**, *141* (31), 12187–12191.

(73) Arasasingham, R. D.; He, G. X.; Bruice, T. C. Mechanism of Manganese Porphyrin-Catalyzed Oxidation of Alkenes. Role of Manganese(IV)-Oxo Species. *J. Am. Chem. Soc.* **1993**, *115* (18), 7985–7991.

(74) Klaine, S.; Bratcher, F.; Winchester, C. M.; Zhang, R. Formation and Kinetic Studies of Manganese(IV)-Oxo Porphyrins: Oxygen Atom Transfer Mechanism of Sulfide Oxidations. *J. Inorg. Biochem.* **2020**, *204*, 110986.

(75) Hoshino, M.; Nagashima, Y.; Seki, H.; De Leo, M.; Ford, P. C. Laser Flash Photolysis Studies of Nitritomanganese(III) Tetraphenylporphyrin. Reactions of O $_2$, NO, and Pyridine with Manganese(II) Tetraphenylporphyrin. *Inorg. Chem.* **1998**, *37* (10), 2464–2469.

(76) Kwong, K. W.; Winchester, C. M.; Zhang, R. Photochemical Generation of Manganese(IV)-Oxo Porphyrins by Visible Light Photolysis of Dimanganese(III) μ-Oxo Bis-Porphyrins. *Inorganica Chim. Acta* **2016**, *451*, 202–206.

(77) Kwong, K. W.; Chen, T.-H.; Luo, W.; Jeddi, H.; Zhang, R. A Biomimetic Oxidation Catalyzed by Manganese(III) Porphyrins and Iodobenzene Diacetate: Synthetic and Mechanistic Investigations. *Inorganica Chim. Acta* **2015**, *430*, 176–183.

(78) Shaw, S.; White, J. D. Asymmetric Catalysis Using Chiral Salen–Metal Complexes: Recent Advances. *Chem. Rev.* **2019**, *119* (16), 9381–9426.

(79) McGarrigle, E. M.; Gilheany, D. G. Chromium− and Manganese−salen Promoted Epoxidation of Alkenes. *Chem. Rev.* **2005**, *105* (5), 1563–1602.

(80) Venkataramanan, N. S.; Kuppuraj, G.; Rajagopal, S. Metal–Salen Complexes as Efficient Catalysts for the Oxygenation of Heteroatom Containing Organic Compounds—Synthetic and Mechanistic Aspects. *Coord. Chem. Rev.* 2005, *249* (11–12), 1249–1268.

(81) Samsel, E. G.; Srinivasan, K.; Kochi, J. K. Mechanism of the Chromium-Catalyzed Epoxidation of Olefins. Role of Oxochromium(V) Cations. *J. Am. Chem. Soc.* **1985**, *107* (25), 7606–7617.

(82) Zhang, R.; Newcomb, M. Laser Flash Photolysis Generation of High-Valent Transition Metal−Oxo Species: Insights from Kinetic Studies in Real Time. *Acc. Chem. Res.* **2008**, *41* (3), 468–477.

(83) Klaine, S.; Fung Lee, N.; Dames, A.; Zhang, R. Visible Light Generation of Chromium(V)-Oxo Salen Complexes and Mechanistic Insights into Catalytic Sulfide Oxidation. *Inorg. Chim. Acta* **2020**, *509*, 119681.

(84) Otocka, S.; Kwiatkowska, M.; Madalińska, L.; Kiełbasiński, P. Chiral Organosulfur Ligands/Catalysts with a Stereogenic Sulfur Atom: Applications in Asymmetric Synthesis. *Chem. Rev.* **2017**, *117* (5), 4147–4181.

(85) Lee, N. F.; Patel, D.; Liu, H.; Zhang, R. Insights from Kinetic Studies of Photo-Generated Compound II Models: Reactivity toward Aryl Sulfides. *J. Inorg. Biochem.* **2018**, *183*, 58–65.

(86) Abebrese, C.; Huang, Y.; Pan, A.; Yuan, Z.; Zhang, R. Kinetic Studies of Oxygen Atom Transfer Reactions from Trans-Dioxoruthenium(VI) Porphyrins to Sulfides. *J. Inorg. Biochem.* **2011**, *105* (12), 1555–1561.

(87) Mahammed, A.; Gray, H. B.; Meier-Callahan, A. E.; Gross, Z. Aerobic Oxidations Catalyzed by Chromium Corroles. *J. Am. Chem. Soc.* **2003**, *125* (5), 1162–1163.

(88) Irie, R.; Noda, K.; Ito, Y.; Katsuki, T. Enantioselective Epoxidation of Unfunctionalized Olefins Using Chiral (Salen)Manganese(III) Complexes. *Tetrahedron Lett.* **1991**, *32* (8), 1055–1058.

(89) Palucki, M.; Hanson, P.; Jacobsen, E. N. Asymmetric Oxidation of Sulfides with H2O2 Catalyzed by (Salen)Mn(III) Complexes. *Tetrahedron Lett.* **1992**, *33* (47), 7111–7114.

(90) Bryliakov, K. P.; Babushkin, D. E.; Talsi, E. P. 1H NMR and EPR Spectroscopic Monitoring of the Reactive Intermediates of (Salen)MnIII Catalyzed Olefin Epoxidation. *J. Mol. Catal. A Chem.* **2000**, *158* (1), 19–35.

(91) Malone, J.; Klaine, S.; Alcantar, C.; Bratcher, F.; Zhang, R. Synthesis of a Light-Harvesting Ruthenium Porphyrin Complex Substituted with BODIPY Units. Implications for Visible Light-Promoted Catalytic Oxidations. *New J. Chem.* **2021**, *45* (11), 4977–4985.

CURRICULUM VITAE

EDUCATION

Master of Science, Chemistry   May 2021

Western Kentucky University, Bowling Green, Kentucky

Summa Cum Laude (GPA 4.00)

Bachelor of Science, Chemistry   May 2019

Bachelor of Science, Biology | Minor, Biophysics

Western Kentucky University, Bowling Green, Kentucky

Summa Cum Laude (GPA 3.94)

PEER-REVIEWED PUBLICATIONS

- Malone J.; **Klaine S.**; Alcantar C.; Bratcher F., Zhang R. Synthesis of a Novel Ruthenium Porphyrin Complex Substituted with Lightharvesting BODIPY Units. Implications for Visible Light-promoted Catalytic Oxidations. *New J. Chem.* **2020**, *45***,** 4977-4985**.**
- Zhang, R.; **Klaine, S.**; Alcantar, C.; Bratcher, F.; Visible Light Generation of High-Valent Metal-Oxo Intermediates and Mechanistic Insights into Catalytic Oxidations. *J. Inorg. Biochem.* **2020**, *212*, 111246.
- **Klaine, S**.; Fung Lee, N.; Dames, A.; Zhang, R. Visible Light Generation of Chromium(V)-Oxo Salen Complexes and Mechanistic Insights into Catalytic Sulfide Oxidation. *Inorg. Chim. Acta* **2020**, *509*, 119681.
- **Klaine, S**.; Bratcher, F.; Winchester, C. M.; Zhang, R. Formation and Kinetic Studies of Manganese(IV)-Oxo Porphyrins: Oxygen Atom Transfer Mechanism of Sulfide Oxidations. *J. Inorg. Biochem.* **2020**, *204*, 110986.

PRESENTATIONS

- **Klaine, S.**; Zhang R. *Oxidation kinetic studies and photochemical production of high-valent manganese(IV)-oxo porphyrins, chromium(V)-oxo salens, and manganese(V)-oxo salens*, The 260th American Chemical Society Meeting, virtual, April 5-16, 2021.
- **Klaine S.**; Zhang R. *Oxidation kinetic studies and photochemical production of high-valent manganese(IV)-oxo porphyrins and chromium (V)-oxo salens.* The 106th Kentucky Academy of Science Annual Meeting, Berea, KY, November 6-7, 2020
- **Klaine S.** *Photochemical generation and kinetic studies of manganese(IV)-oxo porphyrins and chromium(V)-oxo salens.* WKU Department of Chemistry Research Seminar, Bowling Green KY, October 10th, 2020.
- **Klaine S.**; Dames A.; Bratcher F.; Zhang R. *Photochemical generation and oxidation kinetic studies of chromium(V)-oxosalen intermediates*. The 50th Annual WKU Student Research Conference, Bowling Green, KY, May 2nd, 2020.

- **Klaine S.** *Photopromoted Ru-Catalyzed Asymmetric Aerobic Sulfide Oxidation and Epoxidation Using Water as a Proton Transfer Mediator.* WKU Department of Chemistry Literature Seminar, Bowling Green KY, April 10th, 2020.
- **Klaine S.**; Zhang R. *Visible light generation and kinetic studies of a chromium(V)-oxosalen complex*, The 105th Kentucky Academy of Science Annual Meeting, Berea, KY, November 1-2, 2019
- **Klaine, S.**; Ning W.; Zhang R. *Oxidation kinetic studies on porphyrin-manganese(IV)-oxo intermediates via chemical and photochemical generation*, The 71st Southeastern Regional Meeting of the American Chemical Society, Savannah, GA, October 20-23, 2019.
- **Klaine, S.**; Winchester C.; Zhang R. *Oxidation kinetics of porphyrin-manganese(IV)-oxo intermediates generated by chemical and photochemical methods*, The 257th American Chemical Society Meeting, Orlando, FL, March 31-4, 2019.
- **Klaine, S**.; Winchester C.; Zhang R. *Generation and kinetic studies of porphyrin-manganese(IV)-oxo intermediates*, The 104th Kentucky Academy of Science Annual Meeting, Bowling Green, KY, November 2-3, 2018.
- **Klaine, S.**; Winchester C.; Zhang R. *Oxidation kinetics of porphyrin-manganese(IV)-oxo intermediates generated by chemical and photochemical methods*, The 49th Annual WKU Student Research Conference, Bowling Green, KY, March 23, 2019.

HONORS, AWARDS, AND INTERNAL GRANTS

AIC Outstanding Graduate Student Award	2021
Carl P. McNally Graduate Fellowship	2020
Klaine, S. and Zhang, R. The Graduate School - Research Grant, $3,000	2019
Klaine, S. and Zhang, R. Fuse Grant, $4,000	2019
Graduate Research Assistantship	2019
American Chemical Society Organic Division Undergraduate Award	2019
Department of Chemistry Scholarship	2018
Turiano and Concepcion Memorial Scholarship	2018
September Birthday Club Scholarship	2018
William H Horrell Scholarship	2017
Dr. Sharron Halcomb Francis Scholarship	2017
BB&T Bank Scholarship	2016
E.A. Diddle Scholarship	2015

PROFESSIONAL EXPERIENCE

Graduate Research Assistant   June 2018 -Present

Advisor: Rui Zhang Ph.D., *Professor*

- Investigated high-valent transition metal oxo species through spectroscopic detections and kinetic studies of various oxidation reactions
- Served as the laboratory leader and manager

Undergraduate Teaching Assistant   May 2018 - December 2018

Advisor: Lawrence Hill, Ph.D., *Assistant Professor* and Rui Zhang Ph.D., *Professor*

- Instructed students with experimentation, graded assignments, and presented lectures
- Principles of Organic Chemistry Lab (CHEM 108)
- Organic Chemistry I Lab (CHEM 341)
- Organic Chemistry II Lab (CHEM 343)

Undergraduate Research Assistant   September 2016 - May 2018

Advisor: Donald Slocum, Ph.D.*, Emeritus Research Professor*

- Studied regioselective electrophilic aromatic substitutions and halogen-lithium metal exchange reaction

ABBREVIATIONS AND SYMBOLS

2,6-Cl$_2$PyNO	2,6-dichloropyridine *N*-oxide
AgCl	Silver chloride
AgBrO$_3$	Silver Bromate
AgClO$_3$	Silver chlorate
Ar	Aryl
Al$_2$O$_3$	Aluminum oxide
AU	Absorbance unit
BF$_3$·OEt$_2$	Boron trifluoride diethyl etherate
P450	Cytochrome P450s
CDCl$_3$	Chloroform-*d*
CHCl$_3$	Chloroform
CH$_2$Cl$_2$	methylene chloride
CH$_3$CN	Acetonitrile
CO	Carbon monoxide
[Cr^{III}(napthen)Cl]	(*R,R*)-(−)-*N,N′*-Bis(2-hydroxy-1-naphthalidene)-1,2-cyclohexanediaminochromium(III) chloride
[Cr^{III}(salen)Cl]	(*R,R*)-(−)-*N,N′*-Bis(3,5-di-tert-butylsalicylidene)-1,2-cyclohexanediaminochromium(III) chloride
Cys	Cysteine
DMF	*N,N*-Dimethylformamide
DDQ	2,3-Dichloro-5,6-dicyano-p-benzoquinone
EPR	Electron Paramagnetic Resonance

ESI	Electron Spray Ionization
Equiv.	Equivalents
EXAFS	Extended X-ray absorption fine structure
FID	Flame Ionization Detector
[Fe^{III}(TDCPP)Cl]	5,10,15,20-tetrakis(2,6-dichlorophenyl)porphyrinatoiron(III) chloride
[Fe^{III}(TMP)Cl]	5,10,15,20-tetramesitylporphyrinatoiron(III) chloride
GC	Gas Chromatography
h	hour
HAT	Hydrogen atom transfer
HCl	Hydrochloric acid
Hx	Hexane
[H$_2$(napthen)]	(*R,R*)-(−)-*N,N′*-Bis(2-hydroxy-1-naphthalidene)-1,2-cyclohexanediamine
[H$_2$(Por)]	porphyrin
[H$_2$(salen)]	(*R,R*)-(−)-*N,N′*-Bis(3,5-di-tert-butylsalicylidene)-1,2-cyclohexanediamine
[H$_2$(TMP)]	5,10,15,20-tetramesitylporphyrin
[H$_2$(TDFPP)]	5,10,15,20-tetrakis(2,6-dichlorophenyl)porphyrin
[H$_2$(TPFPP)]	5,10,15,20-tetrakis(pentafluorophenyl)porphyrin
H$_2$O	Water
H$_2$O$_2$	Hydrogen peroxide
Imid	Imidazole

k_{rel}	Relative rate constant
k_{obs}	Observed pseudo-first-order rate constants
k_0	Background rate constant
$KHSO_5$	Potassium peroxymonosulfate
KIE	Kinetic Isotope effect
LFP	Laser flash photolysis
[Mn^{III}(napthen)Cl]	(R,R)-(−)-*N*,*N*′-Bis(2-hydroxy-1-naphthalidene)-1,2-cyclohexanediaminomanganese(III) chloride
[Mn^{III}(salen)Cl]	(R,R)-(−)-*N*,*N*′-Bis(3,5-di-tert-butylsalicylidene)-1,2-cyclohexanediaminomanganese(III) chloride
[Mn^{III}(TMP)Cl]	5,10,15,20-tetramesitylporphyrinatomanganese(III) chloride
[Mn^{III}(TDFPP)Cl]	5,10,15,20-tetrakis(2,6-dichlorophenyl)porphyrinato manganese(III)
[Mn^{III}(TPFPP)Cl]	5,10,15,20-tetrakis(2,3,4,5,6,-pentafluorophenyl)porphyrinatomanganese(III) chloride
MeOH	Methanol
min	minute
MS	Mass Spectroscopy
m/*z*	Mass-to-charge ratio
mCPBA	*meta*-chloroperoxybenzoic acid
NADPH	Nicotinamide adenine dinucleotide phosphate
NBS	*N*-bromosuccinimide
NCS	*N*-chlorosuccinimide

NH$_4$Cl	Ammonium Chloride
NMR	Nuclear Magnetic Resonance
NaClO$_2$	Sodium chlorite
NaOCl	Sodium hypochlorite
NaIO$_4$	Sodium periodate
PhIO	Iodosylbenzene
PTFE	Polytetrafluoroethylene
OAT	Oxygen Atom Transfer
O$_2$	Dioxygen
O$_3$	Ozone
PhI(OAc)$_2$	Iodobenzene diacetate
PPh$_3$	Triphenylphosphine
Py	Pyridine
RDS	Rate-determining step
Rho (ρ)	Reaction constant
s	second
Sub	Substrate
^{t}BuOOH	*tert*-butyl hydroperoxide
THF	Tetrahydrofuran
TLC	Thin layer chromatography
TMS	Tetramethylsilane
UV-Vis	Ultraviolet-Visible
XANES	X-ray absorption near edge structure

NUMBER INDEX

1	[H$_2$(Por)] or [H$_2$(Salen)]	**5c**	[Mn^{III}(TPFPP)(XO$_3$)]
1a	[H$_2$(TPFPP)]	**6**	[Mn^{IV}(TPFPP)(O)]
1b	[H$_2$(TDFPP)]	**6a**	[Mn^{IV}(TPFPP)(O)]
1c	[H$_2$(TMP)]	**6b**	[Mn^{IV}(TDFPP)(O)]
1d	[H$_2$(salen)]	**6c**	[Mn^{IV}(TPFPP)(O)]
1e	[H$_2$(napthen)]	**7**	[Mn^{II}(Por)Cl]
2	[Mn^{III}(Por)Cl]	**7c**	[Mn^{II}(TPFPP)Cl]
2a	[Mn^{III}(TPFPP)Cl]	**8**	[Mn^{V}(Por)Cl]
2b	[Mn^{III} (TDFPP)Cl]	**9d**	[Cr^{III}(salen)XO$_3$]
2c	[Mn^{III}(TMP)Cl]	**9e**	[Cr^{III}(napthen)XO$_3$]
3d	[Cr^{III}(salen)Cl]	**10d**	[Cr^{V}(salen)O]$^+$
3e	[Cr^{III}(napthen)Cl]	**10e**	[Cr^{V}(napthen)O]$^+$
4d	[Mn^{III}(salen)Cl]	**11d**	[Mn^{III}(salen)XO$_3$]
4e	[Mn^{III}(napthen)Cl]	**11e**	[Mn^{III}(napthen)XO$_3$]
5a	[Mn^{III}(TPFPP)(XO$_3$)]	**12d**	[Mn^{V}(salen)O]$^+$
5b	[Mn^{III}(TDFPP)(XO$_3$)]	**12e**	[Mn^{V}(napthen)O]$^+$